工學博士學位論文

Fabrication of Polypyrrole Nanowire-based Conductive Nanostructures by Electrodeposition and Their Chemical/Biosensor Applications

전기도금법을 통한 폴리피롤 나노와이어 기반

전도성 나노구조체 제조 및 화학/바이오센서 응용

2019年 8月

서울大學校 大學院

化學生物工學部

趙 敬 熙

Fabrication of Polypyrrole Nanowire-based Conductive Nanostructures by Electrodeposition and Their Chemical/Biosensor Applications

by

Kyung Hee Cho

Submitted to the Graduate School of Seoul National University in Partial Fulfillment of the Requirements for the Degree of Doctor of Philosophy

August, 2019

Thesis Adviser: Jyongsik Jang

Abstract

Demands for high-performance sensors are exploding today as chemical sensors and biosensors are used in a variety of areas, including industrial safety, environmental management, medical diagnosis, food quality tests, and health status tracking. Indicators that evaluate a sensor performance can largely address sensitivity, selectivity, response/recovery speed, and reliability. The transducer material is one of the sensor components that have a fundamental effect on the performance improvement of the sensor, as it reacts directly or indirectly with the target material and converts it into a measurable electrical signal. In particular, many studies have been conducted on conductive polymer nanomaterials as transducers because of several advantages. Compared to inorganic or metal oxide-based nanomaterials, they are easily synthesized in versatile structures, light, flexible, and their surface functionalities are facilely tunable. Among the various conductive polymers, polypyrrole has been appealing research theme as the monomer is easily oxidized and well dissolved in water and that polymerized products have strong environmental stability, good redox properties, high electrical conductivity and biocompatibility. Sensor transducers based on

polypyrrole nanomaterials can help improve sensor performance by regulating physical structures and chemical composition through combining diverse polymerization and modification methods.

This dissertation describes the effective synthetic and application methods of polypyrrole nanowire-based transducer. Firstly, three-dimensional microvillus-like polypyrrole nanowire-based conductive nanofilms (3D MCN) with different morphologies and doping levels were synthesized by electropolymerization and electrochemical doping control methods. The resulting doping level-controlled 3D MCN-based VOC sensor displayed high sensitivity toward ammonia and methanol gases ascribed to the enhanced carrier mobility. Secondly, Pd nanoparticle-decorated three-dimensional polypyrrole nanowire-based conductive nanofilms (PPyPd) with different population and size of Pd nanoparticles were fabricated by sequential electrodeposition steps. The resulting PPyPd was applied to highly sensitive gas sensor for hydrogen gas detection. Finally, multidimensional polypyrrole nanowire-based conductive nanofilms (MCNF) with different *L/D* ratios of polypyrrole nanowires and degree of surface carboxylation were fabricated using electropolymerization process and acid treatment. After

immobilization of binding aptamers, MCNF-based FET-type biosensor showed superb performance in detection of HBsAg. Accordingly, this study provides promising synthetic and application approaches of polypyrrole nanowires as transducer materials to achieve highly sensitive, selective, stable, and flexible chemical/biosensors. Furthermore, the material manufacturing and modifying methodologies discussed in this dissertation is expected to be extended to various organic/inorganic nanomaterials other than polypyrrole nanowires.

Keywords: Sensor, Polypyrrole nanowire, Electrodeposition, Doping, Noble metal, Aptamer.

Student Number: 2014-22602

List of Abbreviations

3D MCN: three-dimensional microvillus-like conductive nanofilm

3D: three-dimensional

A: ampere

A_MCNF: aptamer-functionalized multidimensional conductive

nanofilm

AFM: Atomic force microscopy

AA: ascorbic acid

Ag: silver

Ag/AgCl: silver chloride electrode

Au: gold

BSA: bovine serum albumin

ca.: circa

cm: centi-meter

CP: conducting polymer

CPPyNW: carboxylated polypyrrole nanowire

Cr: chrome

Cu: copper

CVD: chemical vapor deposition

D: drain

d: thickness

DI: deionized

Dibasic: Sodium phosphate dibasic dodecahydrate

DMTMM: 4-(4,6-dimethoxy-1,3,5-triazin-2-yl)-4-methyl-morpholinium chloride

e.g.: exempli gratia

EDS: energy-dispersive X-ray spectra

eV: electron volt

fcc: face-centered-cubic

FE-SEM: field-emission scanning electron microscopy

FET: field-effect transistor

FT-IR: Fourier transform-infrared

Gr: graphene

h: hour

H_2: hydrogen

H_2SO_4: sulfuric acid

HBsAg: hepatitis B surface antigen

HBV: hepatitis B virus

HNO_3: nitric acid

HOMO: highest occupied molecular orbital

HR-TEM: high resolution-transmission electron microscopy

$I–V$: current–voltage

i.e.: id est

I_0: measured initial current

IDA: interdigitated array

IgG: immunoglobulin G

I_{SD}: source-drain current

I_{SD}-V_{SD}: source-drain current versus source drain voltage

JCPDS: joint committee on powder diffraction standards

L/D: length to diameter

LiBis: Bis(trifluoromethane)sulfonimide lithium salt

LUMO: lowest unoccupied molecular orbital

MCNF: multidimensional conductive nanofilm

MDL: minimum detectable level

MeOH: methanol

MFC: mass flow controller

min: minute

mL: milliliter

mM: milli-mole

Monobasic: sodium phosphate monobasic dihydrate

n-type: negative-type

N_2: nitrogen

Ni: nickel

nm: nanometer

NP: nanoparticle

p-type: positive-type

PANI: polyaniline

PBS: phosphate buffered-saline

PEDOT: poly(3,4-ethylenedioxythiophene)

Pd: palladium

$PdCl_2$: palladium chloride

PdHx: palladium halide

PdO: palladium oxide

PEDOT:PSS: poly(3,4-ethylenedioxythiophene):poly(styrene-

sulfonate)

PEN: poly(ethylene naphthalate)

PET: poly(ethylene terephthalate)

PMMA: poly(methyl methacrylate)

ppb: parts per billion

ppm: parts per million

PPyPd: palladium nanoparticle-decorated three dimensional polypyrrole nanostructure

PPyPd_0.1: PPyPd prepared with 0.1 mM $PdCl_2$ precursor solution

PPyPd_1.0: PPyPd prepared with 1.0 mM $PdCl_2$ precursor solution

PPyPd_10: PPyPd prepared with 10 mM $PdCl_2$ precursor solution

PPyPd_0.1_5: PPyPd_0.1 prepared at reaction temperature of 5°C

PPyPd_0.1_60: PPyPd_0.1 prepared at reaction temperature of 60°C

PPyPd_0.1_90: PPyPd_0.1 prepared at reaction temperature of 90°C

PPy: polypyrrole

PPy@IDA: polypyrrole nanostructure electropolymerized at interdigitated array

PPyNW: polypyrrole nanowire

Pt: platinum

pTSA: *para*-toluenesulfonic acid

Py: pyrrole

ΔR: resistance change

R: real-time measured resistance

R_0: initial measured resistance

rGO: reduced graphene oxide

S/N: signal-to-noise

s: second

S: source

sccm: standard cubic centimeters per minute

Si: silicon

slm: standard liters per minute

ssDNA: single-stranded DNA

UA: uric acid

UV-Vis: ultraviolet-visible

V_G: gate voltage

VOC: volatile organic compound

V_{SD}: source-drain voltage

XPS: X-ray photoelectron spectroscopy

XRD: X-ray diffraction

ε: relative dielectric constant

θ: theta

μ: charge mobility

μL: microliter

μm: micrometer

σ: conductivity

List of Figures

and (b) liquid-ion gated FET biosensor system.

PPy surface is hindered. Small Pd clusters deposited on Pd NP surface aggregate and coalesce to cover the entire surface.

treatment).

and target (HBsAg) analytes.

List of Tables

Table of Contents

1. Introduction

1.1. Background

1.1.1. Conducting polymers

Conducting polymers are polymers that conduct electricity due to their unique π-conjugated chain structures. They have attracted considerable attention since Heeger *et al.* reported polyacetylene in 1977 [1-3]. For the last few decades, the typical conducting polymers such as polypyrrole (PPy), polyaniline (PANI), polythiophene (PT), and poly(3,4-ethylenedioxythiophene) (PEDOT) have been extensively researched (**Figure 1**).

Generally, conducting polymers consist of the π-conjugated backbones of the alternating single (σ) and double (π) bonds. This conjugated backbone is the conduction pathway where charge carriers move through to generate conduction. The conjugation state of the conducting polymer such as conjugation length, intra-/inter-chain interactions, the extent of disorder governs the electrical and optical properties of conducting polymers [4].
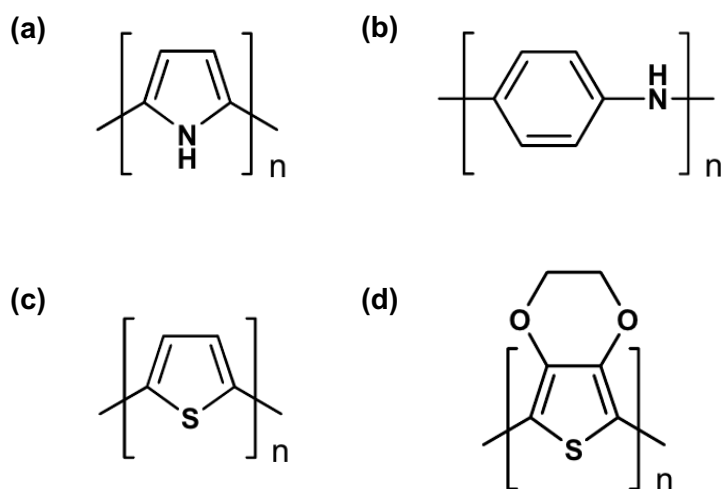
Figure 1. Chemical structures of some of the most extensively researched conducting polymers represented with repeating units (undoped states). (a) Polypyrrole, (b) Polyaniline, (c) Polythiophene, and (d) Poly(3,4-ethylenedioxythiophene).

1.1.1.1. Conducting polymer nanomaterials

Nanotechnology deals with the fabrication and various applications of functional materials and structures in the range of 1 nm to 100 nm using chemical and physical methods [5]. The properties of the nanomaterials (optical, electrical, mechanical, and chemical) are usually different from those of their counterpart, bulk materials. This phenomenon originates from the surface effects and quantum effects [6,7]. Nanomaterials have high particle number per unit mass or volume (i.e., high surface-to-volume ratio), which induces high reactivity and low melting point (**Figure 2**). In addition, nanomaterials can be regarded as "pseudo-atoms" because they have quantized states of energy.

Among various nanomaterials, fabrication of conducting polymer nanomaterials has been a fascinating topic because of the favorable advantages over other metal and inorganic nanomaterials: facile synthesis, a wide range of source materials, structural versatility, tunable surface functionalities, lightweight, and flexibility (**Figure 3**) [8-10]. For example, conducting polymer (CP) nanomaterials are considered a great signal transducer for chemical/biosensors due to its inherent electrical and biocompatible properties [11]. Also, it is

attractive that CP nanomaterials are easily fabricated into various morphologies such as nanoparticles, core-shell nanomaterials, nanowires, nanotubes, nanofibers, and arbitrary nano-patterns by electrochemical and chemical polymerization methods [12-17]. Facile modulation of the nanostructure enables us to explore shape and size-dependent properties of CP. Another important benefit is that the chemical composition of CP nanomaterials is readily modified by synthetic variables or post-treatment after polymerization. Under their advantages, CP nanomaterials have opened the doors to advanced applications in the fields of displays, sensors, actuators, solar cells, catalysis, energy storage, and biological systems [18]. So far, investigations have been confined to enlarging the surface area of CP nanomaterials rather than manipulating surface functionality. Thus, developing CP nanomaterials with not only enhanced surface-to-volume ratio but also improved surface functionality is needed. Furthermore, manipulating CP nanomaterial shapes are also a challenging topic in various applications as they are directly related to the electron pathway.

(a)
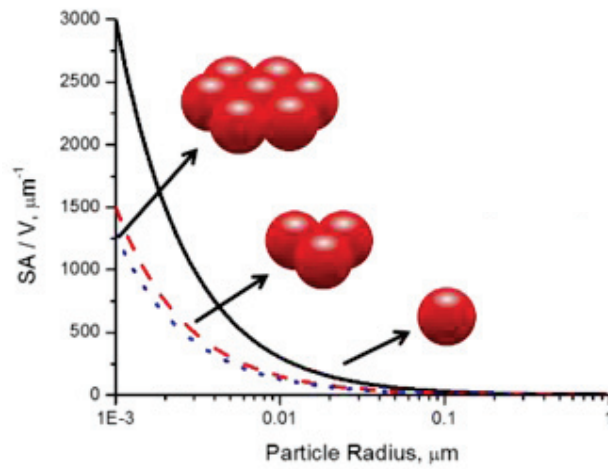
(b)

Nanoparticles in different shapes	Bar-like nanoparticle	Spherical	Planar
Images			
Dimension	1nm×5.33nm	2nm	4nm×0.33nm
Surface area to volume ratio(S/V)	4.375	3	7.061

Figure 2. Size effects of metal nanomaterials. (a) The surface-to-volume ratio of a particle increases with decreasing particle size. (b) Nanoparticles of different shapes with equal volumes [6,7].
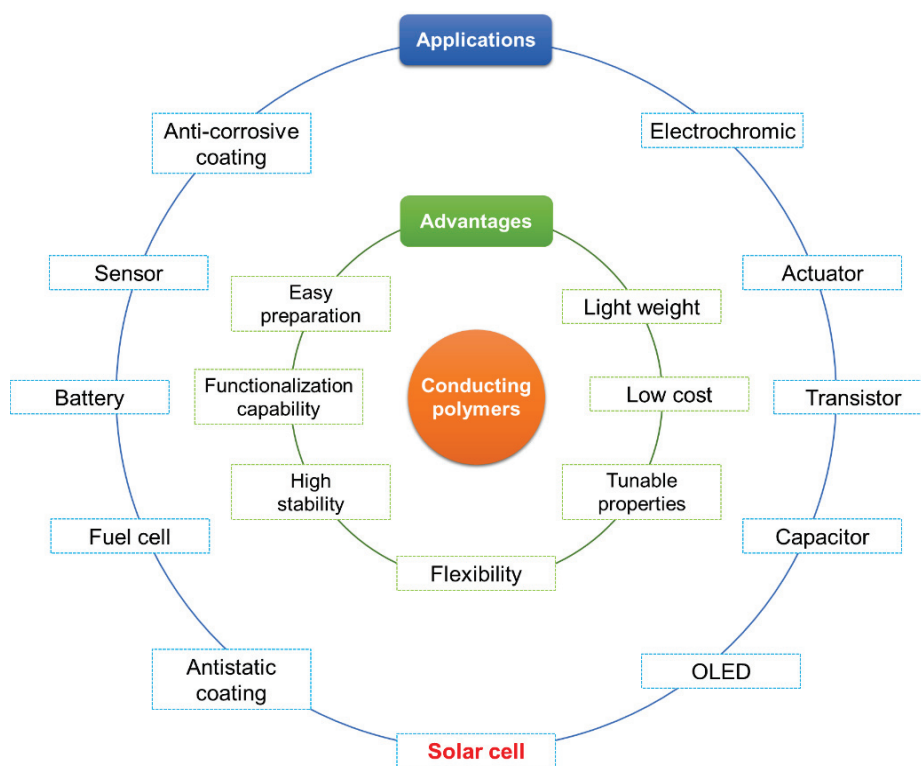
Figure 3. Schematic illustration of a wide range of application fields of conducting polymer nanomaterials.

1.1.1.2. Polypyrrole

Polypyrrole (PPy) consists of five-membered heterocyclic rings and it is by far one of the most intensively studied conducting polymer. The reasons for this intense focus on polypyrrole certainly lie in the fact that the monomer (pyrrole) is easily oxidized, water-soluble and commercially available. Hence, polypyrrole displays several beneficial characteristics including environmental stability, good redox properties and the ability to give high electrical conductivities [19,20]. As a result of its good intrinsic properties, polypyrrole has proven to have the potential for several applications including batteries, supercapacitors, electrochemical sensors, conductive textiles and fabrics, mechanical actuators, electromagnetic interference (EMI) shielding, anti-static coatings, and drug delivery systems [21,22].

The generic synthetic procedures for conducting polymers are i) chemical oxidative polymerization and ii) electrochemical polymerization. The former is suitable for mass production by obtaining powder-type materials, while the latter is suitable for precise control of the thin film. Chemical oxidative polymerization of the PPy involves addition polymerization. The most widely accepted mechanism of polymerization of polypyrrole is described in **Figure 4**

[23,24]. In the initial stage, pyrrole monomers are oxidized to generate radical cations ($C_4NH_5^{•+}$). Next, radical-radical coupling reactions occur between these cations to produce a dimer with deprotonation, forming a bipyrrole. The bipyrrole is reoxidized and couples with another radical cation. By repeating the previous steps, the PPy chain is propagated and finally terminated with a nucleophilic attack by water molecules or impurities [25].

The repeating units of PPy can be linked through α-α' and/or α-β couplings (**Figure 5**). The α-α' coupling leads to linear and planar structured PPy chains, thus producing high order of conjugation. On the contrary, α-β coupling reaction produces branched and cross-linked PPys and shortens the conjugation length. Meanwhile, other structural defects can also occur during polymerization, by insertion of hydroxyl and carbonyl groups as a result of overoxidation [5].

Electrochemical polymerization of polypyrrole is performed at an electrode applying the positive potential. The monomers used for electro-synthesizing CPs are aromatic compounds such as benzene, thiophene, pyrrole, aniline, furan, etc. This is mainly because these compounds can be oxidized to relatively stable cation radicals [26]. Most electropolymerized conducting polymers have crosslinked

structures since aromatic monomers possess more than two electroactive positions [26]. The radical cations of monomers are generated by electrochemical oxidation on the electrode surface, unlike the chemical oxidative polymerization. A more detailed description of electropolymerization is provided in the following section.
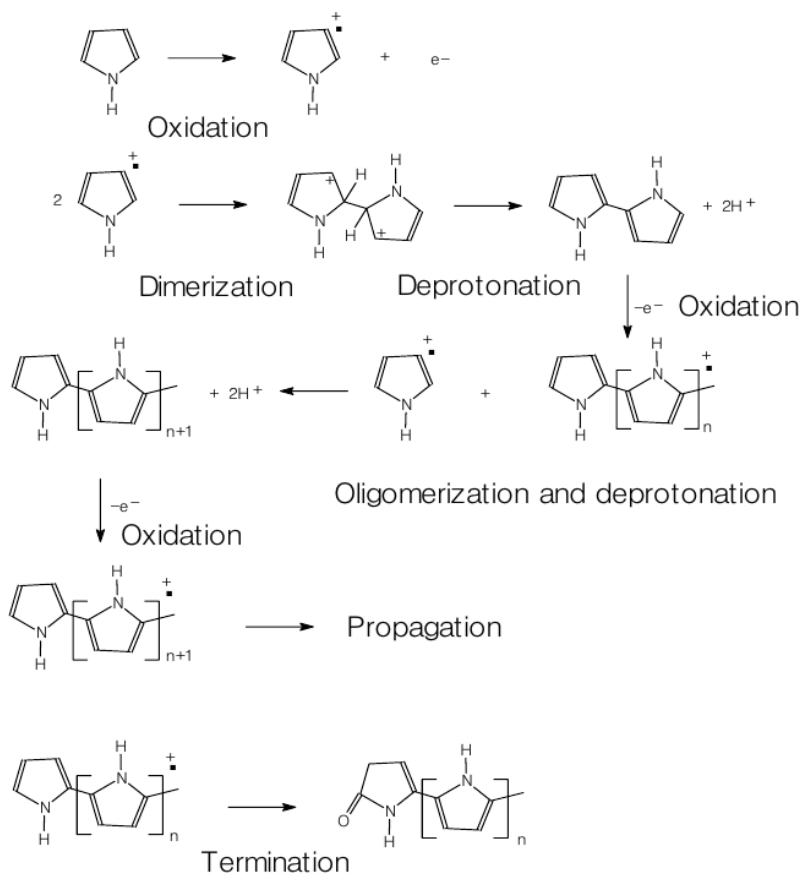
Figure 4. Widely accepted polymerization mechanism of pyrrole [23,24].
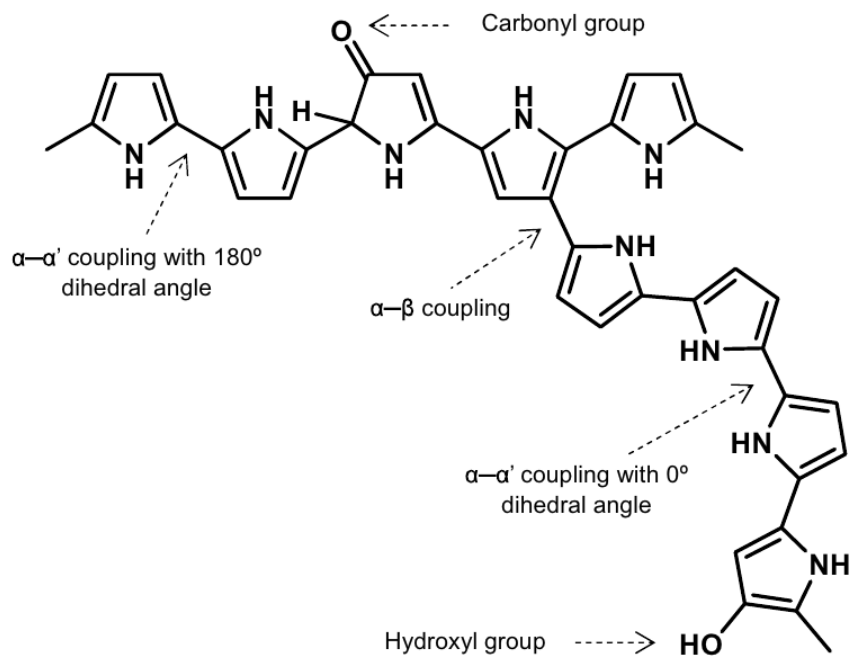
Figure 5. Possible chain structures in polypyrrole chains including conjugation and defects [5].

1.1.2. CVD graphene

First isolated by Novoselov and Geim at 2004, graphene is an allotrope of carbon where sp^2-bonded carbon atoms constitute a monolayer in a hexagonal honeycomb lattice [27]. Layers of graphene are easily attracted and stacked on top of each other by Van der Waals forces.

There are two major routes to synthesize graphene: the top-down approach and the bottom-up approach (**Figure 6**) [28]. The top-down approach involves splitting a large chunk of graphite into small pieces of graphenes by chemical, physical, and thermal treatments. Liquid phase exfoliation (i.e., Hummer's method), mechanical exfoliation (e.g., ball-milling), electrochemical exfoliation methods are such examples [29-31]. Although this approach allows facile mass production, it yields irregular sizes and qualities of the product.

Bottom-up approaches are opposite, which involves growing graphene on a substrate by assembling carbon atoms as building blocks (**Figure 7a**). Chemical vapor deposition (CVD) is a representative method of bottom-up approaches. CVD graphene is created in two steps: i) precursor pyrolysis to form carbon atoms ii) formation of graphene structure from coalescence of carbon atoms. Carbon source such as

methane gas flows inside the furnace and thermally decomposes on the catalytic surfaces (such as Ni and Cu foils) and graphene grows epitaxially at cooling stage [32-34]. Despite there are some hurdles in the CVD method such as difficulties of separation from the substrate or creating a complete uniform layer, the CVD method can produce relatively high-quality graphene on a large scale.

The high-quality graphene crystallite exhibits exceptional electronic properties. For example, it reveals the ambipolar electric field effect; if the gate voltage changes, the position of the Fermi energy changes. This means that either electrons or holes can be charge carriers of graphene. Graphene also shows superior carrier mobility which can exceed 15,000 $cm^2 V^{-1} s^{-1}$ under ambient conditions and significantly improved up to 1,000,000 $cm^2 V^{-1} s^{-1}$ [35]. Because of its extraordinary properties such as high current density, high thermal conductivity, and optical transmittance, graphene has gaining marked attention in research fields such as composite materials, supercapacitors, solar cells, transparent conducting electrodes, and biosensors.

An alternative exploit of the graphene is to consider as a conductive substrate because it is mechanically strong and very structure-stable down to nanometer sizes [35]. For instance, graphene can be prepared

as a conductive substrate to serve as the working electrode of the electrodeposition system. Conventionally, metal sheet or Au, Pt sputtered/deposited plates are used as the conductive substrate for electrochemical deposition of metal oxide and conducting polymers. To be utilized as a working electrode, the conductive substrate has to be inert during the electrochemical reaction without dissolution of the electrode. In this regard, CVD graphene is a great candidate for a working electrode as it has an inert, transparent feature and can be transferred to various substrates (**Figure 7b**) [36].
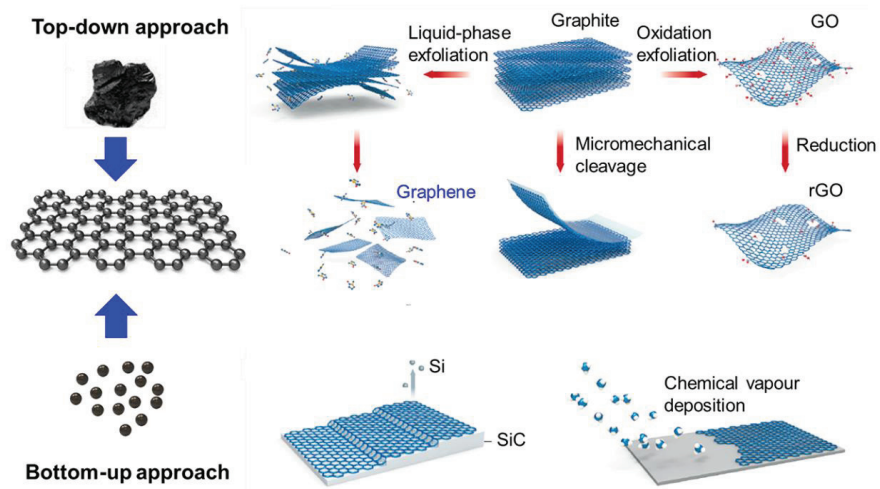
Figure 6. Classification of synthetic methods for the production of graphene: Top-down and bottom-up approaches [28].

(a)
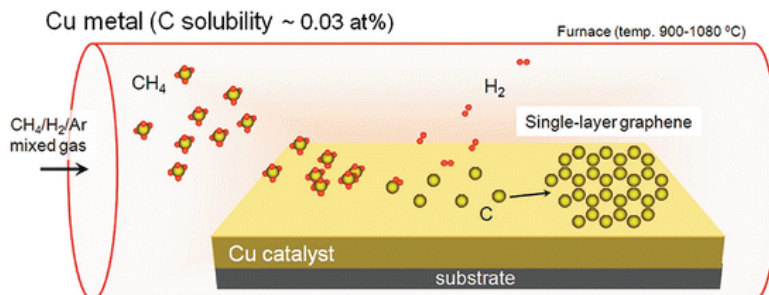
(b)
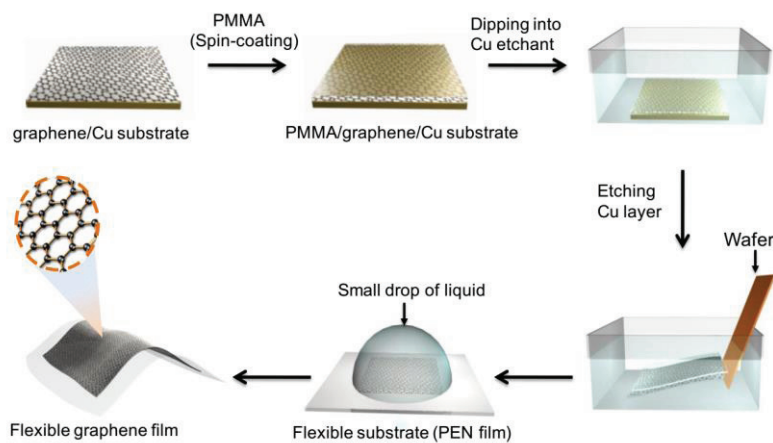
Figure 7. Synthetic procedures for CVD graphene. (a) CVD graphene growth in furnace. (b) Wet-transfer of the CVD graphene on the flexible substrate [33,34].

1.1.3. Synthesis and modification methods of nanomaterials

1.1.3.1. Electrochemical deposition

Electrochemical deposition (i.e., electrodeposition) is a technology to fabricate thin films or particles of metal and nonmetals (such as ceramics, electroactive polymers) by passing a current through an electrochemical cell from an external source. It stemmed from an ancient technique, electroless deposition, and has been used for a very long time. Traditional applications of electrodeposition include protective coatings, interconnects in integrated circuits, magnetic data storage systems [37]. In recent years, it has been emerged as an important technique and extensively applied in nanoelectronics, biotechnology, and energy engineering.

Electrochemical deposition is superior to other nanomaterial synthesis methods because of low energy consumption, the minimum requirement of the additives and absence of any interfering and byproducts generated during the process. It can be performed at room temperature from aqueous/organic-based electrolytes. Moreover, combined with 3D templates, complex shapes of nanomaterials of which scale range from a few atoms to large dimensions can be easily synthesized [38]. Hence, electrochemical deposition is a versatile

technique that can be used to synthesize desirable nanostructures for diverse applications.

Typical experimental setups for the electrochemical deposition include a counter electrode, working electrode (where desired nanomaterials are deposited onto), reference electrode, electrolyte, and external electric source (**Figure 8a**). Various electrochemical techniques can be used including potentiostatic (constant-potential), galvanostatic (constant-current) and potentiodynamic (potential scanning, i.e., cyclic voltammetry) methods [39].

Preparation of conducting polymer nanomaterials *via* electrochemical polymerization is generally preferred over chemical oxidation because it provides better control of film thickness and morphology, and cleaner polymers in a relatively short time (a few minutes). Moreover, the direct deposition of CP nanomaterials onto electrodes guarantees good Ohmic contact between the nanomaterial and the electrode, which is beneficial to sensing applications [40]. Films of electronically conducting polymers are generally deposited onto a working electrode surface by anodic oxidation (electropolymerization) of the corresponding monomer in the presence of an electrolyte solution [39,41]. Each CP monomers has its own oxidation potentials to form

reactive radical ion intermediates. For instance, pyrrole monomer oxidizes at potentials higher than *ca.* +0.75 V (vs. Ag/AgCl). At initial oxidation potential (0.8 V), radical cation of the monomer is produced and reacts with other monomers to form oligomers. These oligomers are easily oxidized at much lower oxidation potentials than monomers. During the polymerization, the anions are incorporated into the polymer chain to maintain electrical neutrality of the polymer. It is known that experimental factors such as monomers, dopants, solvent, pH, temperature, applied potential, and electrochemical method have a strong impact on the morphology of electropolymerized CP [42].

In the case of electrodeposition of metal or inorganic nanomaterials, there are two kinds of methods: i) electrophoretic deposition and ii) electrolytic deposition (**Figure 8b** and **c**) [43]. In the electrophoretic deposition, preformed metal nanoparticles that are covered by surface stabilizers are suspended in the solvent. The charged particles then move toward the electrode under an electric field. Whereas electrolytic deposition starts from solutions of ionized metal salts. The electrodeposition mechanism of the metal nanomaterials (i.e., electrolytic deposition) is quite different from that of CP nanomaterials. Most of the metallic deposition occurs at the cathode surface as the

adsorbed metal ions or complexes are reduced. The deposition mechanisms are based on the Derjaguin-Landau-Verwey-Overbeek (DLVO) theory of colloidal stability [44]. The particle formation kinetics and deposit composition are influenced by deposition potentials, solvent, additives, temperature and current density [45]. Recently, various micro/nanostructures of metals (Ag, Cu, Pt, Pd, and Au) were prepared by electrodeposition [46-48]. However, shape- and size-controlled synthesis of micro/nanostructures using electrodeposition has remained extremely challenging and there remains plenty of rooms to be explored.
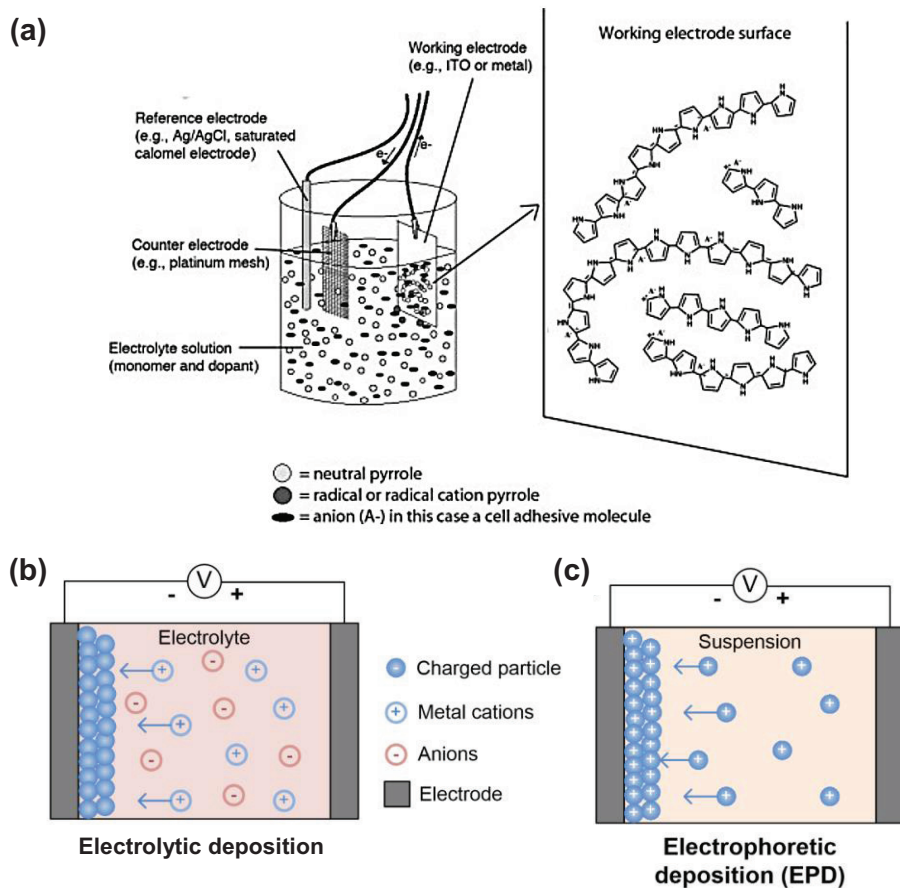
Figure 8. Schematic illustrations of typical electrochemical deposition processes of (a) conducting polymer nanomaterials, (b) electrolytic deposition and (c) electrophoretic deposition of metal nanoparticles [41,43].

1.1.3.2. Doping ratio control

The electrical properties of conducting polymers are easily modulated by altering their doping ratio (or oxidation level). To apply conducting polymers as substitutes of inorganic or conventional semiconductors, some higher conductivity is required than that of the undoped conducting polymers. Analogy with the doping of inorganic semiconductors, "doping" in conducting polymer is a process to convert neutral conducting polymers with low conductivity (typically in the range of 10^{-10} to 10^{-5} S cm^{-1}) into semi-conductive or conductive ones with higher conductivities (1 to 10^4 S cm^{-1}) through redox reactions [26, 49].

The concept of doping in conductive polymers has some similarities and differences with the doping of inorganic substances. Doping in both CP and inorganic semiconductor increases the conductivity and changes the oxidation states of materials. One difference is that the incorporation of dopant is interstitial in CP materials while it is substitutional in inorganic semiconductor [50]. Thus, the dopant plays the role of creating additional charges in inorganic semiconductors, but in CP, the dopant is responsible for neutralizing the additional charges generated by the inflow/outflow of electrons. Another

difference is that the doping is reversible in CP materials.

Except for a few cases, most of the conducting polymers are reported as p-type. The p-type doping can be defined as the removal of electrons from the valence band, from highly occupied molecular orbital (HOMO) of conducting polymer by oxidizing agents. The oxidizing agent is usually electron-attracting substance and it acts as an electron acceptor or p-type dopant. After p-type doping, positively charged conducting polymer chains and negatively charged counter ions form an ionic complex [51].

A variety of doping control techniques are available including chemical, electrochemical, in-situ, photo, and charge injection doping [51]. Among these, electrochemical doping method is advantageous over other methods because the doping/dedoping process is highly reversible and it allows precise control of doping level and homogeneous distribution of dopants in CPs. Also, the information about the amount of charge used up in the doping reaction can be easily obtained. Electrochemical doping is usually carried out in three-electrode set-up (**Figure 11a**). The electrode supplies the redox charge by donating or withdrawing electrons to/from the conducting polymer, and ions diffuse from the nearby electrolyte into (or out of) the

polymer to compensate the charge. The p-type doping is anodic oxidation of a conducting polymer which can be done by immersing CP coated negative electrode within dopant electrolyte. Commonly used supporting electrolytes are quaternary ammonium salts of the R_4NX (where R=alkyl, aryl group and X=Cl^-, Br^-, I^-, ClO_4^-, BF_4^-, PF_6, $CF_3SO_3^-$, $CH_3C_6H_4SO_3^-$) that are soluble in an aprotic solvent.

The doping affects the band gap energy of the conducting polymers by introducing the defects into the conducting polymer matrix such as soliton, polaron, and bipolaron. **Figure 9** shows the four states of orbital or band structures of PPy. The neutral state PPy is an insulator and it is characterized by a large band gap of *ca.* 3.2 eV [52]. At low p-doping level, the dopant accepts a single electron or a pair of electrons from the polymer, and soliton is formed. At this state, the independent charge defects are observed because bonding electrons having an identical energy state are separated to an opposite orientation, similar to the degenerate ground state. If further charge transfer occurs between soliton and neutral conducting polymer, the radical cation is formed which is called polaron. The formation of polaron induces two localized electronic states (bonding and antibonding) within the band gap while the unpaired single electron

occupies the bonding state. By further oxidation of polaron, a couple of electron transfers with the dopant, which results in the formation of a dication (also called bipolaron). For bipolaron, two new localized electronic states are located within the band gap containing an unpaired single electron by each. At heavily doped state (higher oxidation level), the two bipolarons can overlap to form a bipolaronic band [4,51].

$$PPy \xrightarrow{A} PPy^{\bullet}A^{\bullet}$$

$$PPy \xrightarrow{Oxidized} PPy^{+}A^{-}$$

$$PPy_1^{+}A^{-} \xrightarrow{PPy_2} (PPy_1\ PPy_2)^{\bullet +}A^{-}$$

$$PPy^{+}A^{-} \xrightarrow{A} PPy^{2+}2A^{-}$$
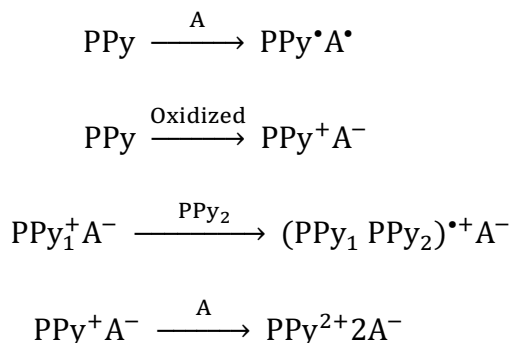
The doping/dedoping process is highly reversible until it reaches overoxidation state (**Figure 10**). If the polymer is excessively oxidized (i.e. when a too high potential is applied during electrochemical doping process), PPy loses its electroactivity and undergoes an increase in film thickness due to volume expansion. The positive –NH^{+}– of PPy is rearranged into –NH–, accompanied by loss of counter ions [53,54]. In the course of doping (oxidation), chain swelling occurs as counter ions are inserted (**Figure 11b** and **c**). If the

polymer is reduced, the polymer chain shrinks to form a compact structure [55].
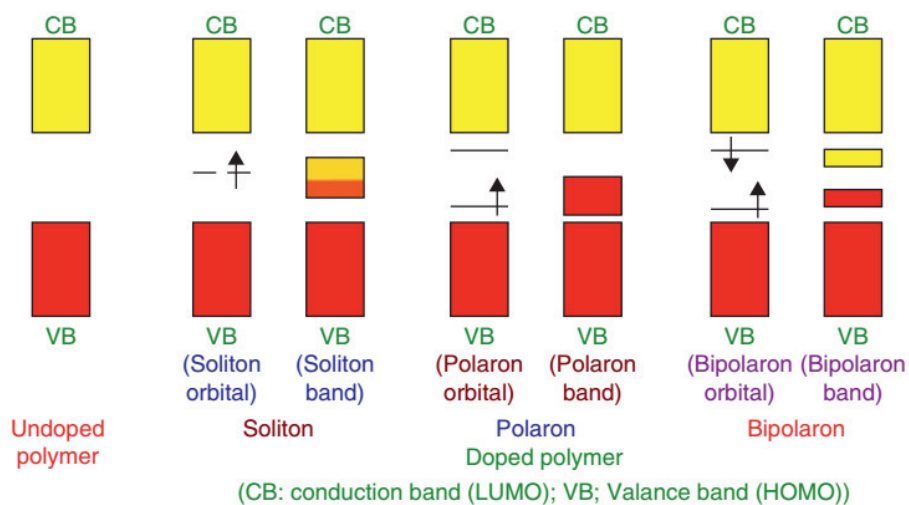
Figure 9. Electronic band model of PPy: neutral (undoped) state, soliton, polaron, and bipolaron of PPy [51].
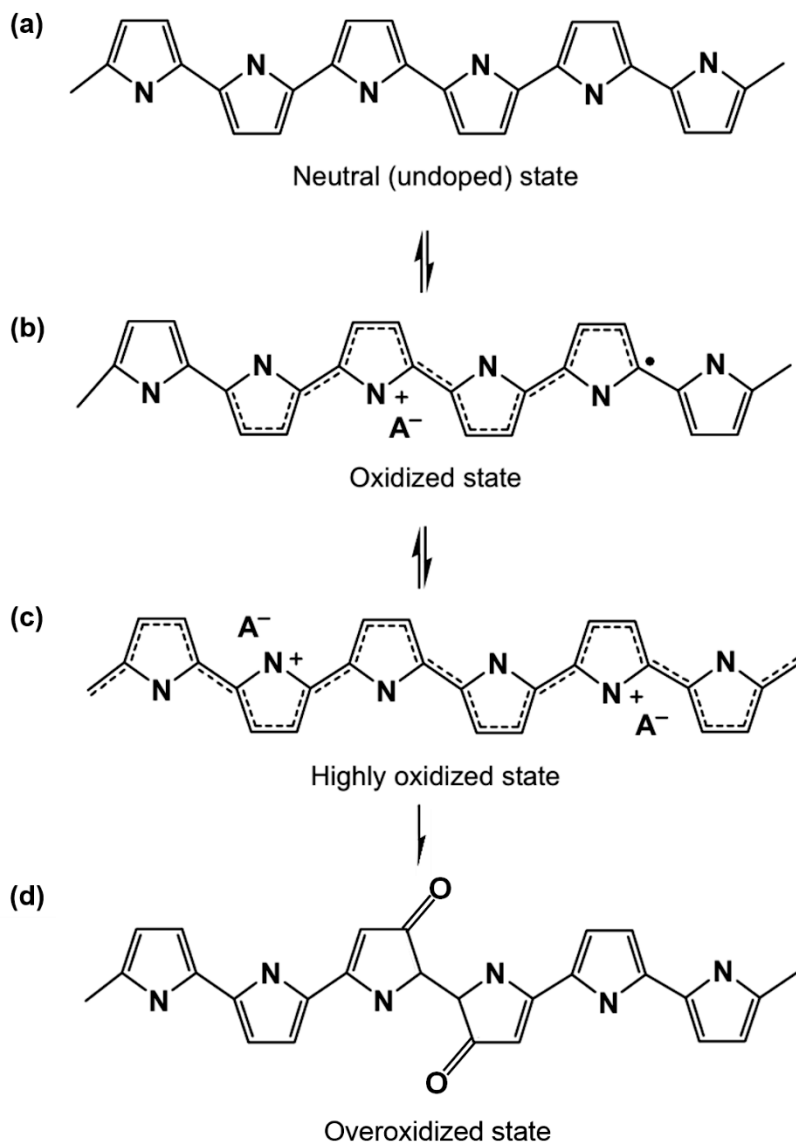
Figure 10. Molecular structures of (a) neutral state, (b) polaron, (c) bipolaron, and (d) overoxidized PPy [4,53].

(a)

(b)

(c)

Shrink (reduction)   **Swell (oxidation)**
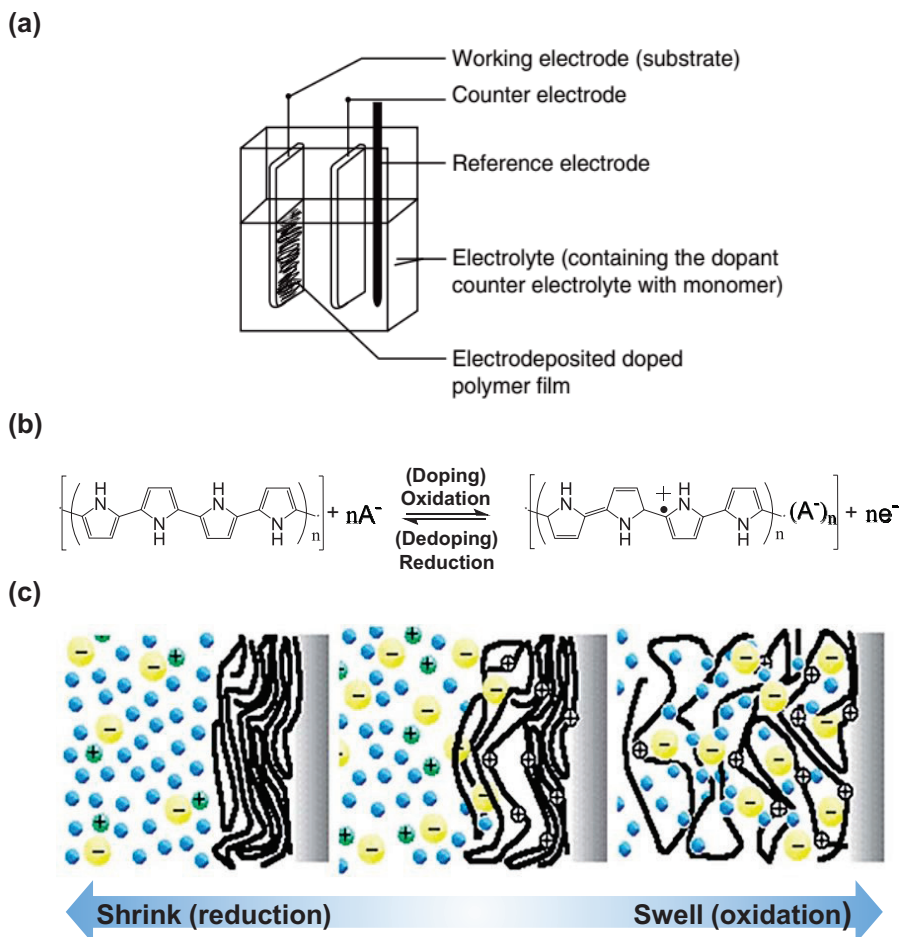
Figure 11. (a) Schematic illustration of a three-electrode system for electrochemical doping. (b) Change in double bond distribution of polypyrrole chain during doping/dedoping process. (c) Plain view illustration describing chain shrinking/swelling during electrochemical doping control [51,55].

1.1.3.3. Aptamer functionalization

Bioreceptors play a key role in the detection and quantification of molecules in analytical chemistry as well as in other research fields. Similar to the key-and-lock theory of enzyme-catalyzed reaction, numerous molecules are designed to have binding specificity. Antibodies are the most popular and classic examples of bioreceptors. Also, proteins, aptamers, DNAs, and natural receptors are recently used (**Figure 12a**) [56].

Technologies are evolving to detect a wider range of molecules more specifically and precisely. Hence, there is a growing need for new bioreceptors to meet this demand. Antibodies have excellent specificity to target analytes, but they also have some shortcomings that may offset them. Since producing antibodies requires extraction and cultivation from cells or bioreactors, it is time- and cost-consuming, and performance of the product varies from batch to batch. Besides, antibodies have a limited shelf life due to their sensitiveness to temperature.

Aptamers are single-stranded oligonucleotides artificially designed to bind with specific target molecules. It is chemically synthesized in vitro method called systematic evolution of ligands by exponential

enrichment (SELEX): prepare a pool of oligonucleotides with slightly different sequences and screen out the one that has the highest affinity to the target among them. Aptamers have several advantages over antibodies such as fast automated synthesis, a wide variety of targets, facile chemical modifications, small size, and longer shelf life [56,57]. These attributes of aptamers may fulfill the demands in the development of therapeutic and diagnostic tools.

To integrate bioreceptors into a biosensor system, bioconjugation process is necessary because a CP by itself lacks the specificity toward target analyte. The bioreceptors are immobilized onto the substrate or active sensing layer of the biosensor by crosslinking or physical adsorption (**Figure 12b**). For crosslinking, crosslinking reagents are used to trigger the conjugation between functional groups (such as amines, carboxylic acids, aldehydes, and sulfhydryls) of bioreceptors and the substrate [58]. To form functional groups on the surface of the conducting polymer which is the material for the active sensing layer, various methods can be used, such as copolymerizing a mixture of plane monomer and functional monomer, adsorbing 1-pyrenebutanoic acid succinimide ester (PSE) by π-π interactions, and surface oxidation by immersing in an acid solution.

(a)
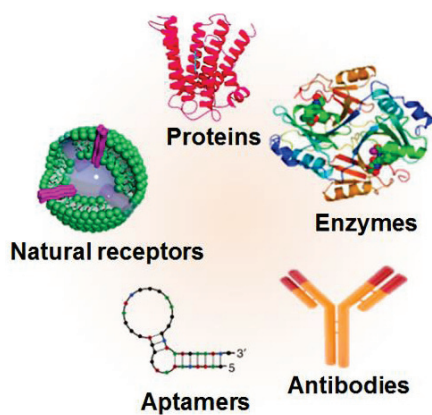
(b)
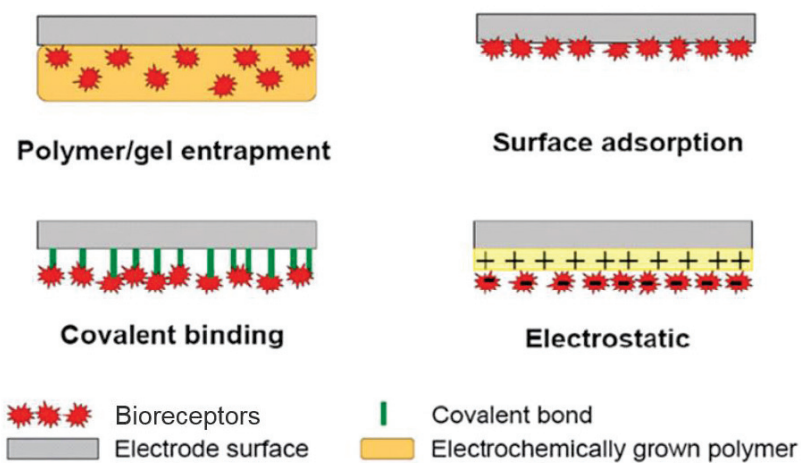
Figure 12. (a) Several examples of bioreceptors. (b) Common methods of bioconjugation of bioreceptors [58].

1.1.4. Sensor applications

Sensors are devices that are designed to detect changes in the environment and convert into readable signals. The signals are then sent to the data processor, which gives useful information to the users. We are experiencing sensors in virtually every part of real life, either directly or indirectly; internet-of-things, artificial intelligence, mimicking human senses (e.g., see, hear, touch, smell, taste). Sensors can be classified into two major groups, chemical sensors and biosensors. There are five indices to characterize the sensor performance: 1) high sensitivity 2) high selectivity 3) rapid response and recovery time 4) operation ability at room temperature 5) durability. The pursuit of realizing high-performance sensor is ongoing through ameliorating active layer materials, electrode configurations, and device types. Recently, multidimensional nanomaterials have been emerged as excellent sensing transducers to boost sensitivity for target analyte through enhancing the active surface area.

1.1.4.1. Chemical sensor

Chemical sensors are analytical devices that convert chemical information such as concentration, partial pressure, and presence of particular molecules into interpretable signals. Chemical sensors usually encompass the detection of gaseous compounds. A chemical sensor consists of two main components: an active sensing material that selectively interacts with analyte gases to produce various output signals (such as photometric, electrochemical, calorimetric, mechanical signals) and a signal transducer which transforms these signals into digital signals (**Figure 13**) [59].

Chemical sensor technologies are applied in numerous fields such as industrial, medical, and agricultural fields. If it had initially started as a simple detection tool, now demand for chemical sensors is tremendously increasing as people are seeking to integrate sensor data into big data and portable device technologies.

Resistive chemical sensor, also called chemiresistive sensor, is a type of chemical sensor that observes the resistance change in a sensor upon exposure to different concentrations of target gases. It has a simple device geometry with active sensing layer placed in between a set of metal electrodes [5]. Many studies are focused on the

chemiresistive sensor because it allows miniaturization, simple fabrication, and high sensitivity. The underlying working principle behind chemiresistive sensing is very straightforward. The chemical reaction with the target gas accumulates or depletes electrons from the sensing layer.

(a)
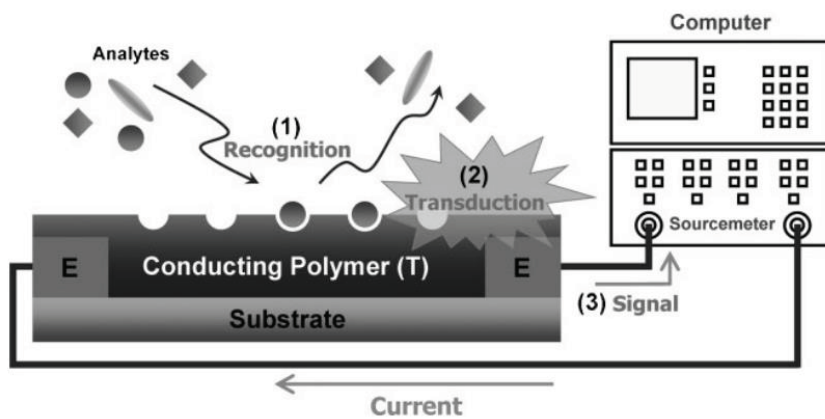
(b)
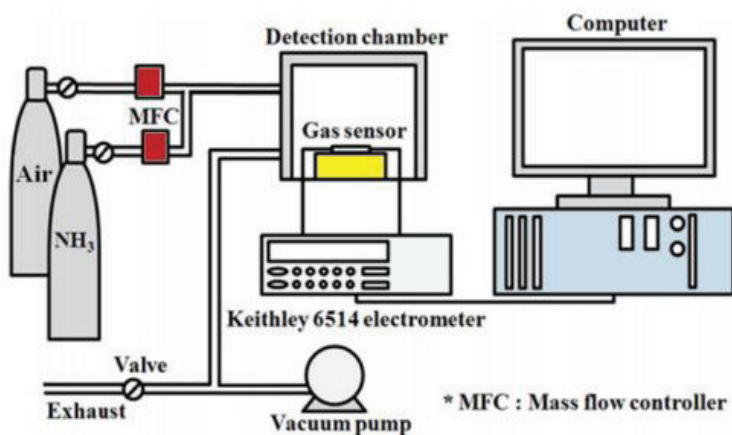
Figure 13. Schematic illustration of (a) sensing mechanism of a chemiresistive gas sensor and (b) typical setup for gas sensing experiment [5,60].

1.1.4.1.1. Hazardous gas chemical sensor

Diverse chemicals can be detected by chemical sensors including volatile organic compounds (VOCs), humidity, hydrogen (H_2), nitrogen dioxide (NO_2), and hydrogen sulfide (H_2S). Volatile organic compounds (VOCs) are compounds that spontaneously vaporize in room temperature. They are mostly released from consumer products or burning fossil fuels. Acetone, ammonia (NH_3), alcohols, and organic vapors fall into this category.

Ammonia is a nitrogen derived compound which is universally used as fertilizers, a precursor to nitrogenous compounds, building blocks of pharmaceuticals, antimicrobial agent for food, and source for deposition of silicon nitride [61]. However, ammonia gas can be extremely toxic to the human respiratory system, for example, exposure limit for long term period is 25 ppm and for short term is 35 ppm [62]. Therefore, developing highly sensitive and effective sensor equipment is necessary for commercial and industrial needs, as well as to take into account the hazard to the human body.

Semiconducting metal oxides such as SnO_2, ZnO, TiO_2, In_2O_3 are classic materials for ammonia gas detection [63,64]. However, common drawbacks of these metal oxide-based sensors are that they

operate at high temperatures in order to achieve substantial sensitivity and the measurable concentration of ammonia is relatively high. Using organic materials including conducting polymer nanomaterials can solve the aforementioned problems. In particular, polypyrrole has room temperature applicability, exceptional sensitivity with the rapid response time. Ammonia gas withdraws protons on –NH groups in polypyrrole as it undergoes dedoping [65]. This process is almost reversible, so it can contribute to the durability of the polypyrrole-based ammonia sensor.

Aliphatic alcohols including methanol, ethanol, and propanol are very volatile due to low molecular weight and high vapor pressure. At low concentration, alcohol vapor can cause nausea and fatigue. It becomes toxic at higher concentration, causing various health problems such as the burning of nose and throat, visual disorders, and respiratory failure [66]. Especially methanol is a noxious chemical; if inhaled in large quantities, it can cause acute poisoning and fatal damage to the central nerve system. A Harmful threshold limit of methanol gas is 200 ppm. Methanol has recently been used as a coolant for metal working and solid fuel for camping because of its low price. However, it poses a great risk as the concentration of

methanol vapor can increase rapidly in the non-ventilating environment. For these reasons, demand for methanol sensor is increasing. Aliphatic alcohols are electron-donating species, hence it enhances the conductance of p-type conducting polymers (e.g., polypyrrole). Previously, Miramirkhani *et al.* reported alcohol sensors based on polypyrrole and polyaniline nanofibers [67]. However, chemiresistive ammonia sensors still suffer from high MDL, slow response/recovery times, and complex fabrications.

1.1.4.1.2. Hydrogen sensor

Hydrogen is a promising candidate for a clean energy source to replace fossil fuels because its emissions are only water. It also has the highest heat of combustion with low density (0.0899 kg m^{-3}) and boiling point (20.39 K) [68]. It is widely involved in industrial fields including petrochemical production and refinery, chemical compound synthesis, power plants, electronics, fuel-cell applications, and aerospace industries [69-73]. Despite many benefits, it is difficult to handle hydrogen because a leak causes a massive explosion if the concentration is over 4 vol% in air. Hence, safe storage, transport, and constant vigilance of leakage are a critical issue when working with

hydrogen gas. Since hydrogen is a colorless, odorless and tasteless gas, a high performing sensor is required to detect the presence and concentration of hydrogen.

The sensors for hydrogen need to have selectivity and sensitivity at the ambient condition that can detect trace amounts of hydrogen (ppm levels) near the lower explosive limit (4 vol% in air). In addition, the sensors will be more valuable if they provide fast response time, long-term usability, low prices, and simple manufacturing methods. Some technologies for hydrogen sensors include gas chromatographs, surface plasmon resonance [74].

In resistive hydrogen sensor, the hydrogen gas is adsorbed to the active material and subsequently dissolved into the active material. The phase of the active material changes and it eventually deviates the resistance of the sensor. Noble metals such as Pd, Pt, and Au are good active materials for sensors due to their outstanding catalytic activity and solubility of hydrogen [75]. Pd is one of the most exclusively studied materials for hydrogen sensing because it has unique chemical property; it goes through a phase transition from palladium (Pd) to palladium hydride (PdHx) or volume expansion under hydrogen adsorption. To achieve low cost, sensitive, reproducible and

miniaturized sensor devices, Pd nanomaterials with various morphologies (nanoparticles, nanowires, porous films), alloy nanomaterials, composite materials with conducting polymers, graphene, metal oxides are gaining much interest in research [76,77].

1.1.4.2. Biosensor

Biosensors are analytical devices that detect biomarkers, which converts the biological signals generated from receptors and biomarkers into a measurable signal such as optical, piezoelectric, electrochemical, etc. Biomarkers can include cells, protein, chemicals, DNA, and enzymes (**Figure 14a**).

Until nowadays, biosensors are employed in early diagnose of diseases, water safety, food poisoning, environmental pollution, drug delivery, protein engineering, healthcare monitoring, and other bio-related applications [78-80]. Furthermore, the recent emergence of smartphones and mobile technologies are inspiring researchers to integrate biosensor into wireless and wearable electronics.

The performance of the biosensor can be assessed from various aspects. Sensitivity, selectivity, response time, minimum detectable level, detection range, reusability, shelf life, and stability are required criteria for high-performing biosensor. Through many years, building an outperforming biosensor that detects the ultralow concentration of target analyte in femto- and pico-level was one of the major research topics. To enhance the sensing performance, various types of sensor platforms and transducer materials are exclusively studied.

A field-effect transistor (FET)-based biosensor is one of the promising candidates among the various kinds of electrochemical biosensors, owing to their capability of rapid and sensitive detection of target analytes that originates from high signal-to-noise (S/N) ratio and current amplification.

In general, the structure of a liquid-ion gated FET sensor consists of 3-terminal (source, drain, gate) geometry and a liquid-ion (electrolyte) as illustrated in **Figure 14b** [81,82]. The source (S) and drain (D) are terminal conductors and they are connected through an active channel by Ohmic contact. An active channel is composed of semiconducting transducer materials such as Si, rGO, conducting polymers, and becomes an electrical pathway where charge carriers flow from S to D. The liquid-ion provides liquid-solid interfaces between the channel and electrolyte and acts as a gate dielectric when a gate (G) electrode is immersed in it.

The modulation of G voltage can adjust the current flow between the S and D electrodes. The detection mechanism of a target analyte is described as following: when the target analyte is dissolved into an electrolyte solution, it binds to the recognition moieties of the bioreceptors immobilized on the surface of the transducer. This

interaction alters the local distribution of charge carriers at the transducer surface, thus acting as a gate voltage modulation. Because the change of electrostatic potential in transducer creates current variation, it is possible to bio-sense by monitoring the current change of FET sensor [83,84].

In recent years, conducting polymer nanomaterials drawn attractive transducer materials for FET-type biosensors, due to their synergistic effect with FET devices. CP nanomaterials have various advantages such as a large surface area for anchoring receptor molecules, simple fabrication and modification, biocompatibility, inherent electrical properties, etc.

(a)
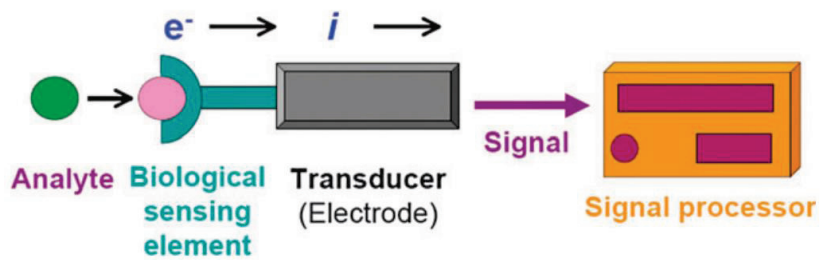
(b)
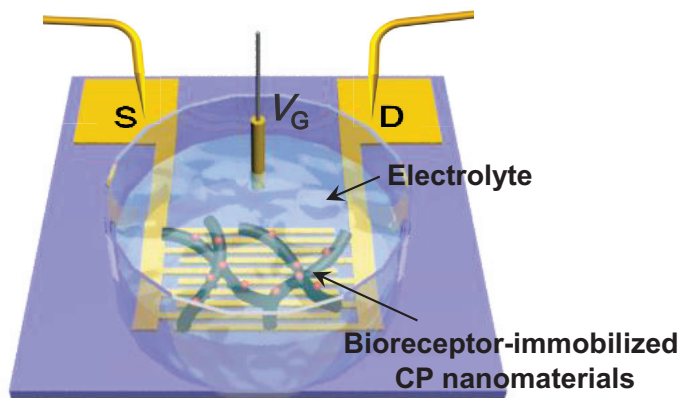
Figure 14. Schematic illustration of (a) biosensor operation mechanism and (b) liquid-ion gated FET biosensor system [81,82].

1.1.4.2.1. Hepatitis B virus surface antigen sensor

Hepatitis B virus (HBV) infection is a worldwide health problem which nearly 30% of the population are healthy carriers or currently under infection [85]. It is a major cause of chronic liver diseases such as liver cirrhosis, hepatocellular carcinoma, and liver failure. One of the important serological markers for diagnosing HBV infection is a hepatitis B virus surface antigen (HBsAg), an envelope protein of the hepatitis B virus (HBV) particle [86]. It can reflect the progress of the disease whether it is acute or chronic and predict the remedial effect in case of treatment of chronic one [87]. The antigen can be present in various body fluids including blood plasma, tears, semen and saliva [88-90]. Several approaches have been developed to detect HBsAg using chemiluminescence, fluorescence, surface plasmon resonance, and ELISA method [91-95]. While these methods can identify HBsAg, most of these approaches have limitations such as involvement of expensive antibody, a requirement of labeling steps to recognize sensing signal, and low sensitivity. Therefore, a new strategy for HBsAg detectors must be developed.

Recently, Deng *et al.* successfully isolated aptamer H01 that exclusively binds to HBsAg [96]. So far, various aptamers for

hepatitis C virus core/envelope protein, HBV core protein, and RNA aptamers were discovered, but DNA aptamer for HBsAg is reported for the first time [97-100]. From the fact that DNA aptamers are resistant to nuclease unlike RNA aptamers, it has the potential to be utilized in real-time detection of an analyte in body fluids.

In recent years, non-invasive assays that use saliva or sweat are getting the spotlight to replace conventional hematologic test. Most diagnostic tests require some incision of skin to collect blood samples. In contrast, saliva-based non-invasive diagnostics have several advantages: easy to collect, cost-effective, simple and safe to handle. To date, salivary assays for biomarkers such as antibodies, hormones, environmental toxins, certain drugs are proved to accurately reflect blood concentration [101-105]. Although many attempts have been made to identify biomarkers in saliva, it is still a challenging goal to attain sensitive and selective detection toward a specific target of extremely low concentration.

1.2. Objectives and Outlines

1.2.1. Objectives

The aim of this dissertation is to describe the methods for fabrication and modification of three-dimensional polypyrrole nanostructures and their application for various chemical/biosensors. In detail, three-dimensional polypyrrole nanowire-based conductive nanofilms were synthesized on either CVD graphene or IDA electrode substrate *via* electropolymerization of pyrrole. Subsequently, polypyrrole polymerization temperature/doping level controlled-conductive nanofilms, population/size of decorated Pd nanoparticle controlled-conductive nanofilms, polypyrrole nanowire aspect ratio/surface functionality controlled-conductive nanofilms are facilely prepared. The as-prepared three-dimensional polypyrrole nanowire-based conductive nanofilms are employed as efficient transducer materials for several chemical/biosensor applications detecting VOCs (NH$_3$/MeOH), hydrogen (H$_2$), and hepatitis B surface antigen (HBsAg). Furthermore, the effect of various modification variables on the properties of polypyrrole nanowire-based conductive nanofilms and the performance of the nanofilm-based sensors are thoroughly scrutinized.

1.2.2. Outlines

This dissertation focused on the fabrication and modification methods of three-dimensional polypyrrole nanowire-based conductive nanofilms and investigations of their performance as chemical and biological sensor electrodes. This dissertation involves the following subtopics:

I. Fabrication of three-dimensional microvillus-like polypyrrole nanowire-based conductive nanofilms for VOC gas sensor: Doping level control

II. Fabrication of Pd NP-decorated three-dimensional polypyrrole nanowire-based conductive nanofilms for hydrogen gas sensor: Size-control of Pd NP

III. Fabrication of multidimensional polypyrrole nanowire-based conductive nanofilms for FET-type HBsAg aptasensor: Surface functionality control

A detailed outline of the study is as follows:

1. Facile synthesis of three-dimensional polypyrrole nanowire-based microvillus-like conductive nanofilm (3D MCN) and its kinetic formation and doping level control are described to prepare a highly sensitive VOC gas sensors. 3D MCN is prepared *via* electropolymerization of pyrrole on the flexible graphene substrate. First, the morphology change of PPy nanostructures from nanowire to micrograin is generated by polymerization temperature control. Next, the oxidation level change of 3D MCN from neutral to overoxidation is achieved by an electrochemical doping control. Four different kinds of temperature-controlled 3D MCNs (5ºC, 20ºC, 45ºC, and 70ºC) and doping states (neutral, polaronic, bipolaronic, and overoxidation) of 3D MCNs are prepared as chemisresistive VOC sensor electrodes. The electron microscope is used to observe the morphology difference of 3D MCNs and electrical conductivity and FT-IR analyses are used to reveal the electrical characteristics and molecular structures. Real-time responses, flexibility, and repeatability data sets for VOC gases (ammonia and methanol) of different concentrations are collected to evaluate the performance of 3D MCN as a gas sensor electrodes.

2. Three-dimensional PPy nanowire structures decorated with Pd nanoparticles (PPyPds) is prepared as an efficient chemiresistive hydrogen gas sensor and facile fabrication strategy for population and size control of Pd NPs is described. First, PPy nanostructure is directly electrodeposited on interdigitated array electrode as the conductive template. The explore how the electrodeposition parameters effect Pd nanoparticle formation, the concentration of the precursor ($PdCl_2$; 0.1, 1, and 10 mM) solution and the temperature (5ºC, 60ºC, and 90ºC) are changed. Analytical tools such as FE-SEM, EDS, and XPS are used to observe the morphology, population, and size of the Pd nanoparticles formed on PPy. The sensitiviy and linear detection range of PPyPd sensor electrodes with different size of Pd NPs are assessed upon exposure to different concentration of hydrogen gas. The correlation between sensing performance and the Pd NP size is interpreted in terms of active catalytic surface area and conducting pathways.

3. Facile fabrication strategy for multidimensional conductive nanofilm (MCNF), consists of vertically oriented carboxylated polypyrrole nanowires grown on the graphene layer, is introduced to prepare a flexible HBsAg aptasensor transducer using

electropolymerization of pyrrole and following acid treatment. The immobilized amount of the HBsAg binding aptamers are controlled using different reaction times of the acid activation. The multidimensional structure of the sensor transducer, consisting of vertically aligned nanowires with a high length-to-diameter (L/D) ratio and sufficient surface modification by acid treatment, enhances the amount of aptamer loading. Diverse microscopic and spectroscopic measurements are conducted to investigate morphological and chemical changes of MCNF and quantify the aptamer immobilization. The sensitivity, response time, and flexibility of MCNF-based aptasensor toward HBsAg are examined. Furthermore, the ability of the aptasensor to discriminate target analyte (HBsAg) from human serum and saliva is also confirmed to prove the potential for the noninvasive diagnosis of HBV infection.

2. Experimental Details

2.1. Fabrication of three-dimensional microvillus-like polypyrrole nanowire-based conductive nanofilms for VOC gas sensor: Doping level control

2.1.1. Materials

Pyrrole (Py), sodium p-toluenesulfonate (pTSA), Bis(trifluoromethane)sulfonimide lithium salt (LiBis) were purchased from Sigma Aldrich. Sodium phosphate dibasic dodecahydrate(Dibasic) and sodium phosphate monobasic dihydrate (Monobasic) were purchased from Junsei Chemical Co. All chemical reagents were used as received without further purification.

2.1.2. Fabrication of three-dimensional microvillus-like polypyrrole nanowire-based conductive nanofilm

Three-dimensional microvillus-like polypyrrole nanowire-based conductive nanofilms (3D MCNs) were prepared on graphene-PEN film by using electrodeposition reaction in a 100 mL aqueous solution containing 0.1 mol pyrrole, 0.2 mol of sodium phosphates (Dibasic : Monobasic = 1 : 1 molar ratio), and 0.1 mol pTSA. The graphene-PET

film was prepared by chemical vapor deposition (CVD) and wet transfer method by as described in previous studies [106]. Electrodeposition was carried out at 5ºC under the constant potential of +0.8 V for 15 min in a three-electrode cell consisting of a Pt wire, Ag/AgCl, and CVD graphene-PEN film as a counter, reference, and working electrode, respectively. After electrodeposition, the 3D MCNs were rinsed with deionized (DI) water and dried at room temperature. To investigate the growth of polypyrrole with temperature, the electrochemical cell was placed in hot water bath and electrodeposition was held in the same manner as described earlier..

2.1.3. Doping level control of three-dimensional microvillus-like polypyrrole nanowire-based conductive nanofilms

Doping level control of the conductive nanofilm was conducted by potentiostat mode using a three-electrode cell with 50 ml of 0.1 M LiBis aqueous electrolyte. Pt wire, Ag/AgCl, and 3D MCNs were used as a counter, reference, and a working electrode, respectively. A constant voltage was applied to the conductive nanofilm electrode for 3 min and the voltage was changed from -1.6 V to +1.4 V stepwise with 0.2 V intervals. Electrical resistance was measured by the 4-

probe method with a source meter right after each voltage applying step was finished. Doping level controlled conductive nanofilm was rinsed with DI water and dried at room temperature.

2.1.4. Characterization

Field-emission scanning electron microscopy (FE-SEM) images were obtained by JSM-6701F (JEOL Ltd., Japan). Raman spectra were obtained using DXR2xi (Thermo, USA) installed at NCIRF at Seoul National University. X-ray photoelectron spectroscopy (XPS) data were acquired with Sigma Probe (Thermo, USA). Electrical conductivity was measured with Keithley 2400 and charge amount was recorded with electrochemical workstation WBCS3000 (Wonatech, Korea). All electrodeposition and oxidation level control were carried out using WBCS3000. Electrical conductivity, charge carrier mobility, and charge carrier density were calculated using following equations:

Electrical conductivity:

$$\sigma = \frac{L}{RA}$$

L: Length of the conductive nanofilm

A: Area of the conductive nanofilm

R: resistance measured by sourcemeter

Charge carrier mobility:

$$\mu = \frac{\sigma}{n_0|e|}$$

n_0: Charge carrier density

$|e|$: Electrical charge of an electron or a hole.

Charge carrier density:

$$n_0 = \frac{q}{V}$$

q: Charge amount from CV data recorded during oxidation level control

V (= twL): Volume of the conductive nanofilm.

t: Thickness of the conductive nanofilm

w: Width of the conductive nanofilm

L: Length of the conductive nanofilm

2.1.5. Electrical sensing measurement for VOC gas sensor

Gas sensor electrode was prepared by painting Ag paste to both ends of oxidation controlled-3D MCN film so as to have a distance of 1 cm

and attaching a copper wire thereto. The sensor electrode was placed inside a one-side-opened gas chamber and connected to a source meter to monitor the resistance change with a computer. In this experiment, a bubbler was used to vaporize organic compounds from ammonia and methanol solution and to mix vapors with nitrogen (N_2) gas to control the concentration of analyte gases. The sensor electrode was exposed to various concentrations of analyte gases (0.001 ppm – 100 ppm) for 100 s and purged with N_2 gas to recover the conductance. The measurement was conducted by applying a constant current of 10^{-6} A to the electrode and the sensitivity was calculated by measuring the normalized electrical resistance change:

$$\Delta R/R_0\ (\%) = (R - R_0)/R_0 \times 100$$

R: real-time measured resistance

R_0: initial measured resistance

In addition, the response time was defined as the time required for a sensor to reach 90 % of maximum sensitivity value after the gas exposure and the recovery time as the time taken for a sensor to reach 10 % of the preceding sensitivity after purged with N_2 gas.

2.2. Fabrication of Pd NP-decorated three-dimensional polypyrrole nanowire-based conductive nanofilms for hydrogen gas sensor: Size control of Pd NP

2.2.1. Materials

Pyrrole monomer (98%) and sodium *p*-toluenesulfonate (95%) were purchased from Sigma-Aldrich. Sodium phosphate dibasic dodecahydrate and monobasic dihydrate were obtained from Junsei Chemical Co. Palladium chloride ($PdCl_2$, 99%) was purchased from Sigma-Aldrich. All reagents were used as received without further purifications.

2.2.2. Fabrication of Pd NP-decorated three-dimensional polypyrrole nanowire-based conductive nanofilms

The Fabrication of Pd NP-decorated three-dimensional polypyrrole nanowire-based conductive nanofilms (PPyPd) was fabricated from electrochemical deposition of Pd nanoparticles on the PPy nanowire arrays. The PPy nanowire arrays, which is the template for Pd electrodeposition, follows the same synthetic protocol as our previous work [106]. First, interdigitated-array (IDA) microelectrodes was prepared by following manufacturing process. A positive photoresist

(AZ5214, Clariant Corp.) was coated onto a glass wafer by spin-coater, and patterns were formed via ultraviolet (UV) exposure through a high resolution film mask, followed by image reversal and development. The source and drain electrodes (Cr/Au, 20 nm/100 nm, respectively) were deposited by thermal evaporation followed by a lift-off process. The IDA microelectrode was then employed as a working electrode for the 3-electrode electrochemical cell experiment, and the PPy nanowire array was electropolymerized on it [107]. The resultant PPy@IDA was carefully washed with DI water and dried. Subsequently, this time the PPy@IDA was utilized as working electrode for the Pd electrodeposition. Pd electrodeposition was carried out at 0 V for 5 minutes at room temperature in an electrolyte consisting of 1 mM $PdCl_2$ in 0.01 M H_2SO_4 aqueous solution. All electrochemical experiments here were conducted with battery cell test system (WBCS3000, Wonatech) and Ag/AgCl and Pt wire were used as reference and counter electrode, respectively. PPyPds with controlled population of Pd NPs can be prepared by adjusting the concentration of Pd precursor of the electrolyte to 0.1, 1, and 10 mM. To change the size of the nanoparticles with fixed population, electrodeposition was carried out using a 1 mM $PdCl_2$ electrolyte while varying the reaction

temperature to 5℃, 60℃, and 90℃.

2.2.3. Characterization

Surface morphologies and elemental analysis of various PPyPd films were obtained from a field-emission scanning electron microscope (JSM-6701F, JEOL) equipped with energy dispersive X-ray spectroscopy (EDS) accessories (Inca). Transmission electron microscope (TEM) images were acquired using JEM-3010 (JEOL) installed at the National Center for Inter-University Research Facilities (NCIRF) at Seoul National University. X-ray photoelectron spectroscopy (XPS) analysis were carried out with Sigma Probe (Thermo, USA). XRD pattern was obtained from X-ray diffractometer (Smartlab, Rigaku).

2.2.4. Electrical sensing measurement for hydrogen gas sensor

PPyPd sensor electrode was prepared by forming bonds between Ag wires and the source and drain pads, respectively, of the PPyPd functionalized IDA electrode by painting Ag paste on the joint part. Then, the as-prepared PPyPd sensor electrode was placed inside the gas chamber and connected to the sourcemeter (Keithley 2400) to measure

the resistance change upon gas exposure. Various concentrations of hydrogen gas were injected into a chamber through a mass flow controller (MFC, KNH instruments) in order to observe the resistance change depending on the gas concentration. A constant current (10^{-4} A) was applied to the sensor electrode while monitoring the resistance of the electrode in real-time. The resistance change was represented as the normalized resistance change by calculating the percent change relative to the baseline resistance value. The sensitivity to H_2 target gas was defined as a normalized resistance change using the following equation:

$$\Delta R/R_0 \ (\%) = (R - R_0)/R_0 \times 100$$

R_0: initial resistance of the sensor exposed to carrier N_2 gas

R: resistance after contact with H_2 gas diluted with N_2

Target gas was injected and the gas inlet was turned on by waiting until the saturation was observed in the resistance change and purged with nitrogen gas for the same time duration. The ppm concentration of the target gas was varied by adjusting the flowrate of diluting nitrogen (slm) and hydrogen gas (sccm). The evaluation of sensing performance was held in ambient condition at relative humidity of *ca.* 20%.

2.3. Fabrication of multidimensional polypyrrole nanowire-based conductive nanofilms for FET-type HBsAg aptasensor: Surface functionality control

2.3.1. Materials

Pyrrole (98%) and sodium p-toluenesulfonate (95%) were purchased from Sigma Aldrich. Sodium phosphate dibasic dodecahydrate and monobasic dihydrate were purchased from Junsei Chemical Co. and used as received. Recombinant hepatitis B virus surface antigen (HBsAg) protein was purchased from Abcam. HBsAg ssDNA aptamer was adapted from the literature and was synthesized by Bioneer Co. (Daejun, Korea) [96]. Aptamer is terminated with an amino modifier C6 at the 5'–end, of which sequence is 5'-NH_2C_6-GGG AAT TCG AGC TCG GTA CCG GCA CAA GCA TAT GGA CTC CTC TGA ACC TAC GAT GTA GTA CCT GCA GGC ATG CAA GCT TGG-3'. The aptamer stock solution was diluted with PBS buffer solution (pH 7.4) and was stored at -20°C until use.

2.3.2. Fabrication of the CVD graphene substrate

Monolayer graphene was synthesized on copper foil through chemical vapor deposition (CVD) method by using CH_4 gas as a

carbon source. First, the copper foil was placed into furnace chamber and H_2 gas (8 sccm) was introduced. The gas flow was stabilized for 30 min to keep up a pressure of 147 mTorr. The furnace was heated up to 1000°C at 40°C min^{-1} and was held for 30 min. Subsequently, CH_4 gas (20 sccm) was supplied with maintaining of 560 mTorr pressure. Finally, the chamber was rapidly cooled to 200°C. Then, PMMA solution was spin coated on the CVD graphene surface and the copper foil was removed using etchant solution. The PMMA coated-graphene film was transferred to polyethylene naphthalate (PEN) substrate and the transferred graphene was dipped into the acetone to discard the PMMA coating layer on the graphene surface.

2.3.3. Fabrication multidimensional polypyrrole nanowire-based conductive nanofilms

For the generation of the vertically oriented polypyrrole nanowires on the graphene surface, graphene transferred-PEN film (1.5 cm x 0.5 cm) was used to working electrode in the electrochemical cell. The electrolyte solution was prepared by dissolving 0.1 mol pyrrole monomer, 0.2 mol of sodium phosphates (sodium phosphate dibasic vs sodium phosphate monobasic = 1 vs 1 molar ratio), and 0.1 mol

sodium *p*-toluenesulfonate into 100 mL distilled water. Pt wire and Ag/AgCl act as a counter and a reference electrode in the cell. Then, electro-polymerization was carried out on the working electrode surface using constant voltage (0.8 V) for 25 min at 5°C. To form the carboxyl group on the polypyrrole surface, the as prepared electrode was soaked into acid mixed solution (composed of equal volume of 1 M HNO_3 and 1 M H_2SO_4) for several hours (from 1 to 12 h) at room temperature. Subsequently, the acid treated electrode was washed with distilled water several times and dried.

2.3.4. Characterization

FE-SEM images were obtained with a JSM-6700 F microscope (JEOL, Japan) and HRTEM images were taken with JEM-3010 (JEOL) microscope. FT-IR spectra were collected with a Perkin Elmer Frontier spectrophotometer in ATR mode. Raman spectra were recorded with a LabRam Aramis (Horiba-Jobin Yvon) spectrometer. XPS data were obtained with AXIS-HS (KRATOS) instrument. Aptamer loading amount was measured with NanoQuant Plate (Infinite M200, TECAN trading) UV spectrophotometer.

2.3.5. Electrical sensing measurement for FET-type HBsAg aptasensor

To construct a aptasensor electrode, HBsAg binding aptamer (0.1 μM) and 1 wt% aqueous 4-(4,6-dimethoxy-1,3,5-triazin-2-yl)-4-methylmorpholinium chloride (DMTMM, 40 μL) solutions were incubated on the nanofilm surface for 6 h. Afterward, the aptamer functionalized multidimensional conductive nanofilm-based electrode was carefully rinsed with PBS (pH 7.4) and dried at room temperature.

All electrical measurements were conducted with a Keithley 2612A source meter, MS TECH, model 4000 probe station, and a Wonatech WBCS 3000 potentiostat. To utilize the solution-based measurement, a solution chamber (250 μL volume) was designed and used. The change in the current is normalized as follows:

$$[\Delta I/I_0]_{SD} \ (\%) = \frac{I - I_0}{I_0} \times 100$$

I_0: measured initial current

I: measured real-time current

Human serum (H4522, Sigma Aldrich) was diluted to 1 % aqueous solution with distilled water. Artificial saliva was produced according to the published recipe as follows: 25 mM K_2HPO_4 (0.1 L), 24 mM Na_2HPO_4 (0.1 L), 150 mM $KHCO_3$ (1 L), 1.5 mM $MgCl_2$ (0.1 L), 100

mM NaCl (0.1 L), 25 mM citric acid (0.006 L), 5 mM $CaCl_2$ (0.1 L) [108]. Furthermore, commercially available oral rinse (Biotene®, GSK, USA) was added to give a viscosity similar to actual saliva.

3. Results and Discussion

3.1. Fabrication of three-dimensional microvillus-like polypyrrole nanowire-based conductive nanofilms for VOC gas sensor: Doping level control

3.1.1. Fabrication of three-dimensional microvillus-like polypyrrole nanowire-based conductive nanofilms

Figure 15 suggests the overall process for the fabrication of three-dimensional microvillus-like conductive nanofilms based on the electro-polymerization technique. As a template for the polymerized conductive nanostructure, monolayer graphene was introduced onto a poly(ethylene naphthalate) (PEN) substrate using wet transfer method. To decorate microvillus-like polypyrrole nanostructures on the surface, the graphene transferred PEN substrate was immersed in a pyrrole dispersed electrolyte solution at low temperature (5°C). In the electrolyte solution, phosphate buffer maintains pH of the electrolyte during the polymer synthesis to prevent the influence of the generated hydrogen ions and *p*-toluenesulfonic acid (*p*TSA) acts as not only dopant but also soft-template of the pyrrole to form pyrrole contained micelle [109]. In the polymerization process, the pyrrole contained

67

micelles are adsorbed on the graphene surface to act as a template at the beginning of the polymerization (i.e., nucleation site). The generated nucleation sites prohibit growth of polypyrrole nanostructures in direction other than vertical direction due to the steric hindrance from the adjacent polypyrrole [110]. Then, the steric hindrance effect is enhanced with growing of the microvillus-like polypyrrole structure.

The morphology of the generated microvillus-like polypyrrole nanostructures is changed from nanowire to micrograin at different temperatures (**Figure 16-18**). At 5°C of polymerization, *ca.* 50-nm diameter of nucleation sites are uniformly formed on the surface and then vertically aligned polypyrrole nanowires (*ca.* 1 μm long with the diameter of *ca.* 70 nm) are decorated after following growth process. On the other hand, nucleation sites and nanowires grow larger and show more irregular with increasing reaction temperature. However, higher than 70°C cause thick coated polypyrrole films rather than nucleation sites and nanowires on the graphene surface. Especially, thickness of the aggregated part in the nanofilms is improved from 60 nm to 120 nm and diameter of the nanostructures is also enlarged up to 1 μm for 90°C (**Figure 19**). In addition, from a large scale aspect,

the generated polypyrrole nanofilms present micrometer scale pore generation at mid temperature (45°C to 70°C) and bumpy surface at high temperature range (**Figure 20**).

The morphology change of the polypyrrole nanostructures is originated from following mechanism (**Figure 21**). First, size of the micelles in the electrolyte is enlarged at higher reaction temperature due to improvement of hydrodynamic radius [111-113]. Then, the larger micelles generate increasing size of nucleation site and cause expanding diffusion area of the each nucleation site. The more expanded diffusion areas of the nucleation sites can induce overlap of each nucleus to form a bulk film on the substrate during the consequent incorporation process [114].
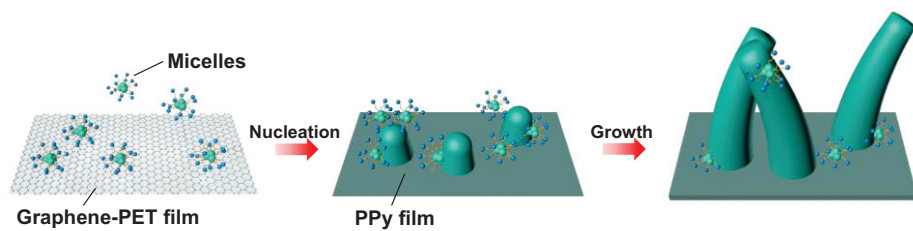
Figure 15. Schematic diagram of the sequential fabrication steps for the polypyrrole nanowire-based three-dimensional microvillus-like conductive nanofilm.
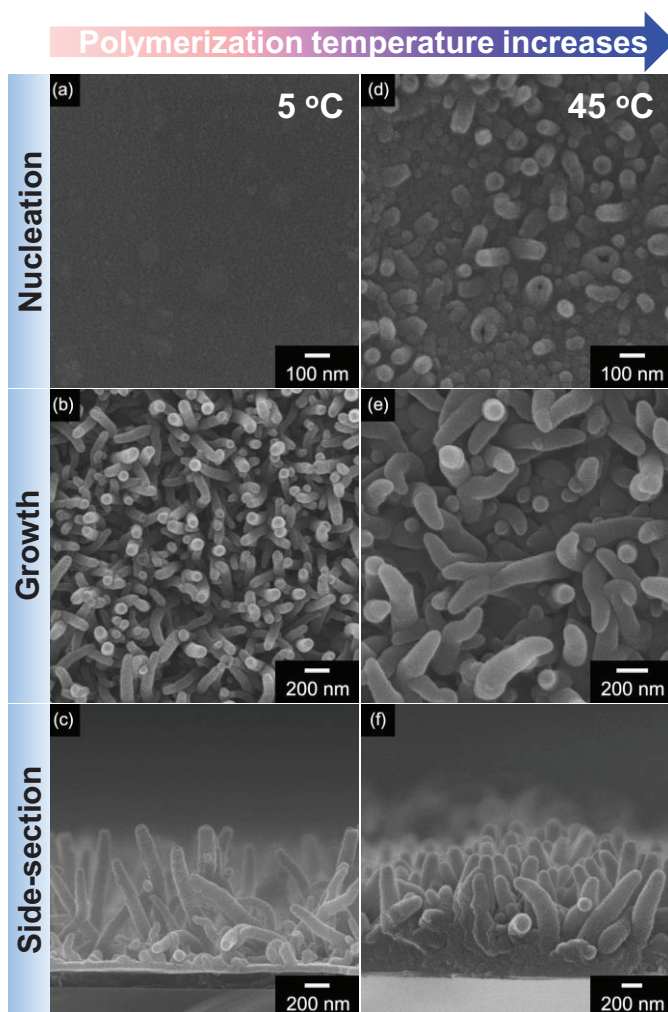
Figure 16. Field-emission scanning electron microscopy (FE-SEM) images of the polypyrrole nanowire-based conductive nanofilms during electrochemical polymerization of polypyrrole on CVD graphene substrate (nucleation and growth step) with different temperature: (a) – (c): 5ºC; (d) – (f): 45ºC.
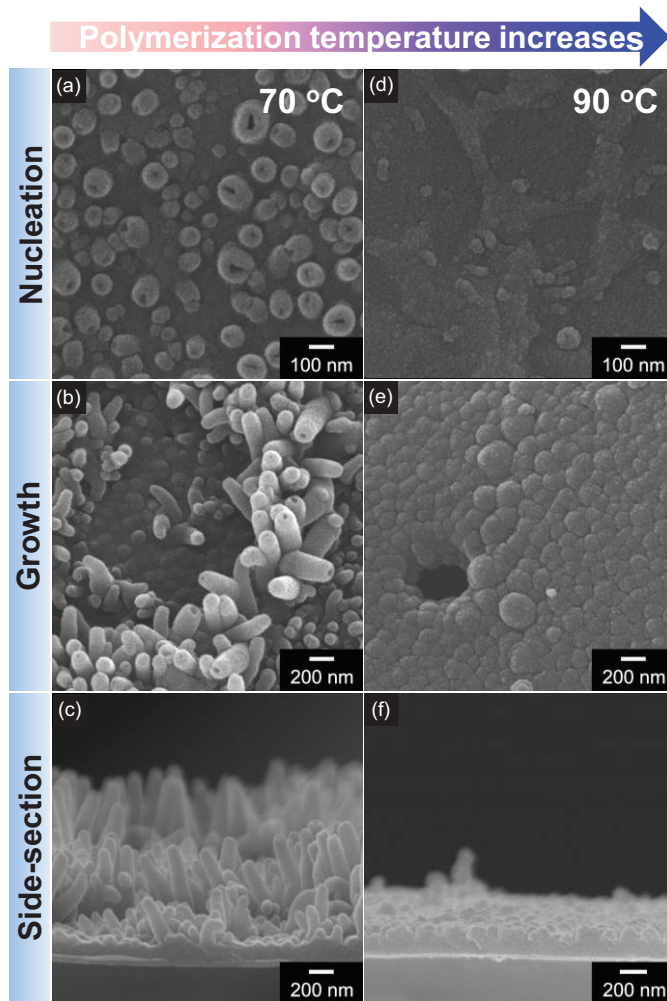
Figure 17. Field-emission scanning electron microscopy (FE-SEM) images of the polypyrrole nanowire-based conductive nanofilms during electrochemical polymerization of polypyrrole on CVD graphene substrate (nucleation and growth step) with different temperature: (a) – (c): 70ºC; (d) – (f): 90ºC.
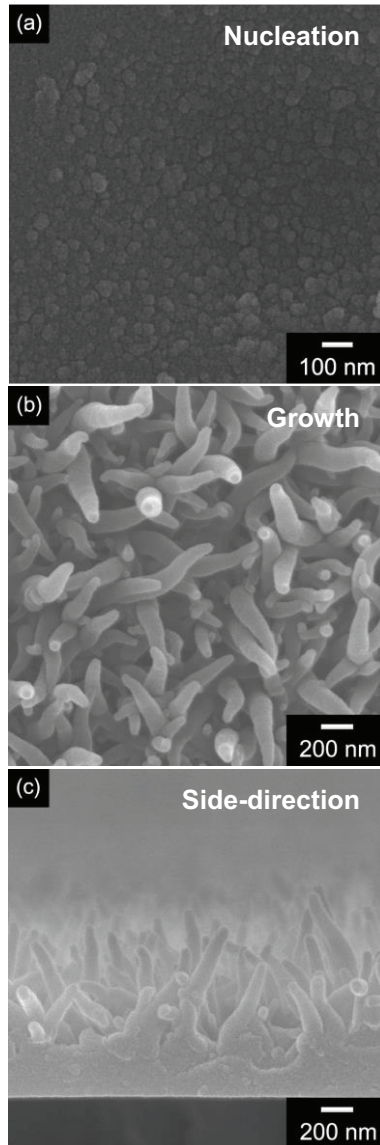
Figure 18. FE-SEM images of polypyrrole nanowire-based conductive nanofilm at 25°C during (a) nucleation step, (b) growth step and (c) side-direction images of (b).
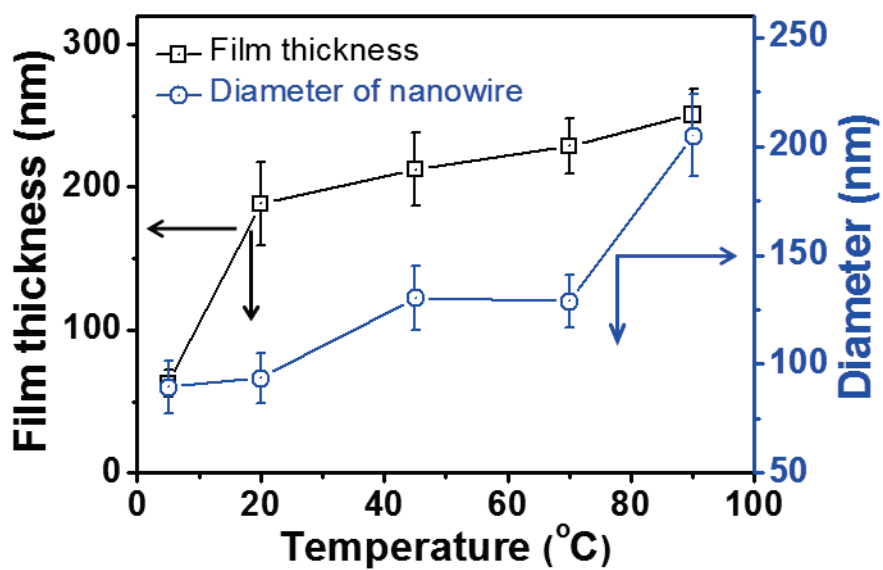
Figure 19. Thickness of nanofilms (black open square) and diameter of nanostructures in the conductive films (blue open circle) as a function of polymerization temperature.
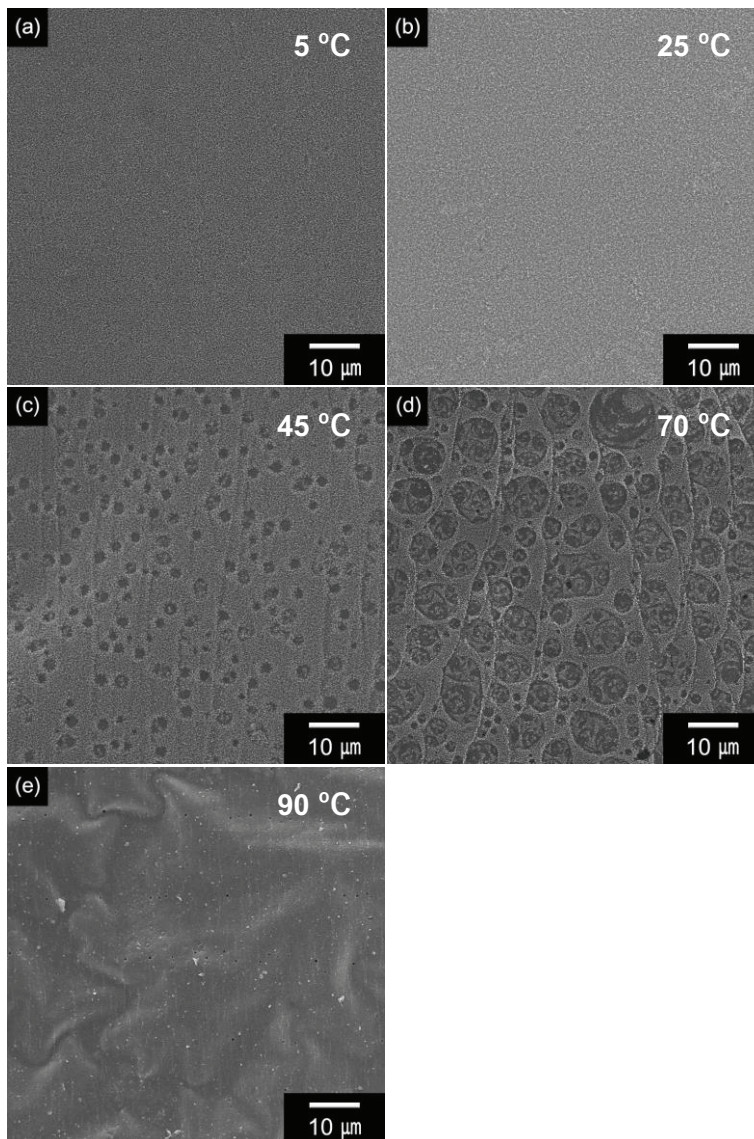
Figure 20. Low magnification of FE-SEM images of the conductive nanofilms with different electropolymerization temperature: (a) 5ºC, (b) 25ºC (c) 45ºC, (d) 70ºC and (e) 90ºC.
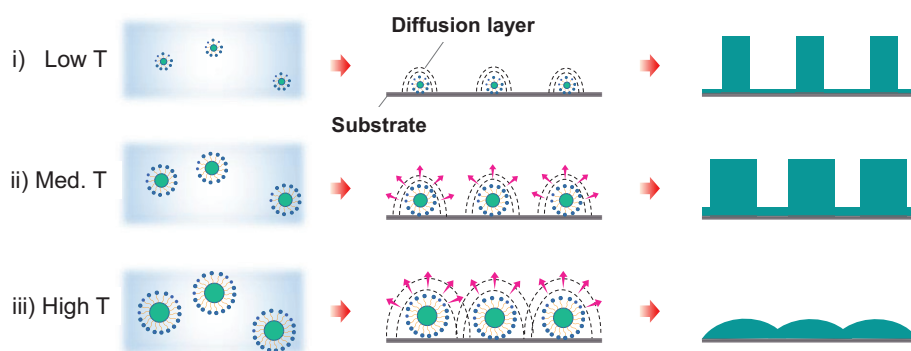
Figure 21. Illustrative formation mechanism of polypyrrole nanostructures with different temperature on the graphene substrate.

3.1.2. Characterization

The prepared microvillus-like conductive nanofilm that polymerized at 5°C suggests different chemical properties and morphology using electrochemical oxidation level control on account of transformation of the polymer chain structure that are neutral, polaron, bipolaron, and over-oxidation (**Figure 22**). **Figure 23** displays the electrical conductivity of the nanofilms with different oxidation levels (from -1.4 V to +1.4 V). The value of the electrical conductivity increases with enhancing oxidation levels because more positive potentials improve carrier densities (0.2×10^{18} – 1.31×10^{19}) in the polymer chains as shown in **Figure 24**. Especially, there are two increase of the electrical conductivity that are ranges from -1.4 V to -1.0 V and from 0 V to 0.6 V, respectively, due to charge transport property changes from neutral to polarons and from polarons to bipolarons. Consequently, the highest value of the electrical conductivity is 101.8 S cm^{-1} for +1.0 V of the applied potential. On the other hand, high applied potentials (from +1.3 V) acted as over-oxidation of the polymer films that cause promptly diminishing of the electrical conductivity (down to 1.3×10^{-3} S cm^{-1} at 1.4 V) despite of high carrier densities [115]. Moreover, following carrier mobility (μ),

originating from the electrical conductivity and carrier density ($\sigma = \mu eN$, where μ is carrier mobility, e is electron or hole charge, and N carrier density from charge current), represents enhancing up to +0.6 V potentials and rapid diminishing from +1.2 V, respectively, because of the improvement of the electrical conductivity with higher carrier density and the destruction of the polymer chain structures at the over-oxidation state.

Raman spectroscopy is acquired to further characterize the conductive nanofilms. **Figure 25** displays Raman spectra with different oxidation levels from -1.2 to +1.4 V. The bands at 1082 cm^{-1} and at 1332 cm^{-1} are characteristic of C-H in-plane and C-C stretching vibrations. In addition, the strong bands *ca.* 1410 cm^{-1} and *ca.* 1560 cm^{-1} are attributed to C=C symmetric and C=C asymmetric vibrations. In particular, these strong bands are shifted with enhancing amount of charge because of transformation of the polymer chains from the benzoid to quinoid structure with enhancing charged amount up to +1.4 V. Positive doped species (polaron or bipolaron) are located on a geometrical defect and formed quinoid structure. Therefore more positive voltages increase amount of (bi)polarons and change the polymer chains to quinoid [116]. In addition, the chemical

composition of the nanofilms is characterized using X-ray photoelectron spectroscopy (XPS). **Figure 26** presents new bond of the polymer chains using the N 1s region of the nanofilms with different voltage applications. The peaks *ca.* 400 eV, related to neutral amine nitrogen of the pyrrole unit (-NH-) and *ca.* 398 eV, correlated with imine (-N=), are shown in all cases. -0.2 V of potential causes emergence of a positive charged nitrogen ($-NH^+-$) peak ,assigned to polaron, at 401.4 eV. The more positive potentials (+1.0 V and +1.4 V) display bipolaron nitrogen peak ($=NH^+-$) at 403.0 eV. Consequently, increasing oxidation level of the polymer films presents development amount of positive charged nitrogen in the structure.

The morphology of the conductive nanofilm is reversibly changed for different oxidation levels using osmotic effect of the counter ion (Bis(trifluoromethansulfonyl)imide anion) [117]. When the electro-oxidation process occurs, electrons are ejected from the nanofilm and the positive charge in the polymer chain is developed. Then, the mobile anion in the electrolyte can move and create a volume expansion in the polymer by insertion of ions and the subsequent uptake of the solvent. However, excess electro-oxidation (i.e., over-oxidation) causes irreversible volume expansion of the polymer

nanostructure. Consequently, from a large film area of view, the conductive nanofilm of over-oxidation (at +1.4 V) displays cracks in the structure and a part of it falls off on the PET substrate (**Figure 27**). Then, it is extremely weak to the external impact and becomes losses electro-activity. Moreover, for an individual nanowire aspect, the diameter of the nanowires is enhanced from 67.7 nm of -1.2 V to 85.6 nm of +1.4 V with broadening of a deviation (**Figure 28**). The morphology of the nanowires is also changed as the middle hole expanded into the nanotube (**Figure 29**).

Neutral (-1.2 V)

Polaron (-0.2 V)

Bipolaron (+1.0 V)

Over-oxidation (+1.4 V)
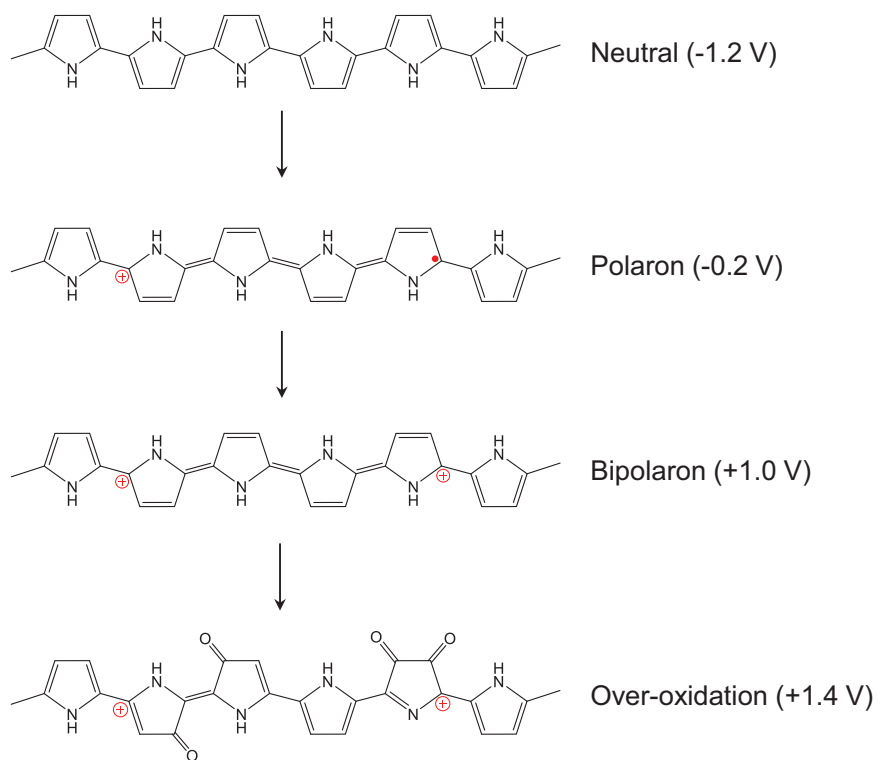
Figure 22. Chemical structures of polypyrrole chain at different chemical states.
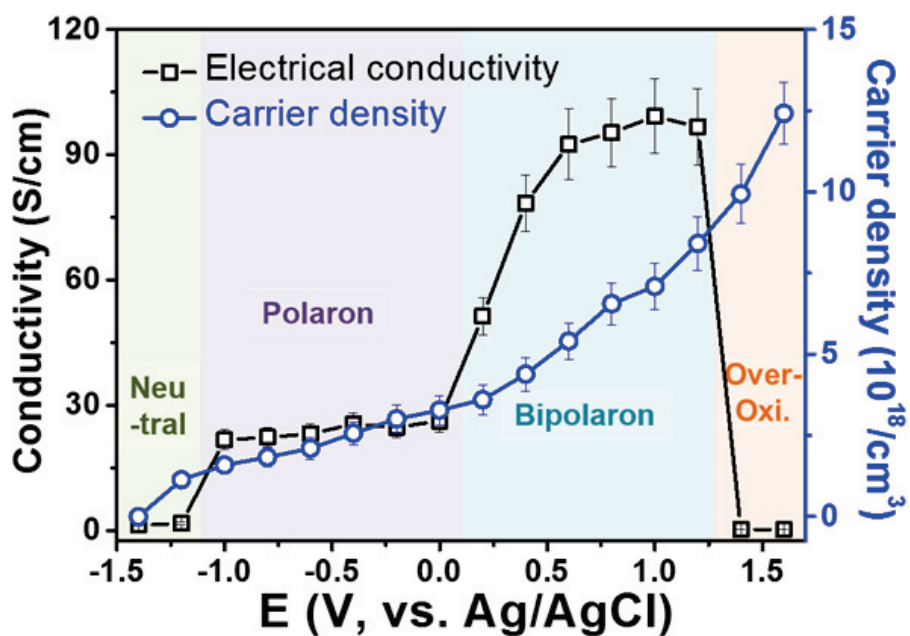
Figure 23. Electrical conductivity (black open square), carrier density (blue open circle) of the three-dimensional microvillus-like conductive nanofilms with applied voltage variation.
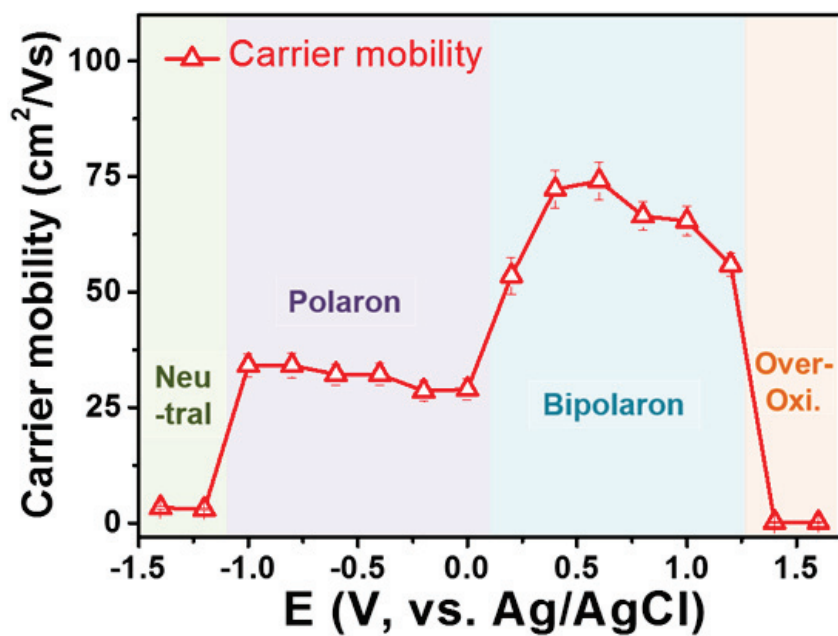
Figure 24. Carrier mobility of the three-dimensional microvillus-like conductive nanofilms with applied voltage variation.
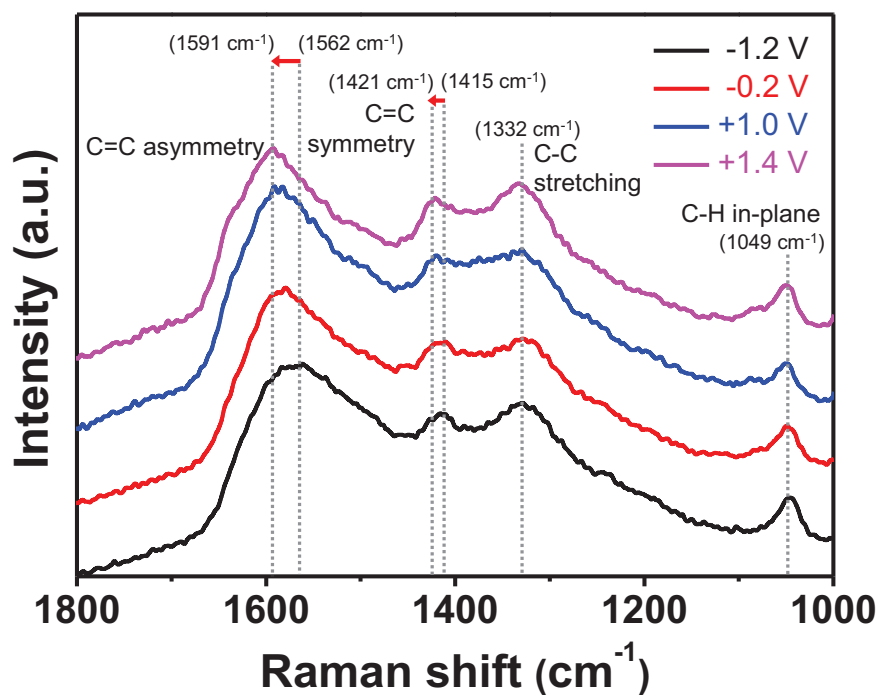
Figure 25. Raman spectra of the three-dimensional microvillus-like conductive nanofilms with different oxidation levels (black: -1.2 V, red: -0.2 V, blue: +1.0 V, pink: +1.4 V).
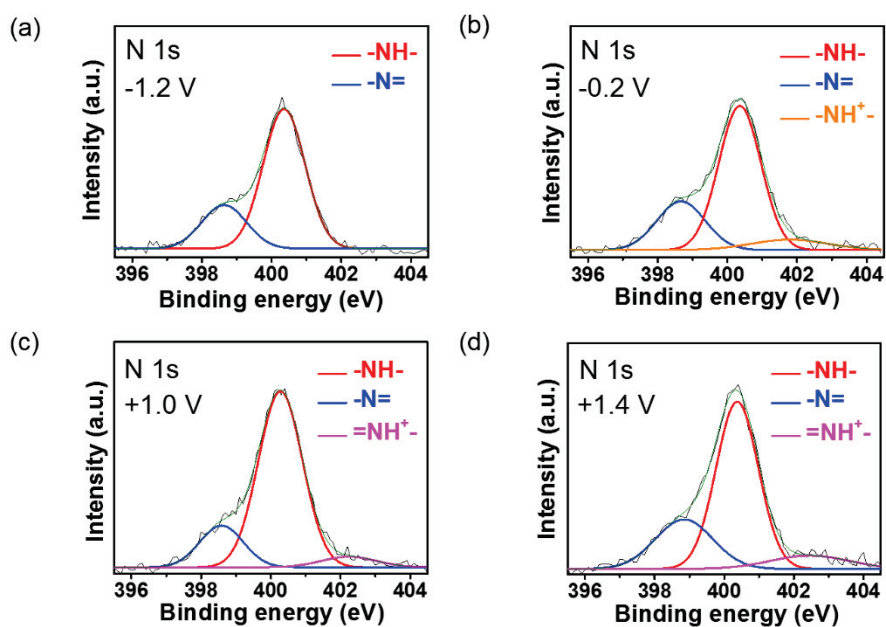
Figure 26. N 1s X-ray photoelectron spectra (XPS) of the three-dimensional microvillus-like conductive nanofilms with different oxidation levels: (a) -1.2 V; (b) -0.2V; (c) +1.0 V; (d) +1.4 V.
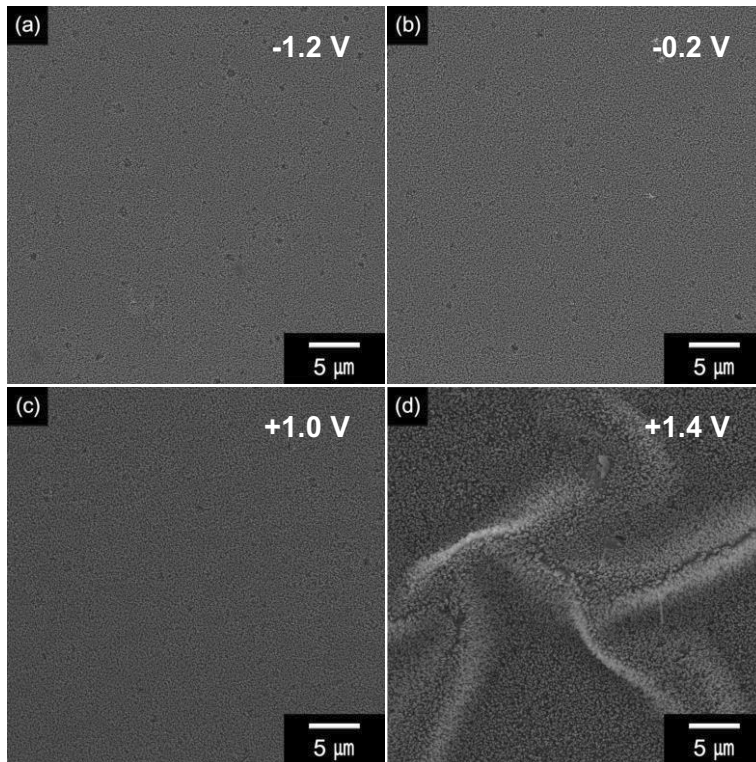
Figure 27. Low-magnification FE-SEM images of the three-dimensional microvillus-like conductive nanofilms as a function of applied voltage variation: (a) -1.2 V; (b) -0.2 V; (c) +1.0 V; (d) +1.4 V.
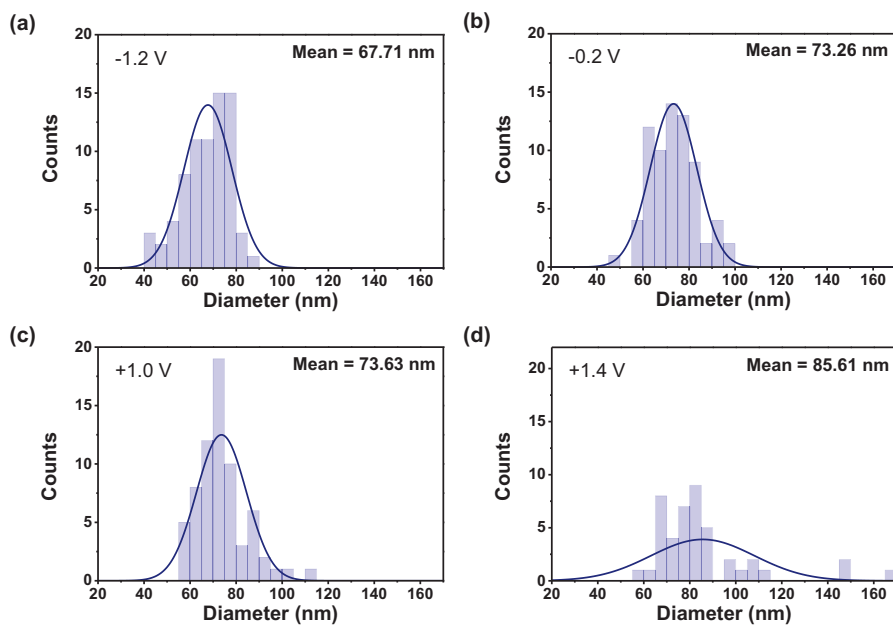
Figure 28. Diameter distribution of the polypyrrole nanorods in the conductive nanofilms with different oxidation levels: (a) -1.2 V; (b) -0.2 V; (c) +1.0 V; (d) +1.4 V.
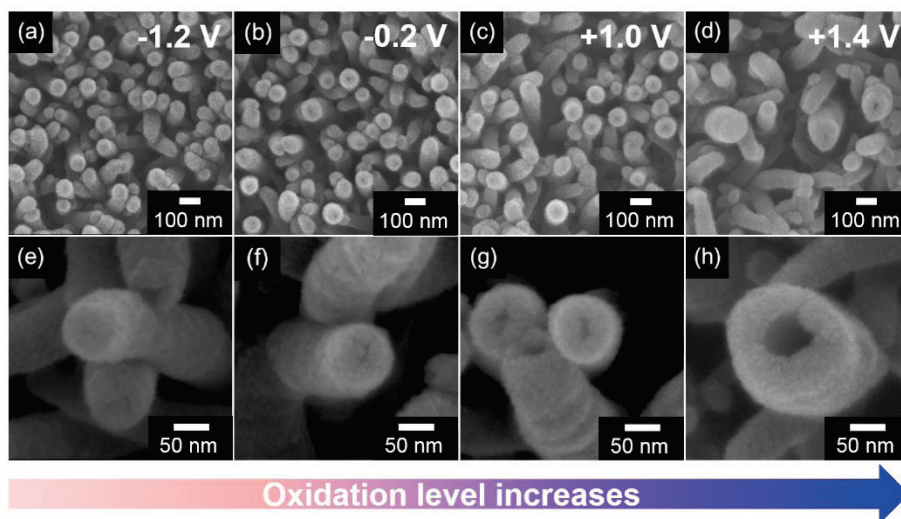
Figure 29. Low- and high-magnification FE-SEM images of the three-dimensional microvillus-like conductive nanofilms with different oxidation levels: (a),(e) -1.2 V; (b),(f) -0.2 V; (c),(g) +1.0 V; (d),(h) +1.4 V.

3.1.3. Application for VOC gas sensor

To investigate the sensing performance of the conductive nanofilms as a sensor transducer, a silver paste was printed on to the both ends to fabricate electrodes for resistive gas sensing. Before sensing of the volatile gases, current of the electrodes with voltage sweep from -1.0 V to +1.0 V to confirm whether the active area and the Ag pattern are well connected at each side. **Figure 30** shows the linearity current-voltage curves that verify electrical Ohmic contact rather than Schottky barriers with poor contact at the electrode.

The real-time responsive resistance changes are measured for different concentration of volatile gases at room temperature. Upon each exposure of gases, the conductive nanofilm-based electrodes present a rapid change in resistance over a several second-period before reaching a saturated value. **Figure 31** suggests the response as a different NH_3 concentration of the conductive nanofilms with temperature variation. The amount of response is decreased at higher reaction temperature owing to diminishing active surface area that comes from larger nanowire and thicker aggregated part in the film structure. Therefore, the sensing performance of the sensor electrodes as a function of oxidation level is conducted using the nanofilms

polymerized at 5ºC.

Figure 32 shows the sensing performance of the NH_3 gas that is one of reducing gases as a function of the oxidation level and suggests most sensitive (up to 1 ppb) in the +1.0 V of electrode due to high density of charge carrier (hole) and space formation of in the nanowire. On the other hand, applied potential at +1.4 V of electrode is applied over-oxidation causing destruction of conductive polymer chain and displays no response to the NH_3 gas. Therefore, better sensitive response is achieved with a large amount of charge carrier and active sites to the gas, as a result of the enhanced activity toward the NH_3 gas. The enlarged a number of charge carrier and active sites in the polymer nanostructure reduce response times to less than 20 s for the NH_3 gas (**Figure 33a**). Especially, the enhanced density of the charge carrier allowed rapid diffusion of the electrons for analyte. However, recovery times of the electrodes presents similar value because detach of the target molecule is concerned about applied external energy rather than charge carrier and active sites (**Figure 33b**). In addition, to confirm sensing ability for the materials that has opposite charge transfer direction, methanol molecule (i.e., oxidizing gas) is detected (**Figure 34**). Similar to the NH_3 case, the electrode for +1.0 V displays

superior to other electrodes as the same reason. **Figure 35** illustrates the normalized resistance changes of the electrodes as a function of NH_3 and MeOH gas concentrations. Linear behavior range of the electrode for +1.0 V (1 ppb – 10^2 ppm for NH_3 and 0.1 ppm – 10^3 ppm for MeOH) is larger than other electrodes. Therefore, the oxidized sensor electrode at +1.0 V can be effectively utilized as a signal transducer for detecting NH_3 and MeOH gases of various concentrations.

Outstanding flexibility and cycle stability is required for electrode materials in the practical wearable sensor devices. **Figure 36** represents the resistance change of the oxidized electrode at +1.0 V against periodic exposure to 1 ppb NH_3 gas. During the 5 repetitive on-off tests, the resistance change is maintained at a similar value without retardation of the response or recovery times that is the PPy film has reversible detection ability and stability up to MDL. In addition, flexibility of the substrate (PET and graphene) and the decorated conductive nanofilms enables consistent sensing performance even when the sensor is deformed in several ways. The resistance change of the sensor electrode shows a comparable amount with deformations such as different angles of concave and convex at 1

ppb of NH$_3$ gas (**Figure 37a**). There is also no significant effect during repeated bending deformation (up to 500 cycles) due to the uniformity of the each component (polymer nanofilm and Ag paste) on the substrate (**Figure 37b** and **Figure 38**).

The selectivity of the sensor electrodes is also one of the important issues to apply them into practical application. **Figure 39** suggests the normalized resistance changes of oxidized electrode at +1.0 V to various volatile gases at low concentrations (1 ppm for NH$_3$ and MeOH; 100 ppm for others). Even though lower concentration than others, NH$_3$ gas shows *ca.* 10 times larger signal change. Therefore, NH$_3$ can be classified from other chemicals based on the extent and direction of the resistance changes upon analyte exposures.
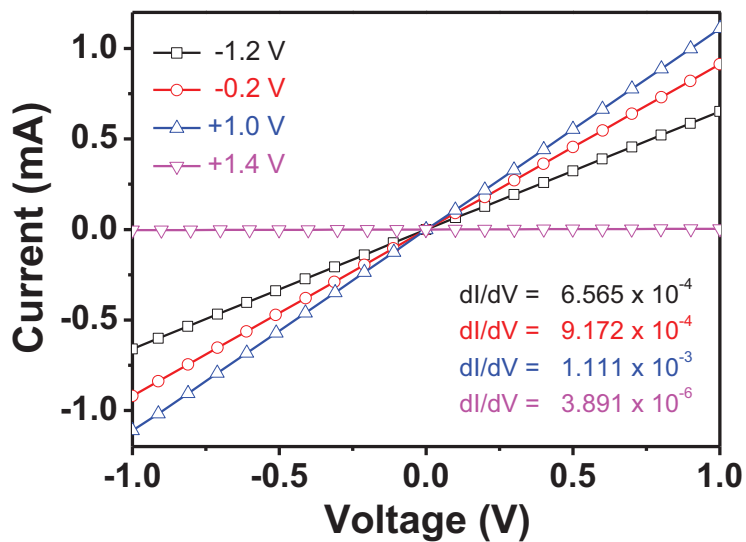
Figure 30. Current-voltage (*I-V*) curves of the three-dimensional microvillus-like conductive nanofilm-based sensor electrode with applied voltage variation (black: -1.2 V, red: -0.2 V, blue: +1.0 V, pink: +1.4 V).
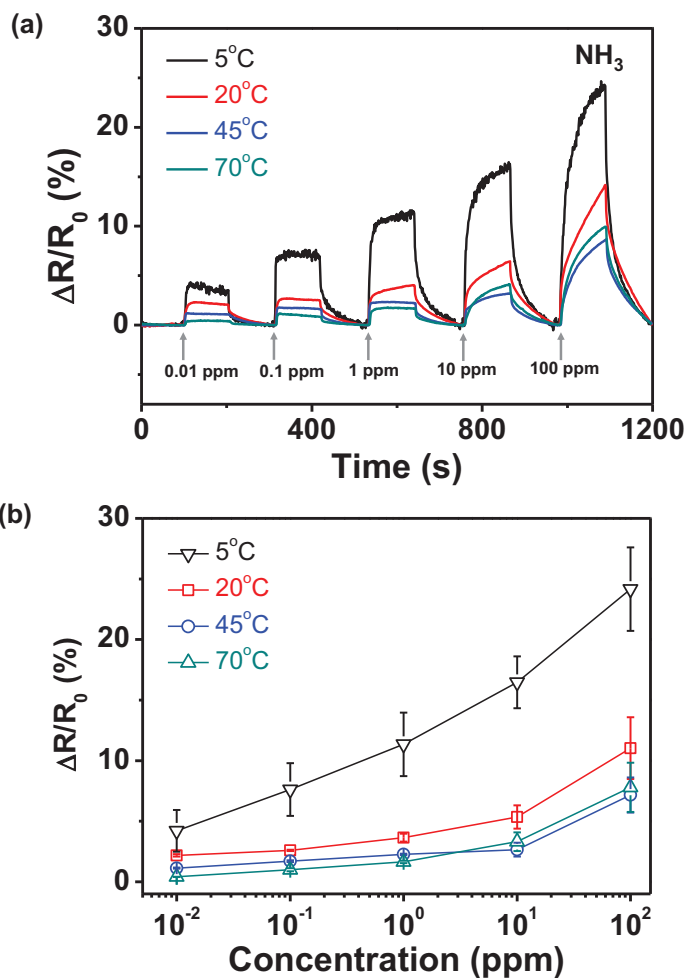
Figure 31. Normalized resistance changes of the conductive nanofilms with different polymerization temperatures (a) upon sequential exposure to NH_3 gas and (b) as a function of NH_3 concentration (black: 5°C; red: 20°C; blue: 45°C; pink: 70°C).
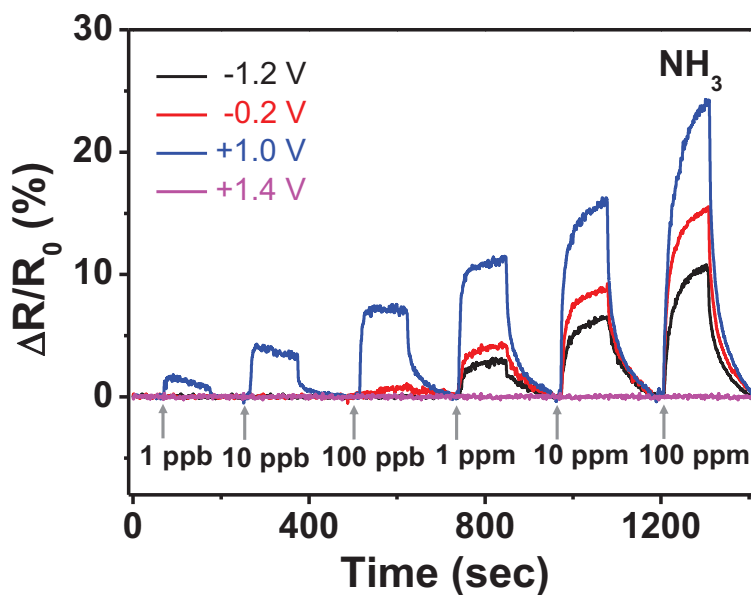
Figure 32. Reversible and reproducible responses are measured at a constant current value (10^{-6} A) of the three-dimensional microvillus-like conductive nanofilms with different oxidation levels. Normalized resistance changes upon sequential exposure to various concentration of NH_3.
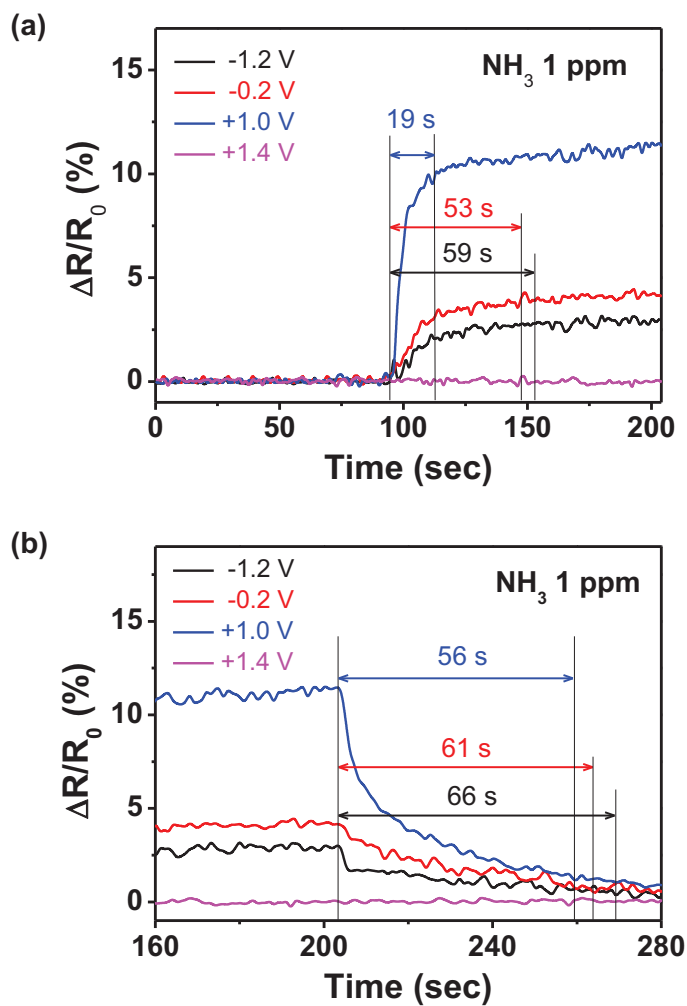
Figure 33. (a) Response and (b) recovery times of the conductive nanofilms toward 1 ppm of NH$_3$.
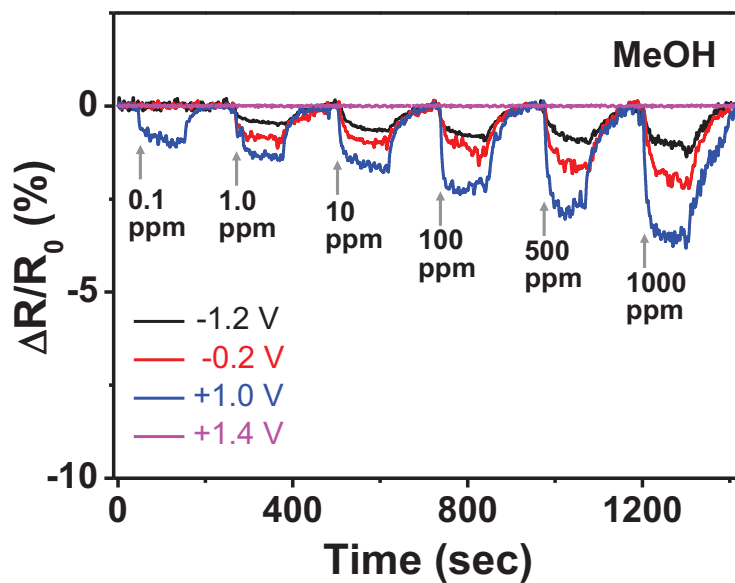
Figure 34. Normalized resistance changes of the three-dimensional microvillus-like conductive nanofilms with different oxidation levels. to different MeOH concentrations.
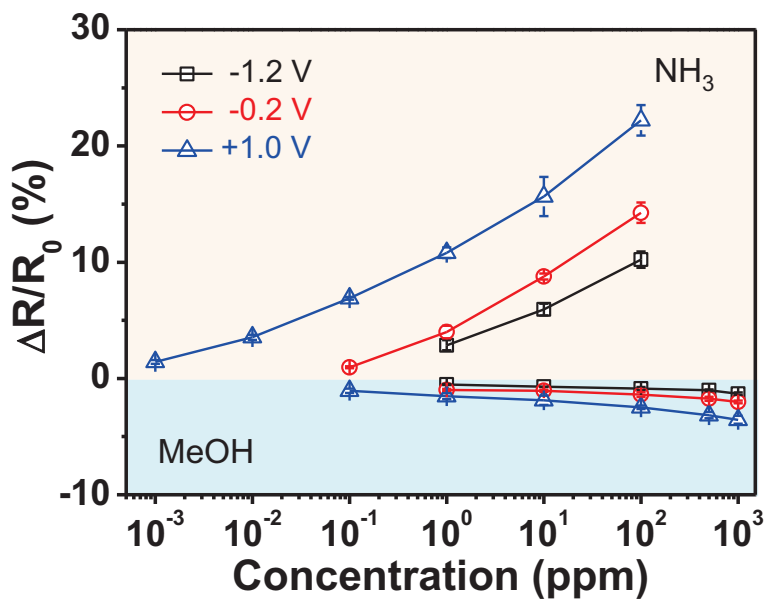
Figure 35. Calibration lines of the conductive nanofilms as a function of NH₃ and MeOH concentrations. Each applied voltages is as follows: black for -1.2 V; red for -0.2 V; blue for +1.0 V; pink for +1.4 V.
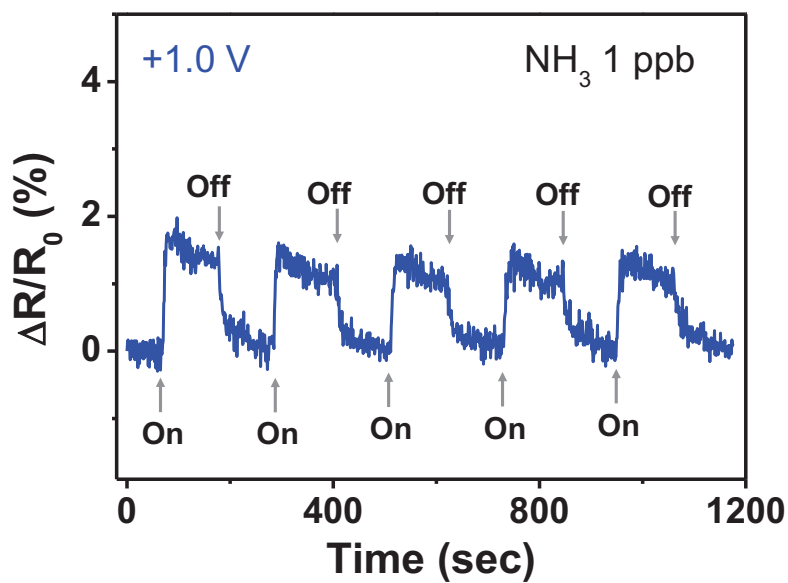
Figure 36. Periodic exposure of the +1.0 V applied conductive nanofilm to 1 ppb of NH₃ gas.

(a)

(b)
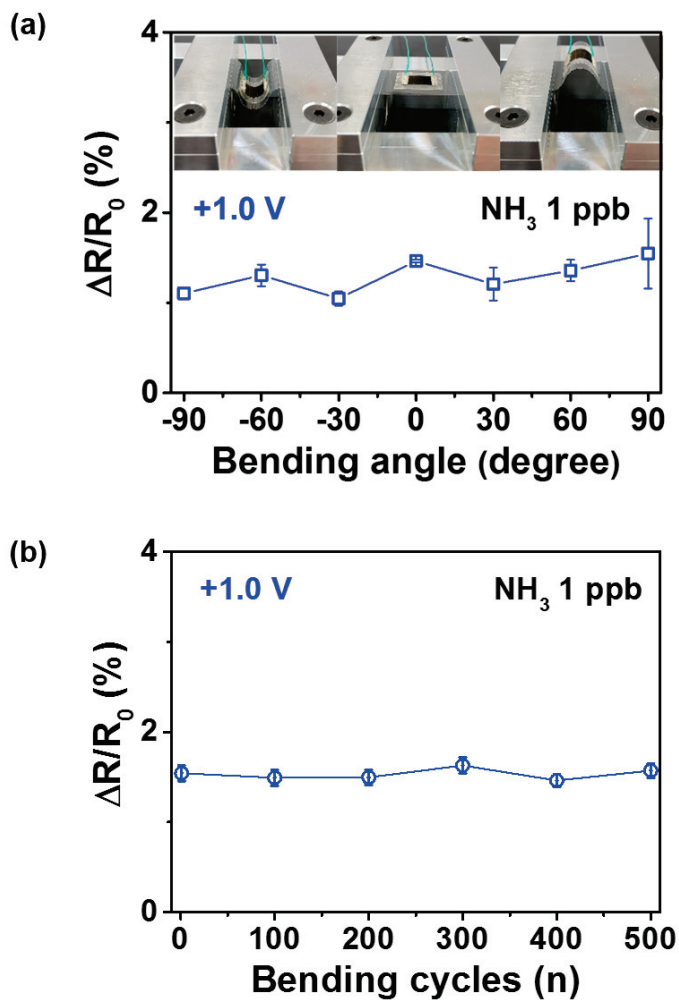
Figure 37. Normalized resistance changes of the +1.0 V applied conductive nanofilm under (a) various bending angles and (b) repeated bending cycles.
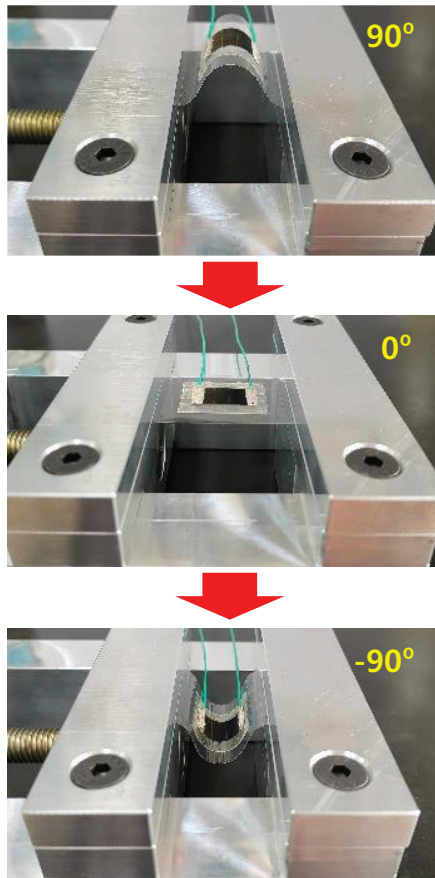
Figure 38. Photographs of the sensor electrode under different deformations for 1 cycle.
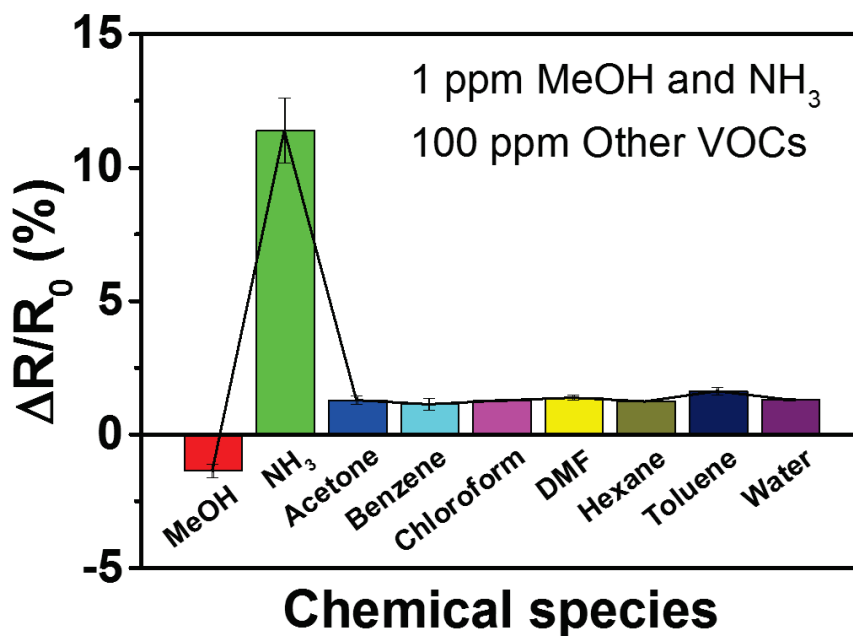
Figure 39. Sensing performance histogram of the +1.0 V applied conductive nanofilm to different oxidizing and reducing volatile gases. The concentration of gases as following: 1 ppm of NH_3, 1 ppm of MeOH, and 100 ppm of others.

3.2. **Fabrication** **of** **Pd** **NP-decorated** **three-dimensional** **polypyrrole nanowire-based conductive nanofilms for hydrogen gas sensor: Size control of Pd NP**

3.2.1. **Fabrication** **of** **Pd** **NP-decorated** **three-dimensional** **polypyrrole nanowire-based conductive nanofilms**

The PPyPds were prepared by direct electropolymerization of PPy nanowire structure on interdigitated array (IDA) electrode, followed by electrodeposition of Pd nanoparticles, as illustrated in **Figure 40**. First, thermal evaporation of metals (Cr/Au) and lift off processes were conducted to create micro-patterns on the glass substrate to make IDA electrodes. The IDA electrodes comprise of several small electrodes, separated by small gaps of 2 μm, thus electrically non-conducting. Using an IDA electrode as a working electrode of a 3-electrode cell, 3D structured conductive polypyrrole nanowires (PPy) can be electrochemically deposited on an individual electrode.

PPys have a 3D structure because nanowires grow in a vertical direction with respect to IDA electrode surface during the electropolymerization [106]. The repulsive force of the micelles produced by *p*-toluenesulfonate within an electrolyte promotes homogenous nucleation, which is responsible for vertically oriented

growth of nanowires [118]. Also, the low temperature of the reaction (5°C) provides the small-sized nuclei to achieve narrow diameter. During the electropolymerization process, PPy can bridge the adjacent small electrodes and therefore produces the conductive pathway, as the deposition of a thin film of polypyrrole onto a substrate is preceded by nanowire growth. The distance between small electrodes is short as if the sufficient amount of polypyrrole thin film is deposited, the boundary of one polypyrrole thin film and another can meet together to fill the gap [107]. To fabricate Pd nanoparticle (Pd NP) decorated PPy structure, this time the PPy functionalized IDA electrode was immersed in an acidic aqueous solution containing Pd precursor as a working electrode and the electrodeposition of Pd was carried out for 5 min at 0 V. The amount and population of Pd NPs were regulated by varying the precursor concentration of the electrolyte. For example, PPyPd_0.1 refers to Pd nanoparticle decorated PPy, where 0.1 mM of $PdCl_2$ solution was used for material fabrication.
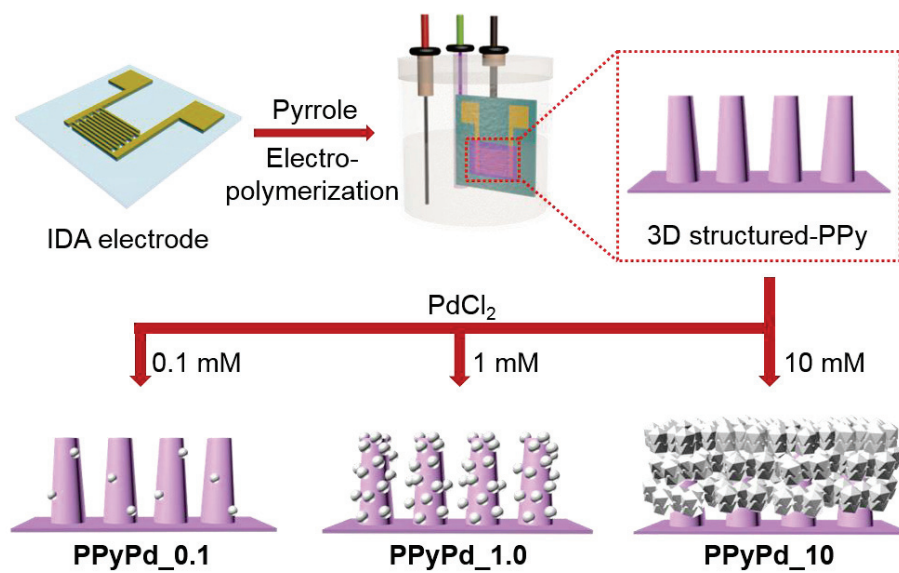
Figure 40. Schematic illustration for fabrication procedures of PPyPds.

3.2.2. Characterization

Field-emission scanning electron microscopy (FE-SEM) images in **Figure 41a-c** shows three types of PPyPds with population controlled Pd NPs through adjusting precursor concentration in the electrodeposition. The electropolymerized polypyrrole nanowires, which form the basis of the Pd growth, were *ca.* 500 nm long and 70 nm thick. The PPy provides highly open structure for Pd ion penetration and amorphous phase for randomly distributed anchoring sites for Pd NP nucleation [119,120]. In PPyPd_0.1, Pd NPs were barely observed (**Figure 41a**). It is not until the concentration of the Pd precursor is 1mM that the Pd NPs can be distinguishable (**Figure 41b**). In PPyPd_1.0, round shape Pd NPs are uniformly distributed around the PPy nanowires including nanowire tips and bodies. The average diameter of the Pd NPs was *ca.* 45 nm. At higher concentration of Pd (10 mM, **Figure 41c**), the Pd NP grew into a star or sea urchin shape rather than a round one. The urchin-shaped Pd NPs have an average width of *ca.* 230 nm, which is about five times larger than PPyPd_1.0. In order to get more details on the morphologies of PPyPds, the side views of PPyPds were confirmed by cross-sectional FE-SEM images. **Figure 42a** and **b** present images that are consistent with top views.

Particularly in PPyPd_10, it is clearly revealed that PPy nanowires were covered thick with chunks of Pd NPs (**Figure 42c**), which would be more suitable to considered as submicron agglomerates than nanoparticles.

To further characterize the Pd NP population controlled PPyPds, the energy dispersive X-ray spectroscopy (EDS) mapping and EDS spectra analyses were carried out (**Figure 42d-f**, **Figure 43, Table 1**). The EDS results revealed that there is a significant difference in Pd atomic percentage depending on the precursor concentrations. In addition, transmission electron microscope (TEM) images and X-ray diffraction (XRD) patterns of PPyPd were obtained to confirm the crystal structure of Pd NPs (**Figure 44**). The diffraction peak at $2\theta= 23.65°$ could be assigned to the amorphous phase of PPy [121]. The peaks at $2\theta= 40.55°$ and $47.26°$ correspond to (111) and (200) planes of fcc crystalline phase of Pd (JCPDS 05-0681), respectively [122,123]. Consequently, it was determined that the concentration of the precursor should be fixed at 1mM since PPyPd_1.0 has the appropriate shape and population of Pd NP.
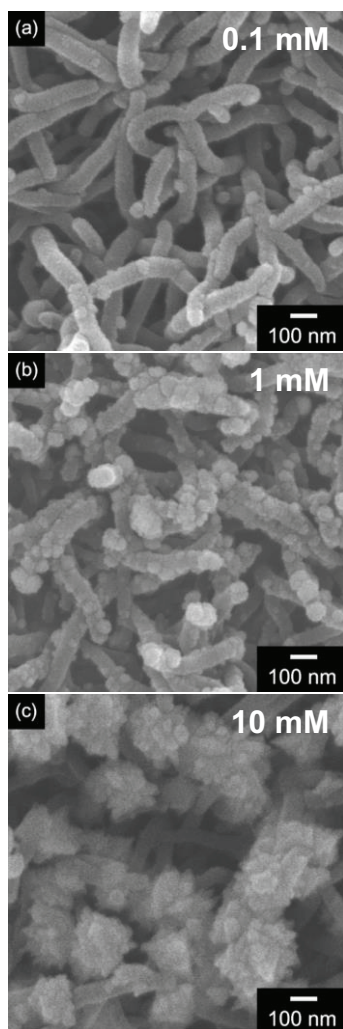
Figure 41. Field-emission scanning electron microscope (FE-SEM) of PPyPds with controlled population of Pd nanoparticles by changing precursor concentration. (a) 0.1 mM PdCl$_2$ (PPyPd_0.1), (b) 1 mM PdCl$_2$ (PPyPd_1.0) (c) 10 mM PdCl$_2$ (PPyPd_10).
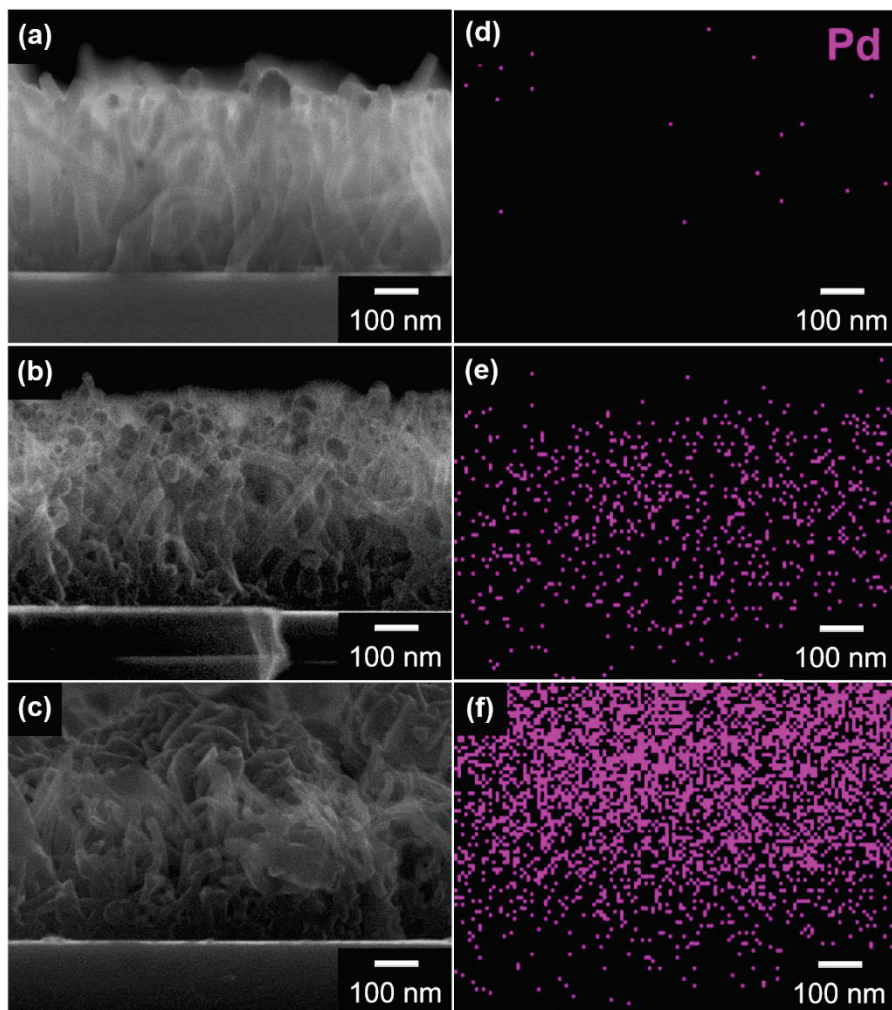
Figure 42. Cross-sectional FE-SEM microscopes of (a) PPyPd_0.1, (b) PPyPd_1.0, and (c) PPyPd_10 and EDS mapping images of Pd atom: (d) PPyPd_0.1, (e) PPyPd_1.0 (f) PPyPd_10.

(a)

PPyPd_0.1

Full Scale 836 cts Cursor: 0.000   keV

(b)

PPyPd_1.0

Full Scale 1347 cts Cursor: 14.169 (0 cts)   keV

(c)

PPyPd_10

Full Scale 1129 cts Cursor: 0.000   keV
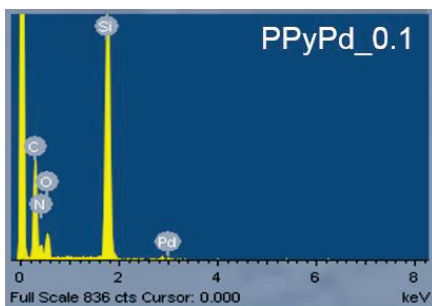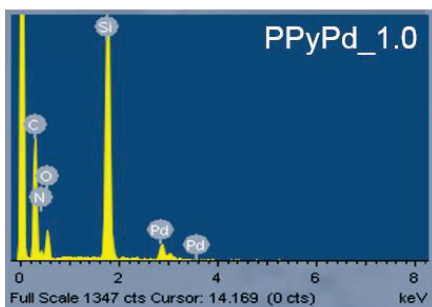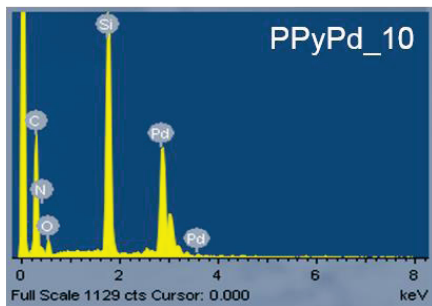
Figure 43. EDS spectra of PPyPds with Pd nanoparticles of controlled density by variation in precursor concentration. (a) PPyPd_0.1, (b) PPyPd_1.0, and (c) PPy_Pd_10.

110

Table 1. Elemental analysis of PPyPd_0.1, PPyPd_1.0, and PPyPd_10

Samples	Atomic%				
	C	N	O	Pd	Total
PPyPd_0.1	33.64	38.77	27.35	0.24	100
PPyPd_1.0	36.40	35.02	26.36	2.22	100
PPyPd_10	40.71	37.12	6.05	16.12	100

Atomic percentages of the samples were obtained by FE-SEM (JSM-6701F, JEOL) installed with Energy Dispersive X-ray spectrometer (INCA Energy, Oxford Instruments Analytical Ltd.).
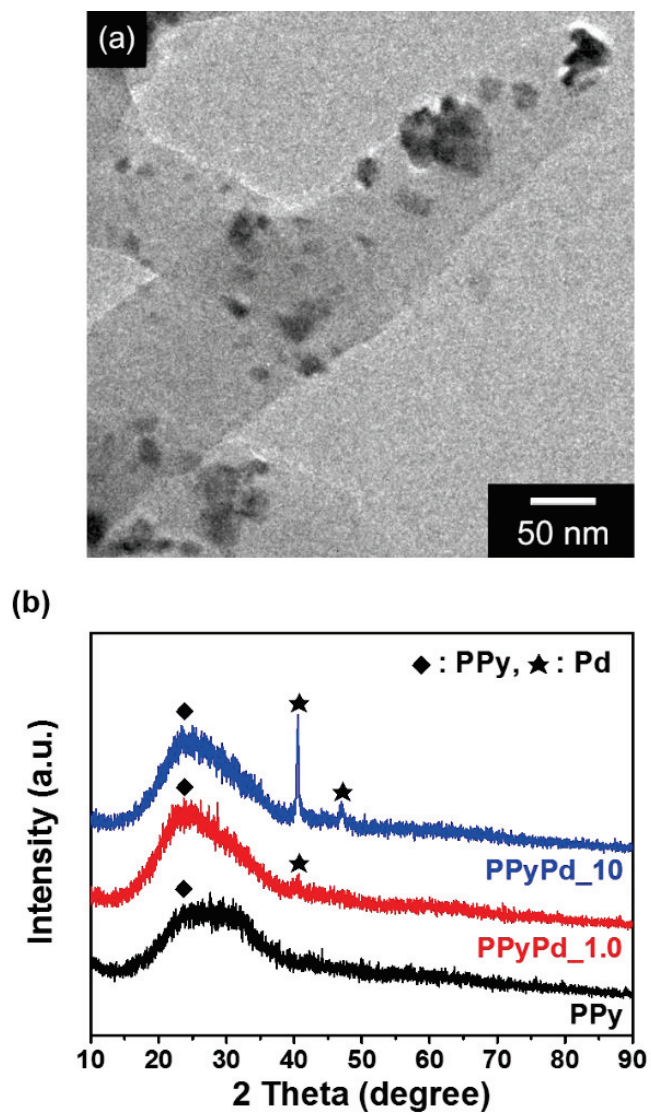
Figure 44. (a) Transmission electron microscope (TEM) image of PPyPd_1.0 and (b) X-ray diffraction (XRD) patterns of PPyPd_10, PPyPd_1.0, and PPy.

3.2.3. Size control of Pd NPs in Pd NP-decorated three-dimensional polypyrrole nanowire-based conductive nanofilms

After fixing the concentration of the precursor to 1 mM, the reaction temperature during the electrodeposition of Pd was adjusted to change the size of the Pd NPs. The degrees of 5, 60, and 90°C were chosen as temperature variables, and the ice bath and hot water bath were used to drop or elevate the temperature. **Figure 45** schematically illustrates the growth mechanism of Pd NP with increasing temperature [124]. The particle size increases as the temperature of the medium increases. After the nucleation process where the Pd ions are reduced at the surface of PPy nanowire, the Pd seed are attached. Then, the reduction occurs continuously around the existing seeds and Pd NP grows in a radial direction. It can be explained by the fact that when the temperature increases, the diffusion length of Pd ion increases which in turn makes the ions to easily incorporate into an existing large cluster contributing to growth. Thus, a large particle acts as a sink for small particles [125]. This phenomenon is similar to mass transport in Ostwald ripening. According to Ostwald ripening, the larger particles grow or ripen at the expense of the smaller ones due to their desire to minimize the surface free energy of the particle. The aggregative-

coalescence process is also involved in the electrochemically facilitated the surface diffusion process [126,127].

FE-SEM images and distribution histograms investigated the size variation of Pd NPs at different electrodeposition temperature (**Figure 46**). At low temperature (5°C), the growth of Pd NPs was mainly focused on the end of PPy nanowires (**Figure 46a**). It is well known that the nucleation takes place preferentially at the disorder or grain boundaries of the substrate [128]. The nanowires build up from the bottom (substrate) to the air so that the tips of the nanowire is most freshly prepared and chemically active [106,114]. As the temperature increased from low to high, there was no significant difference in the number of Pd NPs, but the average size of the Pd NP embedded in PPy nanowire showed a notable change from 33.6 to 60.9 nm. To compare the distribution curve of **Figure 47a-c**, it is observed that the Pd NPs grown at a higher temperature has a much wider distribution than the Pd NPs at a lower temperature.

From the previous experiments of adjusting variables in reaction conditions, it was once again confirmed that the concentration of the precursor determines the population and shape of the Pd NP and that the reaction temperature regulates the size.
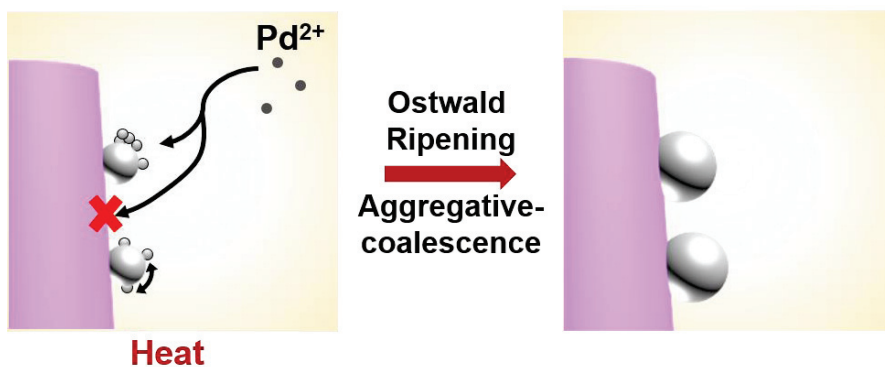
Figure 45. Growth mechanism of Pd nanoparticle with increasing electrodeposition temperature. Pd ions are reduced at the vicinity of existing nanoparticles whereas new nucleation at PPy surface is hindered. Small Pd clusters deposited on Pd NP surface aggregate and coalesce to cover the entire surface.
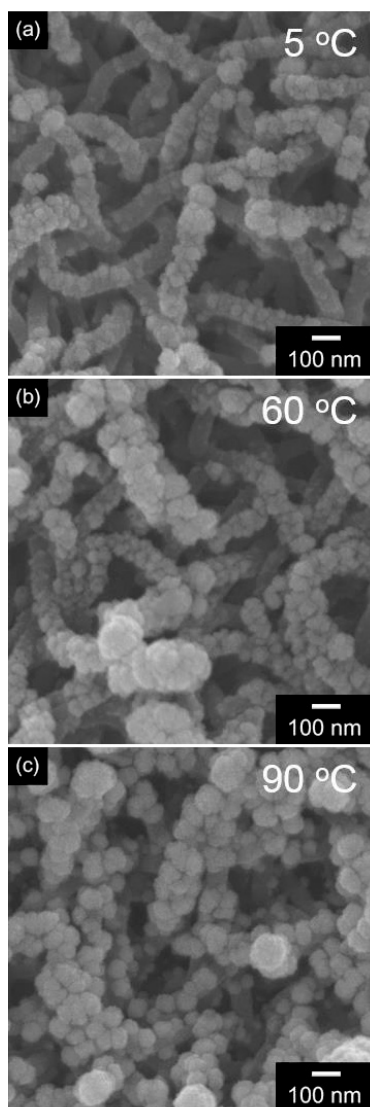
Figure 46 FE-SEM images of PPyPds obtained at different electrodeposition temperatures: (a) 5ºC (PPyPd_1.0_5); (b) 60ºC (PPyPd_1.0_60); (c) 90ºC (PPyPd_1.0_90).
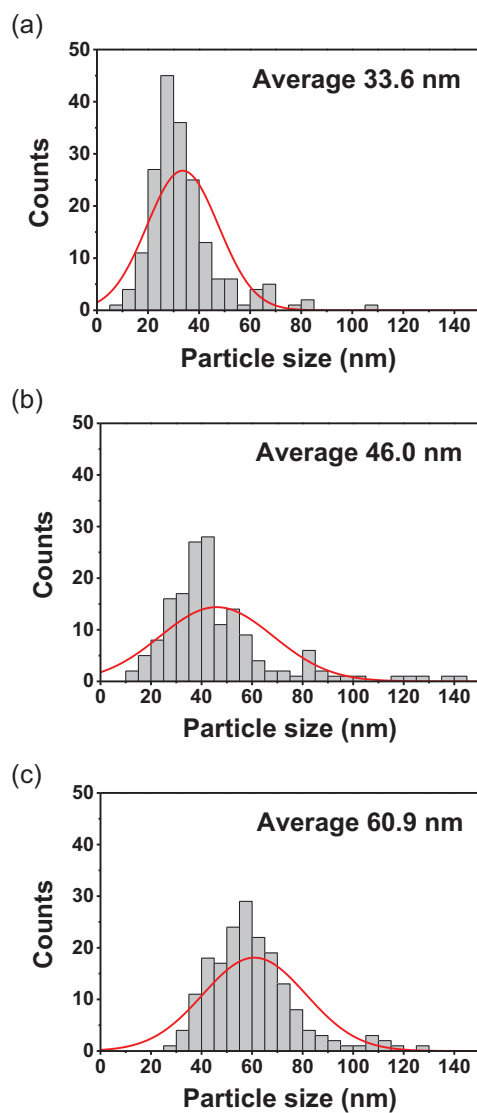
Figure 47. Histograms of Pd nanoparticle size distribution for (a) PPyPd_1.0_5 (5ºC), (b) PPyPd_1.0_60 (60ºC), and (c) PPyPd_1.0_90 (90ºC)

3.2.4. Application for hydrogen gas sensor

To characterize the electrical properties of the different PPyPd materials as a sensor electrode, current-voltage (*I-V*) measurement was conducted (**Figure 48**). Since the IDA electrodes were employed as a base substrate during the manufacturing of the transducer materials, the resulting PPyPd can be readily used as sensor electrodes without additional material deposition processes such as spin coating or drop casting. The *I-V* curves displayed linear modulations for the voltage range from -1 V to +1 V, indicating that the electrodeposited PPyPd has an Ohmic contact with the IDA electrode. The contact resistance (1/(*dI/dV*), reciprocal of the slope) value decreased with an increase in the particle size of the embedded Pd NP on the PPy nanowire surface, implying that the metallic property of Pd NPs contributed in decreasing the resistivity of the PPyPd materials.

Figure 49a and **b** schematically depicts the sensing mechanism of the PPyPd at room temperature. The hydrogen sensing is a catalytic chemical reaction between hydrogen gas and palladium. There are roughly two opposing types of sensing mechanisms in palladium-based hydrogen sensors: resistance increase or resistance decrease [129]. For the former, resistance increases with the transformation of Pd into

118

PdHx [130,131]. For the latter, the resistance decreases due to hydrogen-induced lattice expansion (HILE) in Pd [132]. In PPyPd hydrogen sensor, the electrode becomes more conductive upon H_2 ambient condition. As previously shown in FE-SEM images in **Figure 46**, Pd NPs are discretely embedded on PPy surface. This condition can be considered as a discontinuous film of island-like Pd at the percolation threshold [133]. At exposure to H_2 gas, hydrogen is dissolved in the Pd, causing lattice expansion, and results in interconnection of Pd grains. The dissolution of hydrogen in Pd also has an influence on interface between Pd and PPy [134]. It lowers the electronic work function of Pd thereby prevents leakage of charge carriers from PPy to Pd NP (**Figure 49c** and **d**) [135].

An X-ray photoelectron spectroscopy (XPS) analysis was conducted to elucidate the chemical composition change of the Pd before and after hydrogen gas exposure (**Figure 50**). In **Figure 50a**, the samples before H_2 and after H_2 displayed similar XPS patterns in a wide scan. However, noticeable change in peak intensity and shifts were observed in deconvoluted curves of Pd 3d core level (**Figure 50b**). The Pd 3d core level is composed of two main peaks of Pd $3d_{3/2}$ and Pd $3d_{5/2}$ peaks. Taking into account that the binding energy of 335.6 eV and

340.9 eV refer to the large neutral Pd (Pd^0) at (pink colored area), Pd remains mostly in the metallic state under air environment before being exposed to hydrogen gas [136]. After PPyPd was exposed to 100 ppm of H_2 gas, the intensity of Pd^0 peaks decreased and Pd^{2+} peaks (PdO, 336.4 and 341.6 eV) increased [137]. In addition, shifts from 338.8 to 339 eV and from 338.1 to 337.6 eV were observed. These peaks could belong to the strongly oxidized palladium oxide, PdOx (x>1) [138]. Thus, the strongly oxidized palladium oxide PdO_2 is unstable in its anhydrous phase [139].

The real-time monitoring of the resistance change of the sensor was performed with different concentrations of H_2 gas at room temperature. The range of H_2 concentration was varied from 5 ppm ($\fallingdotseq 0.0005\%$) to 2000 ppm ($\fallingdotseq 0.2\%$), which is much lower than the US Department of Energy's guidelines for the low flammable limit of 4% in air [140]. To evaluate the effect of palladium size on hydrogen sensing, sensing performances of three electrodes with different synthesize temperature (5ºC, 60ºC, and 90ºC) are conducted (PPyPd_1.0_5, PPyPd_1.0_60, PPyPd_1.0_90). Upon sequential exposure to H_2 gas, all PPyPd sensor exhibited rapid resistance decreases. The general sensing mechanism that governs the resistance decrease is explained in the previous section.

As sensing curves shown in **Figure 51**, the response and recovery time, response intensity, and the range of detectable concentration of H_2 gas varies with respect to the size of the palladium nanostructures. The response intensity was largest in PPyPd_1.0_90 (90ºC) and lowest in PPyPd_1.0_5 (5ºC) electrode. Also, the minimum detectable level (MDL) of the PPyPds have shown the clear difference as follows: PPyPd_1.0_5: 50 ppm; PPyPd_1.0_60: 10 ppm; PPyPd_1.0_90: 5 ppm. Hence, a more sensitive response was achieved with a bigger size of Pd nanoparticles. This is likely because bigger Pd NPs provide more active sites for hydrogen catalytic reaction. Moreover, the bigger Pd NP results in bigger size expansions, hence greater decrease in inter-nanoparticle gap [141]. Therefore, the change in resistance is much greater. For the control experiment held with the PPy electrode without Pd NPs, there was no resistance change at all (**Figure 52**). It was verified that the response to hydrogen is solely comes from Pd-H_2 interaction. In addition, PPyPd_1.0_90 shows low MDL and wide detection range of hydrogen gas when compared to previously reported hydrogen sensors (**Table 2**) [142-144].

Figure 53 presents calibration curves for the sensitivity as a function of H_2 gas concentration. The normalized electrical response was

proportional to the square root of H_2 concentration owing to the fact that hydrogen atoms dissociate from H_2 molecules to be adsorbed and dissolved into Pd lattice. The equations for the calibration curve calculated from the linear fitting of sensitivity changes are as follows:

$$y = -0.0215x \text{ (PPyPd\_1.0\_5)}$$

$$y = -0.0843x \text{ (PPyPd\_1.0\_60)}$$

$$y = -0.1234x \text{ (PPyPd\_1.0\_90)}$$

y: sensitivity

x: square root of H_2 concentration in ppm

Additionally, cyclic stability evaluation is executed to confirm features for the reliable chemical sensor. **Figure 54a** demonstrates the electrical response of PPyPd_1.0_90 sensor electrode upon periodic exposure to 5 ppm of hydrogen gas at room temperature. The PPyPd_1.0_90-based sensor yielded similar responses for MDL level of H_2 gas over five times of cyclic testing. Cyclic stability evaluation was executed with other electrodes (**Figure 54b**). When hydrogen gas with a concentration of 50 ppm was turned on and off continuously, all three electrodes of PPyPd_1.0_5, PPyPd_1.0_60, and PPyPd_90 showed good repeatability.

Figure 55 shows the gas sensing capability test according to the

concentration of the Pd precursors (0.1 and 10 mM) other than the optimum of 1mM. The sensor electrodes based on PPyPd_0.1 and PPyPd_10 exhibited completely different sensing behavior. When exposed to hydrogen gas, the resistance of PPyPd_10 increased whereas that of the PPyPd_0.1 decreased. The resistance decrease in PPyPd_0.1 showed no correlation with hydrogen concentrations; the absolute value of ΔR did not enhance even at high ppm of H_2 gas. Interestingly, the PPyPd_10 exhibited resistance increase as the concentration of H_2 increases, unlike PPyPd_1.0 and PPyPd_0.1. This is probably due to the fact that the electrical properties of the sensor are dominated by the PdHx phase transition because the bulk Pd is formed which entirely cover PPy structure.
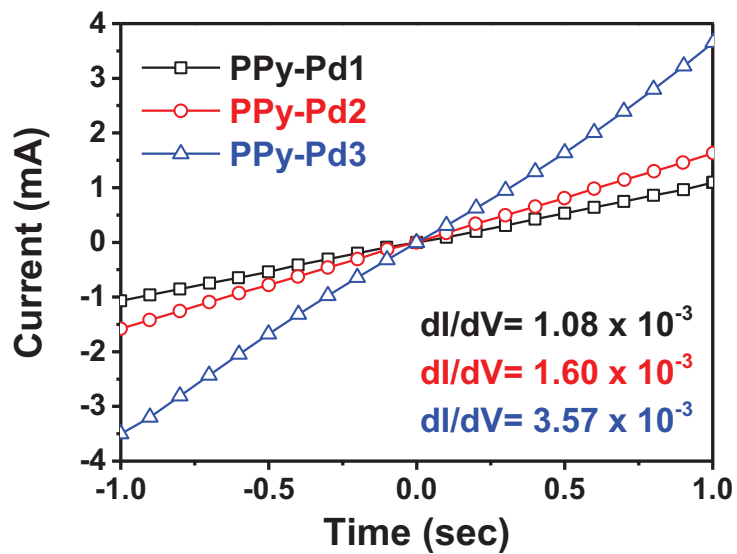
Figure 48. Current-voltage (*I-V*) curves of PPyPd_1.0_5, PPyPd_1.0_60, and PPyPd_1.0_90 electrodes (black: PPyPd_1.0_5; red: PPyPd_1.0_60; blue: PPyPd_1.0_90).
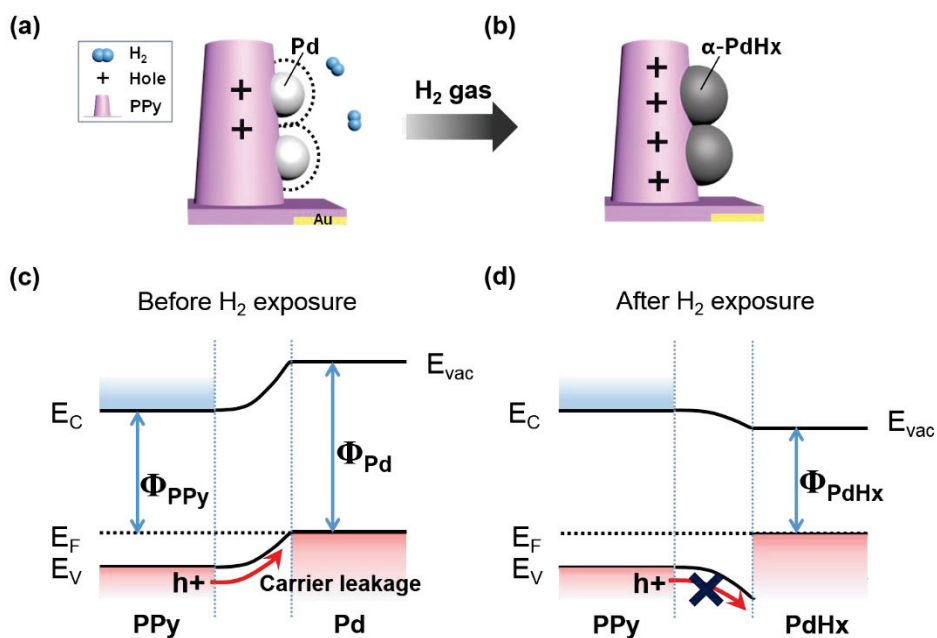
Figure 49. Plausible sensing mechanism of H_2 gas in PPyPd sensor electrode. (a),(b) schematic illustration representing phase transition of Pd into α-PdHx (x<0.017) and hole increase within PPy. (c),(d) Energy band diagrams of junction between PPy and Pd NP before and after H_2 exposure. E_C: conduction band; E_F: Fermi level; E_V: valence band; E_{vac}: vacuum level; Φ_{PPy}, Φ_{Pd}, and Φ_{PdHx}: work function of PPy, Pd, and PdHx, respectively.
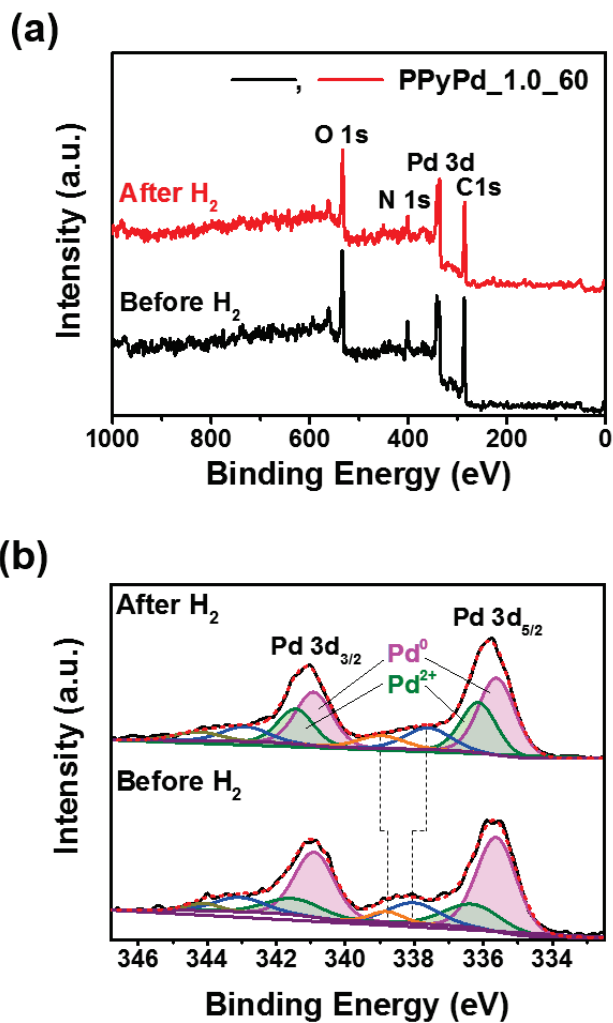
Figure 50. X-ray photoelectron spectroscopy (XPS) spectra of PPyPd_1.0_60 before and after exposure to 100 ppm of H_2 gas: (a) wide scan; (b) deconvoluted Pd 3d core level.
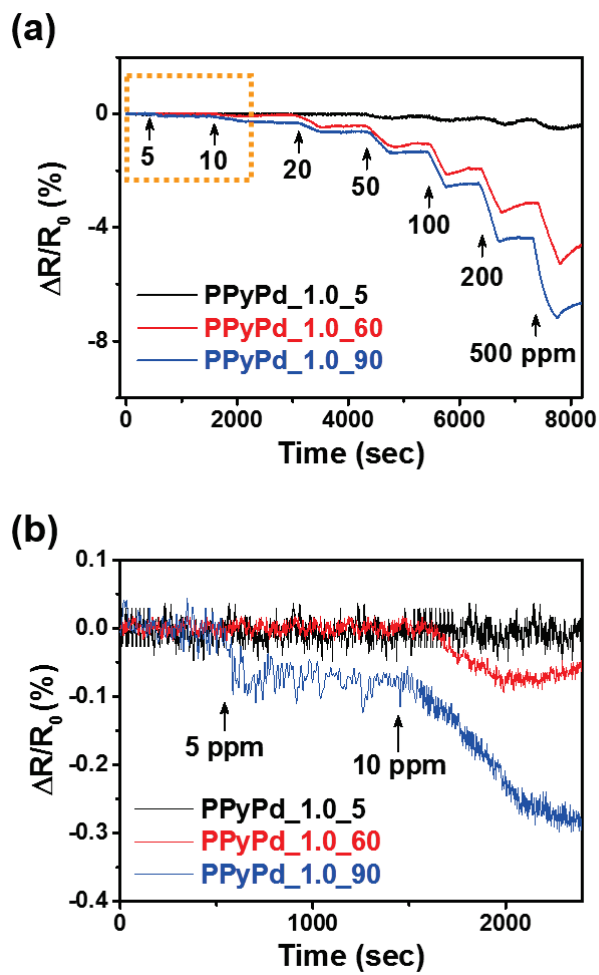
Figure 51. Normalized resistance changes (a) upon sequential exposure to various concentrations of H_2 gas at room temperature (black: PPyPd_1.0_5; red: PPyPd_1.0_60; blue: PPyPd_1.0_90). (b) Shows the minimum detectable level (MDL) data.
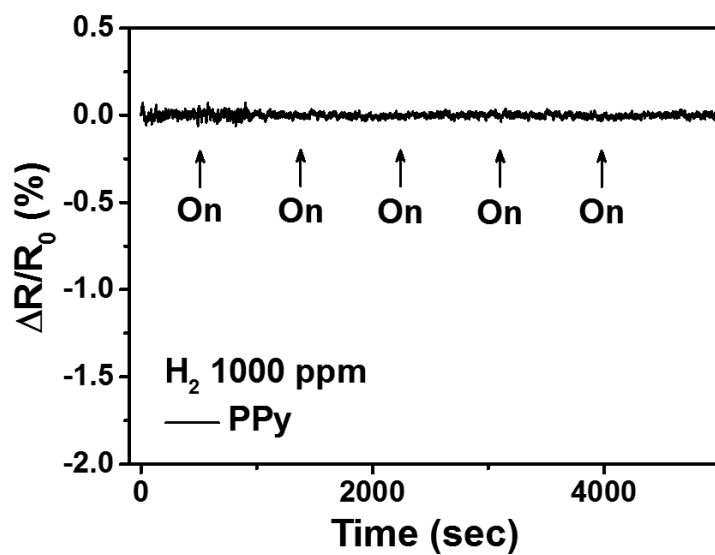
Figure 52. H_2 gas on-off tests for the performance evaluation of PPy electrode without Pd as a control experiment.

Table 2. Comparison of some recently reported Pd-based H_2 sensors.

Materials	Fabrication method[a]	MDL[b]	Dynamic range[c]	Working temp.[d]	Ref.
Pd NPs @ CPPyNP[e]	Chemical reduction	0.1 ppm	0.1-100 ppm	RT	[142]
Pd-PANI-rGO[f]	Chemical reduction	100 ppm	100-20000 ppm	RT	[143]
Pd NC@Gr[g]	Chemical reduction	6 ppm	10-500 ppm	RT	[144]
PPyPd_0.1_90	Electro-deposition	5 ppm	5-2000 ppm	RT	This work

[a]Fabrication method involved in transducer materials of the sensor electrode; [b]Abbreviation: MDL=minimum detectable level; [c]Dynamic range is the gas concentration measured in the paper; [d]Abbreviation: RT=room temperature; [e]Pd nanoparticles at carboxylated polypyrrole nanoparticles; [f]Pd-polyaniline-reduced graphene oxide composite; [g]Pd nanocube at graphene.
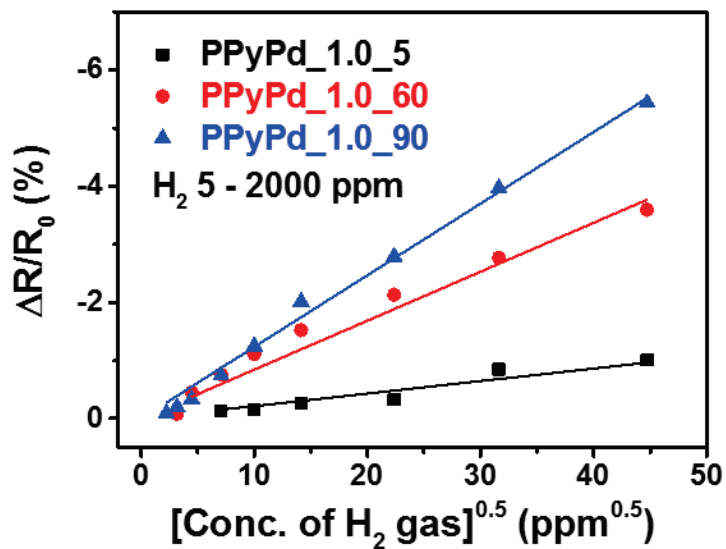
Figure 53. Calibration curves of various size Pd NPs-decorated PPyPds as a function of a square root of H_2 gas concentrations (black: PPyPd_1.0_5; red: PPyPd_1.0_60; blue: PPyPd_1.0_90).
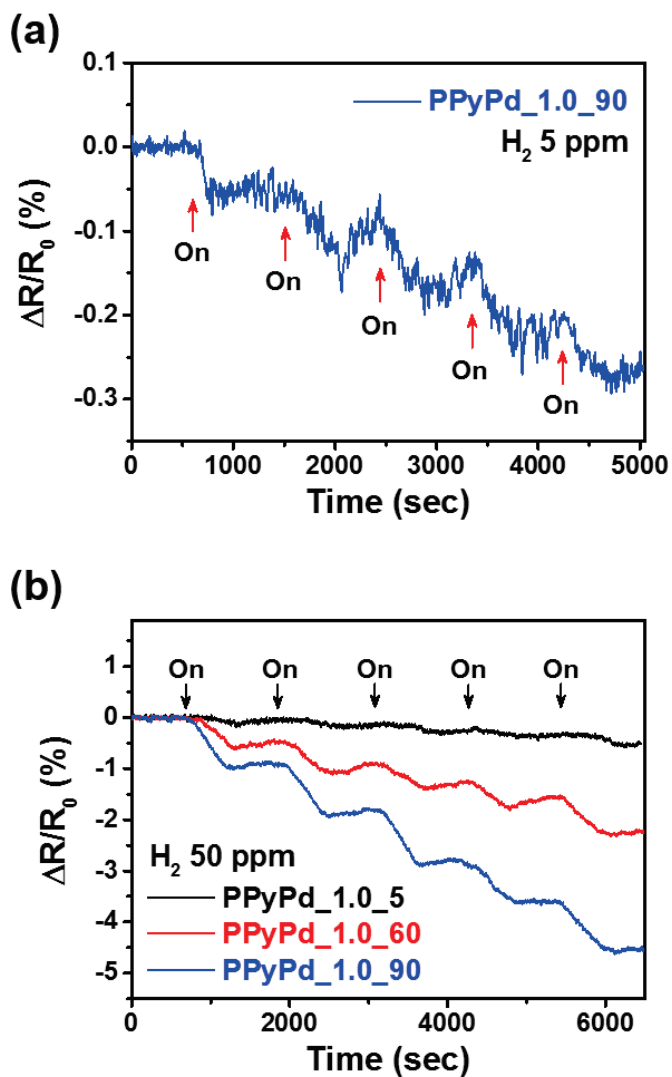
Figure 54. (a) H_2 gas sensing reliability of PPyPd_1.0_90 electrodes at MDL (5 ppm of H_2 gas). (b) Normalized resistance changes of different Pd NP size-controlled PPyPds upon periodic exposure to 50 ppm of H_2 gas.
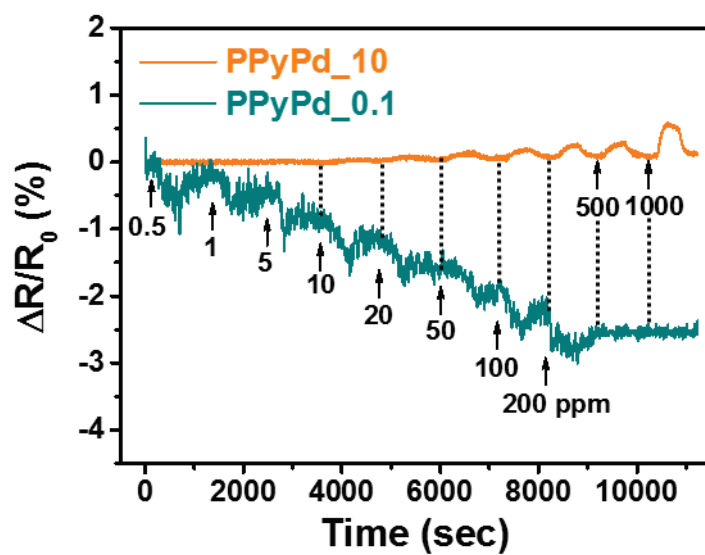
Figure 55. H_2 sensing performances of PPyPd electrodes with controlled Pd NP population by tuning $PdCl_2$ precursor concentrations (orange: PPyPd_0.1; cyan: PPyPd_10).

3.3. Fabrication of multidimensional polypyrrole nanowire-based conductive nanofilms for FET-type HBsAg aptasensor: Surface functionality control

3.3.1. Fabrication of multidimensional polypyrrole nanowire-based conductive nanofilms

Figure 56 suggests schematic illustration of multidimensional conductive nanofilm (MCNF) structure based on electropolymerization and acid treatment processes. First, monolayer graphene was synthesized by conventional chemical vapor deposition method and was transferred onto a transparent poly(ethylene naphthalate) (PEN) substrate to apply as a template of the multidimensional film (**Figure 57**). To fabricate MCNF, a vertically aligned polypyrrole nanowires were grown on the graphene surface using electro-polymerization of pyrrole at low temperature (5°C) with an mixed electrolyte solution (phosphate buffer and *p*-toluenesulfonate). In detail, phosphate buffer and *p*-toluene sulfonic acid (*p*TSA) were used, respectively, as an electrolyte and a dopant in the polymerization process. Especially, anions of *p*TSA act as a soft template to produce the vertically oriented polypyrrole nanostructure [114,145,146].

In the polymerization process, morphology of the polypyrrole nanostructures is changed by several variables such as electrolyte components and reaction times. Firstly, components in the electrolyte have critical effects in the formation of vertically aligned polypyrrole structures (**Figure 58**). The electrolyte solution without phosphate buffer component (i.e., electrolyte) in the solution generates randomly grown polypyrrole nanowires on the graphene surface. On the contrary, without pTSA (dopant) forms a slightly rugged polypyrrole layer rather than vertically aligned structure owing to absence of template. The other variable is an electro-polymerization reaction time that modifies polypyrrole nanostructure from short nanorod to nanofiber network. After 3 min of reaction, the polymer begins to nucleate and short nanorods are deposited on the graphene surface (**Figure 59a**). With increasing reaction time, the polypyrrole structure changes to elongated nanowires. After 25 min, vertically aligned polypyrrole nanowires *ca.* 1-μm long with diameter of *ca.* 70 nm (L/D = 15.5) are formed on the graphene surface (**Figure 59b**). Additionally, reaction time more than 25 min changes polypyrrole morphologies to aggregated network-like nanofibers. In particular, a value of the L/D ratio is 18.9 after 45 min of the electro-polymerization time (**Figure**

59c). Although the network-like nanofibers have a higher *L/D* ratio (18.9) than the nanowires (15.5), an amount of the biomolecule penetration for the network-like nanofibers is smaller than that of the nanowires owing to hindrance comes from an entangled structure. Therefore, proper polypyrrole structure in the electrolyte-gated aptasensor system is nanowire (for 25 min) rather than nanofiber network.
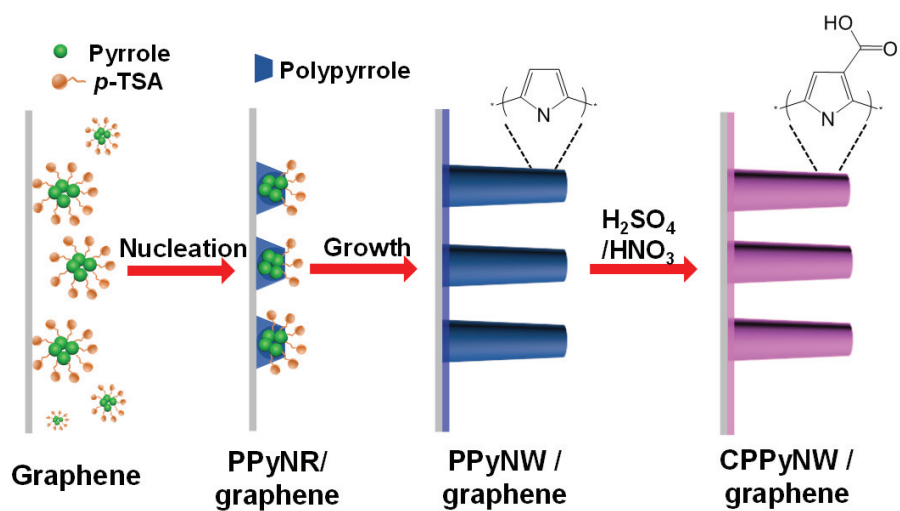
Figure 56. Schematic illustration of polypyrrole nanowire growth mechanism during electro-polymerization.
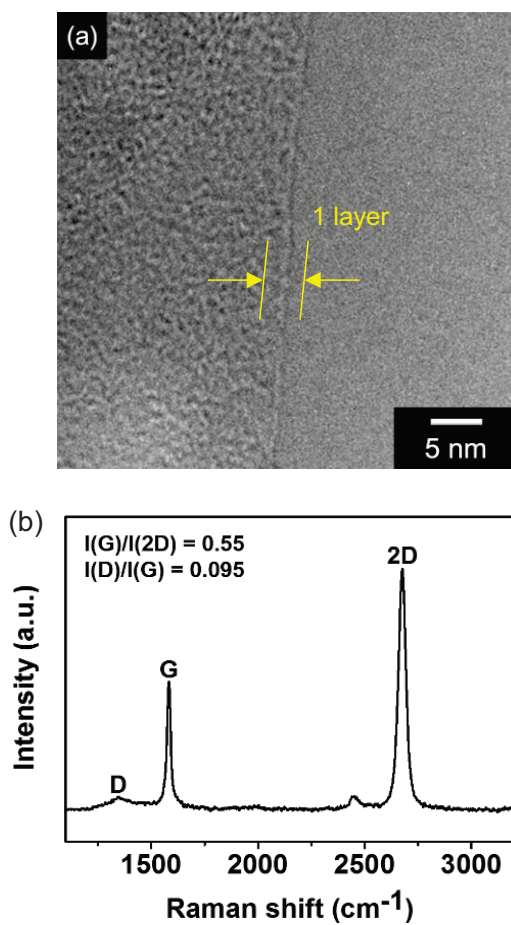
Figure 57. Characterization of CVD graphene. (a) High resolution transmission electron microscopy (HR-TEM) image and (b) RAMAN spectrum of the chemical vapor deposited graphene layer.
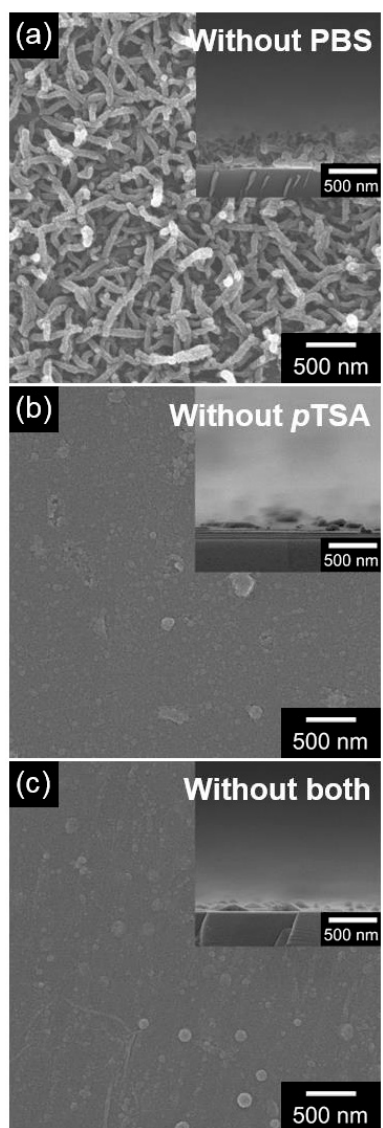
Figure 58. FE-SEM images of conductive nanofilms with different electrolyte compositions: (a) without phosphate, (b) without *p*TSA, and (c) neither phosphate nor *p*TSA.
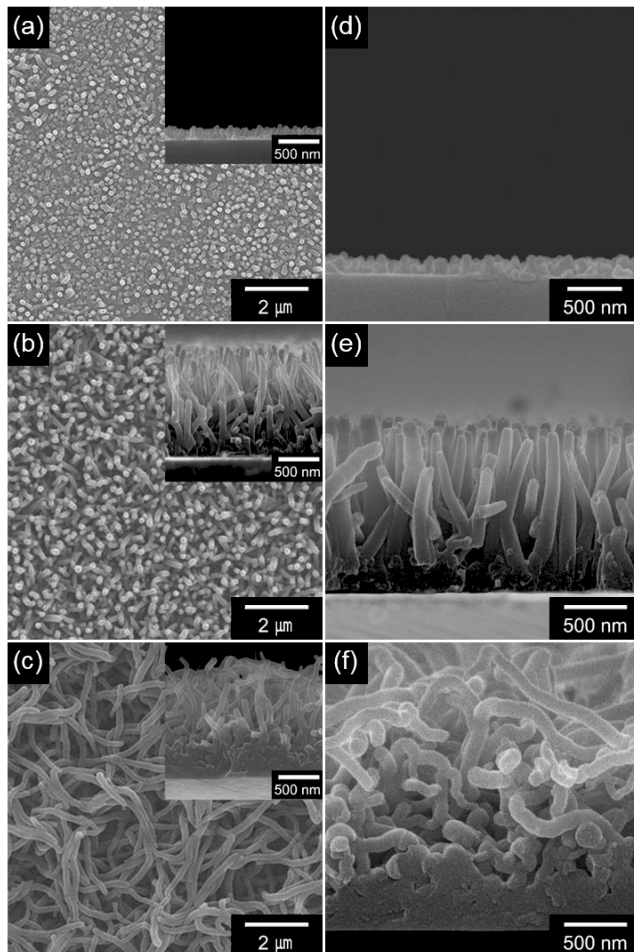
Figure 59. Planar and side-direction (inset) field-emission scanning electron microscopy (FE-SEM) images of the polypyrrole nanostructures: (a) nanorods, (b) vertically aligned nanowires, and (c) network-like nanofibers. FE-SEM images of acid treated polypyrrole nanostructures: (d) nanorods, (e) vertically aligned nanowires, and (f) network-like nanofibers.

3.3.2. Characterization

Then, polypyrrole was chemically functionalized with carboxyl groups using acid treatment process to immobilize bioreceptors on the nanowire surface, because strong bonding between receptor molecules and the transducer materials is critical issue on the fabrication of a highly sensitive and stable aptasensor. The morphology of the polypyrrole nanostructures is maintained after mild acid treatment process as shown in **Figure 59d-f**. Thus, carboxylic acid groups on the polypyrrole surface are generated without structure collapse after mild activation method.

In addition, to enhance the sensitivity of a label-free biosensor application, it is pivotal to maximize the number of probe molecules immobilized on the semiconductor surface. Immobilization of the desired amount of aptamer molecules can be achieved by adjusting the degree of surface modification. The degree of surface functionality is varied by controlling the acid treatment time from 1 to 12 h. To confirm the functionality of the polypyrrole surface with different activation times, Fourier-transform infrared spectroscopy (FT-IR) was conducted as shown in **Figure 60**. Generally, all samples show the characteristic bands of polypyrrole as following: C=C and C–C

stretching vibration bands of pyrrole ring *ca.* 1540 cm^{-1}; =C–H in-plane vibration and C–N pyrrole ring stretching bands at 1277 and 1171 cm^{-1}; and C–H in-plane deformation vibration and –SO$_3$ overlap (due to the sodium *p*-toluenesulfonate doping effect during electropolymerization) bands *ca.* 1029 cm^{-1} [147-149]. The band at 961 cm^{-1} is assigned to the C–C out-of-plane deformation vibration of pyrrole ring. As the treatment time increased, the intensity of the C=O band (at 1698 cm^{-1}) gradually increases with respect to the C=C and C–C pyrrole vibrational bands (*ca.* 1554 cm^{-1}), resultantly, the value of the $I_{C=O}/I_{C=C}$ is enhanced from 0.37 to 0.65. Therefore, MCNF is successfully modified on the polypyrrole surface for binding aptamer immobilization.

To construct selective and stable aptasensor system, the HBsAg binding aptamer was subsequently attached onto the carboxylated MCNF surface using amide group coupling agent (4-(4,6-dimethoxy-1,3,5-triazin-2-yl)-4-methylmorpholinium chloride (DMTMM)) (**Figure 61**). As suggested in **Figure 62a** to **c**, the amount of immobilized aptamer on the carboxylated MCNF surface is controlled by extent of surface functionalization. The surface roughness progressively increases with enhancing activation time from smooth

(1 h) to rugged surface (12 h). The MCNF with 1 h, 6 h, and 12 h activation times are denoted as MCNF_1, MCNF_6, and MCNF_12. Additionally, to further characterize an amount of the binding aptamer immobilization, aptamer loading on the surface is quantified using a micro-volume UV-visible spectrophotometer (**Table 3**). A yield of immobilization and concentration of the conjugated aptamers are calculated for each case: 14.5% (11.3 ng μL^{-1}) for the MCNF_1; 32.8% (25.6 ng μL^{-1}) for the MCNF_6; and 57.4% (44.8 ng μL^{-1}) for the MCNF_12. Consequently, the values of different nanofilms clearly suggest that 12 h is the optimum activation time on the aptamer immobilization.
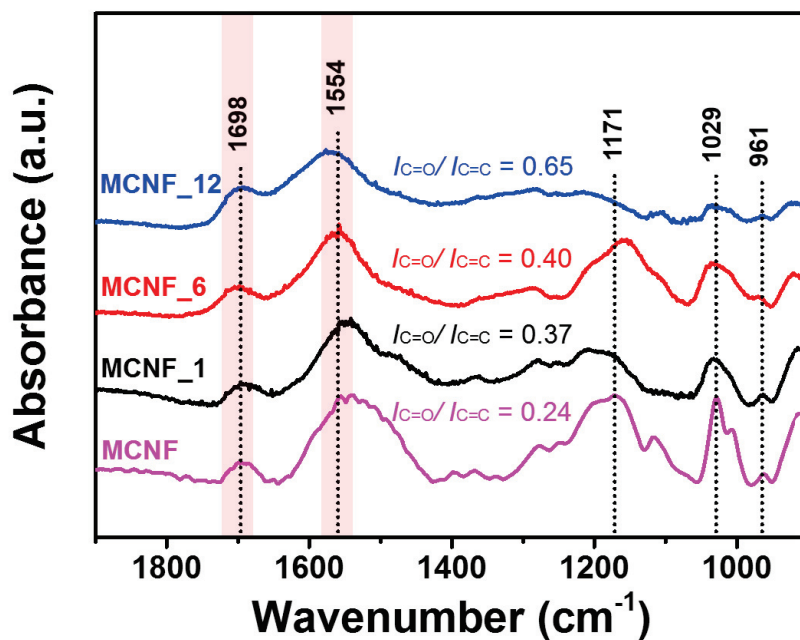
Figure 60. Fourier-transform infrared spectroscopy (FT-IR) spectra of polypyrrole and carboxylated polypyrrole nanowires with different acid treatment time (pink: polypyrrole; black: 1 h acid treatment; red: 6 h acid treatment; blue: 12 h acid treatment).
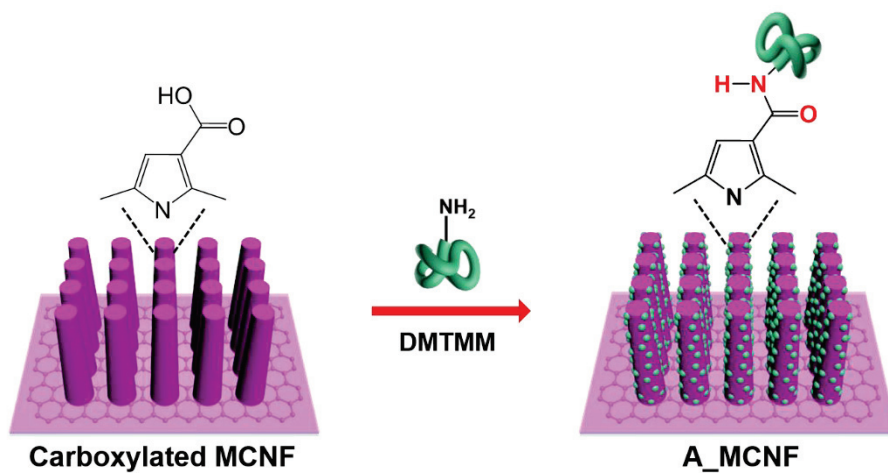
Figure 61. Schematic diagram of aptamer-conjugation reaction on the surface of carboxylated multidimensional conductive nanofilm.
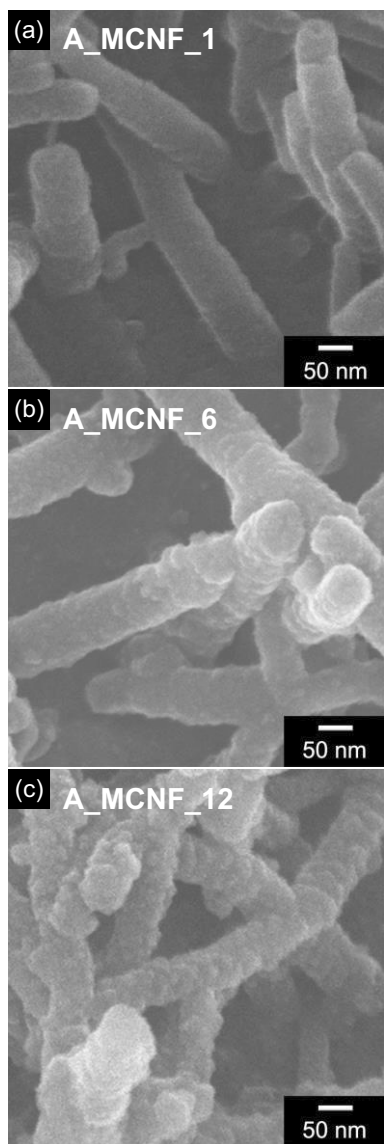
Figure 62. FE-SEM images of aptamer immobilized carboxylated polypyrrole nanowires with different acid treatment time: (a) 1 h, (b) 6 h, and (c) 12 h.

Table 3. Aptamer concentrations measured from the UV absorbance at 260 nm wavelength.

Acid treatment time	Washing sample[a] [ng/µL]	Immobilized aptamer[b] [ng/µL]	Percentage [%]
1 h	66.7	11.3	14.5
6 h	52.4	25.6	32.8
12 h	33.2	44.8	57.4

[a]These values are obtained by NanoQuant Plate (Infinite M200, TECAN trading); [b]Immobilized aptamer concentration is calculated by subtracting a) from standard sample concentration (standard sample concentration = 78.0 ng/µL).

3.3.3. Application for FET-type HBsAg aptasensor

The as prepared sensor system consists of silver source-drain electrodes and aptamer functionalized multidimensional conductive nanofilm (A_MCNF) as a sensing transducer (**Figure 63a**). To evaluate electrical functions of the A_MCNF system, current–voltage (I–V) measurements were conducted over voltage range of –0.5 to +0.5 V, without applying a gate voltage (V_G =0) (**Figure 63b**). The linear I–V curves suggest an Ohmic contact of the sensing materials without generating Schottky barriers owing to strong bonding between the sensing materials and the electrodes. A value of dI/dV, indicating a conductance of the MCNF, slightly decreases after acid treatment with replacement of the p-toluenesulfonic acid (pTSA) dopant anion with HSO^{4-} during the acid treatment [150]. Nonconductive binding aptamers also decrease a value of dI/dV when the binding aptamers are introduced onto the MCNF surface. Although there are modest differences in contact resistances throughout each sample, the linearity of the I–V curves is preserved because of originating from strong linkage between the sensing materials and the electrodes.

Figure 64a shows the assembled electrolyte gated field-effect transistor (FET)-type HBsAg aptasensor using the A_MCNF-based

147

electrode. The FET-type sensor platform consists of a transducer (A_MCNF), silver electrodes and surrounding medium (electrolyte). In detail, source (S) and drain (D) electrodes are deposited at both ends of the transducer channel. The liquid-ion-gated geometry is constructed with phosphate-buffered saline (PBS; pH 7.4) as a gate dielectric. To verify the charge transport behavior of the FET-type aptasensor, a dependence of the source–drain current (I_{SD}) with various gate voltage (V_G, from +0.2 to –0.8 V) is monitored with constant sweep rate (100 mV s^{-1}) of source–drain voltage (V_{SD}). In the I_{SD}-V_{SD} output characteristics in **Figure 64b**, the negative value of I_{SD} increases with negatively enhancing V_G, implying that holes (h$^+$) are the major charge carriers (p-type) of the A_MCNF-based aptasensor; this results from an increase in the oxidation level of the polymer chains [151]. Therefore, the A_MCNF-based aptasensor can effectively operate as an electrochemical sensor for detecting analytes in the solution.
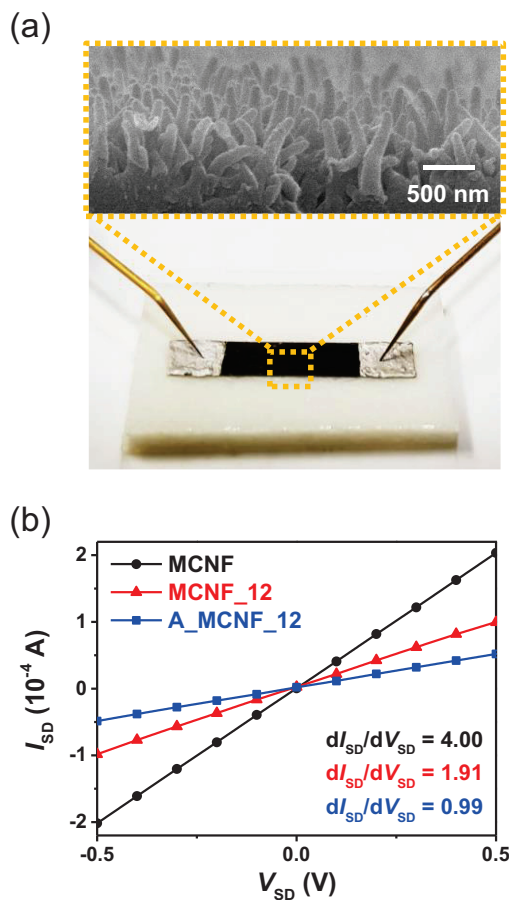
Figure 63. (a) Optical image of multidimensional conductive nanofilm-based aptasensor electrode (inset: FE-SEM image of transducer material of A_MCNF_12). (b) Current-voltage (*I-V*) curves of the each conductive nanofilm (black: pyrrole decorated nanofilm; red: carboxylated polypyrrole decorated nanofilm; blue: aptamer bonded-carboxylated polypyrrole decorated nanofilm).
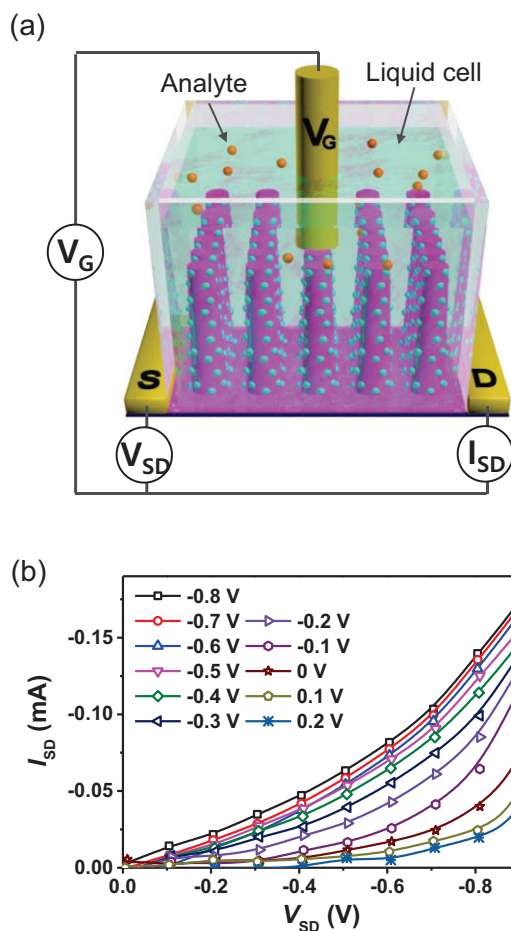
Figure 64. (a) Schematic diagram of a liquid-ion-gated FET-type sensor using MCNF coupled with HBsAg binding aptamer (V_G, V_{SD}, I_{SD}, S, D illustrates gate voltage, source-drain voltage, source-drain current, source, and drain, respectively). (b) I_{SD}-V_{SD} output curves of binding aptamer-conjugated MCNF aptasensor (V_G from +0.2 to -0.8 V at V_{SD} scan rate of -100 mVs^{-1}).

Sensing performance of the A_MCNF-based aptasensor is investigated by monitoring an electrical response upon exposure of target analyte (HBsAg) in real time. The sensing mechanism of the A_MCNF-based aptasensor is described using carrier accumulation as follows (**Figure 65**) [152]. A sensing mechanism of the A_MCNF-based aptasensor is described using charge carrier accumulation as follows. Generally, aptamers show negative charges in a PBS buffer solution due to phosphate groups in nucleic acid backbone [153]. Thus, the immobilized aptamers on the MCNF act as an additional gate voltage in the FET-type aptasensor. When target anlayte is added into the PBS buffer solution, morphology of the immobilized aptamer on the MCNF changes to a complicated tertiary structure to form HBsAg-binding aptamer complex. [96, 154] Then, folding of aptamer strand during the formation of HBsAg-aptamer complex reduces the negative gating effect of the aptamer. Consequently, a density of positively charged carriers (holes) at the surface of the nanofilm is reduced, leading to decrease in I_{SD}.

Due to intimate contact between the gate tip and sensor transducer (A_MCNF), the electrolyte based FET system is capable of achieving sufficient current level at low operating voltage (V_G = -50 mV; V_{SD} =

50 mV) upon insertion of the different analyte concentrations. After addition of the target analyte (HBsAg) into the chamber, the I_{SD} abruptly increased in negative direction (less than 5 s), then slightly decreased, and finally reached the saturated value (**Figure 66a**). The rapid decrease of the I_{SD} implies that charges due to the reaction between HBsAg and binding aptamers are transferred quickly to the nanofilm. Moreover, a minimum detectable level (MDL) of the aptasensor changes with morphology and an amount of functionality of the conductive nanofilm.

  First, the vertically aligned nanowire-based nanofilm displays higher sensitivity than that of the short nanorod-based and nanofiber network-based nanofilms because of the large active surface area to target analyte without interruption originating from entanglement of nanowires (**Figure 67**). An amount of functionality controls binding aptamer conjugation therefore it is also critical factor of the sensitivity to the anlayte. Consequently, the aptasensor based on 12 h acid-treated A_MCNF (A_MCNF_12) suggests a ultralow MDL of 10 aM (signal-to-noise: 3.14) that is more sensitive than that of lower acid treated cases (1 pM for 1 h acid-treated (A_MCNF_1) and 100 fM for 6 h acid-treated (A_MCNF_6) aptasensors) because of large active

surface area and high population of binding aptamers. Additionally, a MDL value of the A_MCNF_12 aptasensor is *ca.* 10^1 to 10^5 fold times more sensitive than previously reported HBsAg sensors (**Table 4**). [92-95,155-159].

Figure 66b shows the sensitivity (S) calibration curves of the A_MCNF aptasensors with different acid treatment times. The sensitivity is determined from the saturation point of the normalized current change ($[\Delta I_{SD}/I_0]$ (%)). Notably, the aptasensor calibration curves display a linear relationship with respect to HBsAg concentration; the obtained sensitivity calibration curves are as follows:

$$S_{A\_MCNF\_1} (\%) = -0.20215\log C - 0.45016$$

$$S_{A\_MCNF\_6} (\%) = -0.22184\log C - 0.86298$$

$$S_{A\_MCNF\_12} (\%) = -0.90939\log C - 3.07847$$

C: HBsAg concentration in fM

Especially, the A_MCNF_12 exhibits a wide linear detection range over an HBsAg concentration ranging from 10 aM to 0.1 µM without saturation. In contrast, the sensitivity signals of the other A_MCNF sensors begin to show linearity at *ca.* 100 fM for 6 h and 1 pM for 1 h, respectively, presenting short linear detection ranges. It is presumed

that most of the aptamer active sites are occupied before exposure to a high concentration of HBsAg, which lead to rapid saturation. Therefore, a high concentration of aptamers provided high sensitivity and slow saturation.
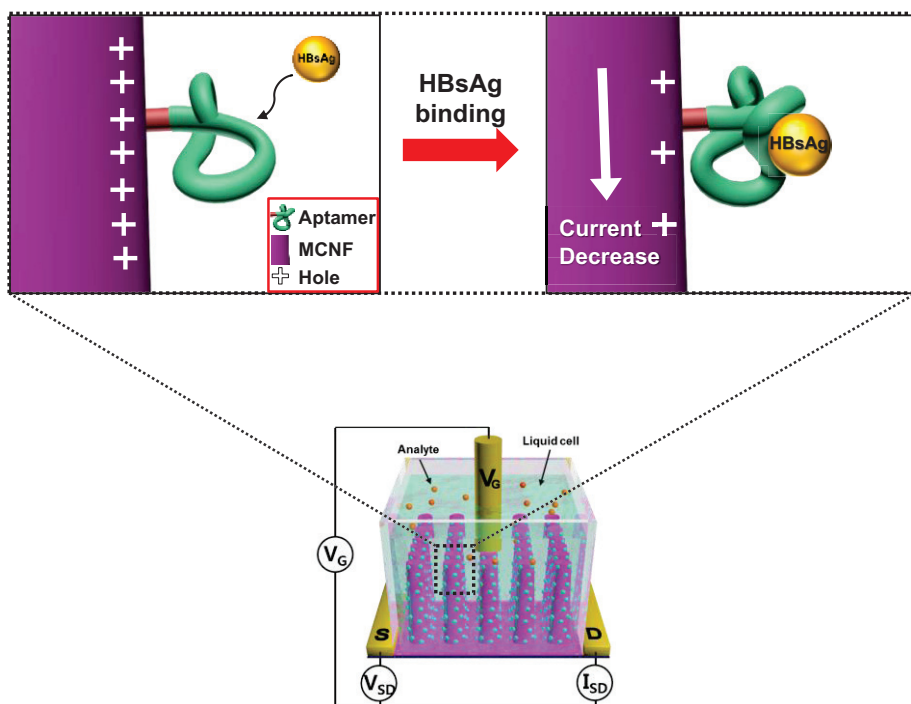
Figure 65. HBsAg molecule sensing mechanism of the A_MCNF aptasensor.
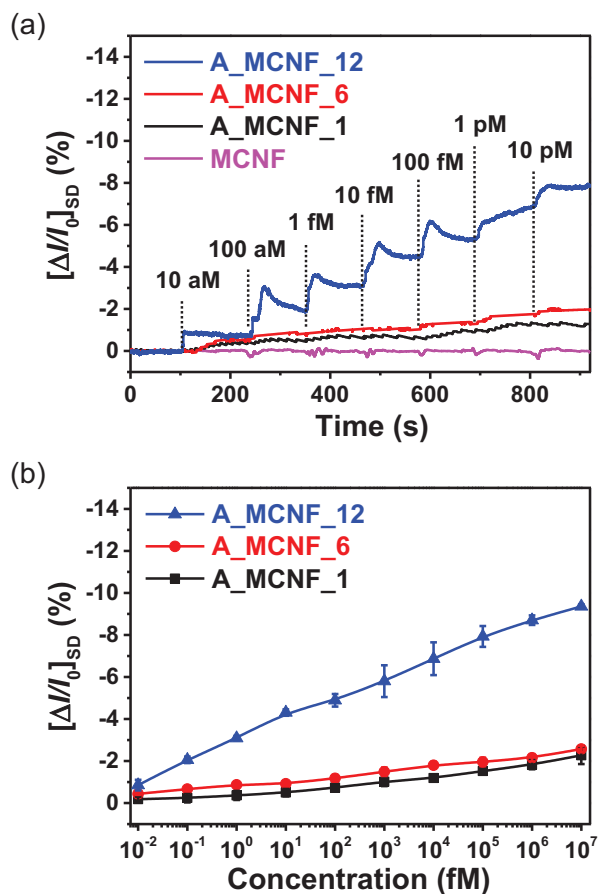
Figure 66. (a) Real-time responses of polypyrrole decorated conductive nanofilm sensor electrode (pink) and aptasensors based on the different amount of the functionalized carboxyl group on the conductive surface (black: 1h, red: 6h, and blue: 12 h acid treatment). (b) Calibration curves of different apsensors toward various HBsAg concentrations (black: 1h, red: 6h, and blue: 12 h acid treatment).
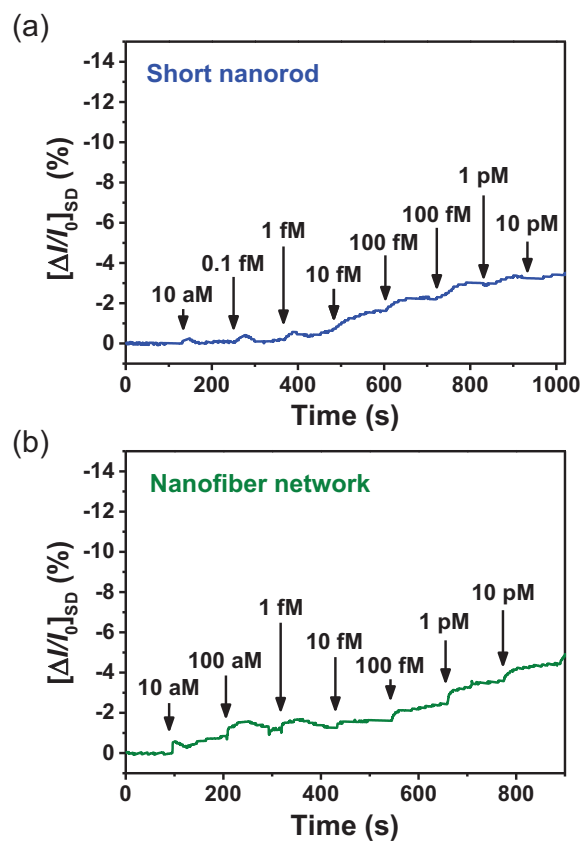
Figure 67. Real time response of (a) short nanorods and (b) network-like nanofibers-decorated conductive nanofilm aptasensors (12 h acid treatment).

Table 4. Comparison of the performance of previously reported HBsAg sensors

Material	Sensor type	Receptor	Detection limit [mol/L]	Ref.
Au nanoparticle	Chemiluminescence	Antibody	5.8×10^{-13}	[92]
Cy3 and Cy5 dye	FRET[a]	Aptamer	12.5×10^{-12}	[93]
Plasma treated Parylene -N film	SPR[b]	Antibody	4.2×10^{-13}	[94]
Amino-PS NPs[c]	Chemiluminescent ELISA[d]	Antibody	3.4×10^{-11}	[95]
SOI-NWs[e]	CMOSFET[f]	Antibody	7×10^{-14}	[155]
SnO$_2$	DG-ISFET[g]	Antibody	1.5×10^{-15}	[156]
CdTe@CdS labeled dendrimer	Electrochemiluminescence	Antibody	3.3×10^{-17}	[157]
Fe$_3$O$_4$ magnetic NP hemin/G-quadruplex DNAzyme	Electrochemical immunosassay	Antibody	7.9×10^{-15}	[158]
Multi-HAT-AuNP-Ab$_2$	Fluorescence ELISA	Antibody	8.3×10^{-14}	[159]
A_MCNF_12	FET-type	Aptamer	1×10^{-17}	This work

[a]Förster resonance energy transfer [b]Surface plasmon resonance [c]Amino functionalized polystyrene nanoparticle [d]Enzyme-linked immunosorbent assay [e]Silicon-on-isolator-nanowires [f]Complementary metal-oxide-semiconductor FET [g]Dual gate ion-sensitive FET

3.3.4. Flexibility and selectivity of FET-type HBsAg aptasensor

Flexibility and selectivity are important issues for biosensor application because a development of portable and wearable sensors has proven particularly challenging. For the flexible ability, **Figure 68** suggests the response changes of the A_MCNF_12 aptasensor after repeated folding and relaxing sequences. The detailed structure changes of the aptasensor are displayed in **Figure 69**. The sensitivity amount of the aptasensor maintained similar value (*ca.* 5-10%) until 200 cycles, and then improved until 500 cycles on account of covalent bonding of the binding aptamers on the surface and superb mechanical strength of the graphene substrate in the MCNF structure. Therefore, the MCNF-based aptasensor suggests flexibility and durability to apply flexible biosensor systems.

Furthermore, **Figure 70** shows the selective response of the A_MCNF_12h aptasensor toward HBsAg molecule. The selectivity test is evaluated by recording the real-time responses of I_{SD} upon addition of non-target molecules. Common serum protein, bovine serum albumin (BSA), immunoglobulin G (IgG), and small molecules such as ascorbic acid (AA) and uric acid (UA) are used as interfering molecules to establish the specificity of the aptasensor (**Figure 71**). As

shown in **Figure 70**, only small decreases in I_{SD} are observed (signal-to-noise: 1.60-1.98) for 100 nM of non-target serum proteins or small molecules. The small increase in I_{SD} is attributed to nonspecific binding that occurred due to the electrostatic interaction between the aptamer sequences and interfering molecules [83]. However, exposure to 1 fM of HBsAg causes a sharp decrease in I_{SD}, thereby certifying the selectivity of the A_MCNF_12 aptasensor. The ultimate goal of the biosensor is to discriminate HBsAg from other biomolecules contained in the human body. Hence, the sensing responses from diluted human serum, artificial saliva samples are evaluated. **Figure 72a** suggests that the A_MCNF_12 aptasensor exhibits noticeable current change upon introduction of 1 fM HBsAg in the human serum condition. 1 % diluted human serum was used to remove the distraction from other biomolecules [160]. Additionally, real-time sensitivity curves are also obtained in artificial saliva and real saliva environments (**Figure 72b** and **c**). The I_{SD} is clearly changed when the artificial and real saliva with 1 fM of HBsAg is injected into PBS electrolyte. However, the response times in artificial and real saliva tests are much slower than that of the others. It is speculated that the materials mixed to mimic the mucus in the artificial saliva would

interfere with the diffusion of target molecules and interrupting salivary bio-components, such as enzymes, blood cells and glycoproteins prevented the HBsAg from adsorbing onto the transducer surface.
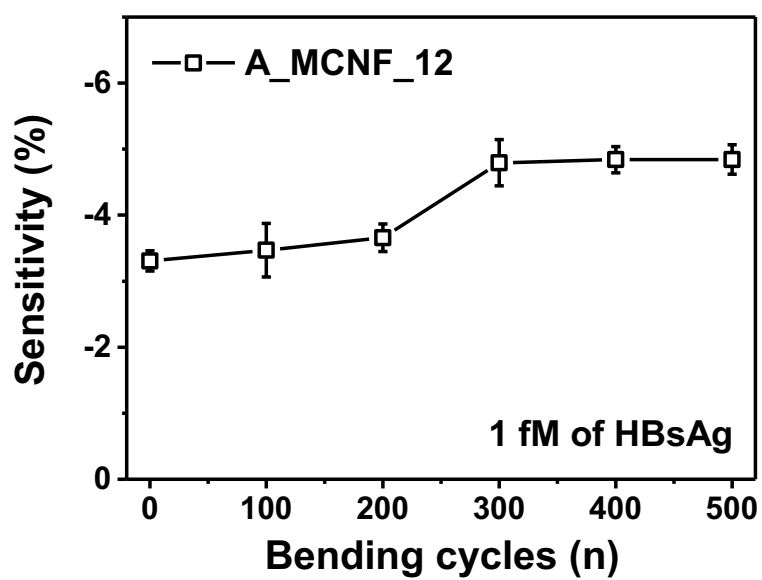
Figure 68. Sensing performance of the A_MCNF-based aptasensor after repeated bending cycles.
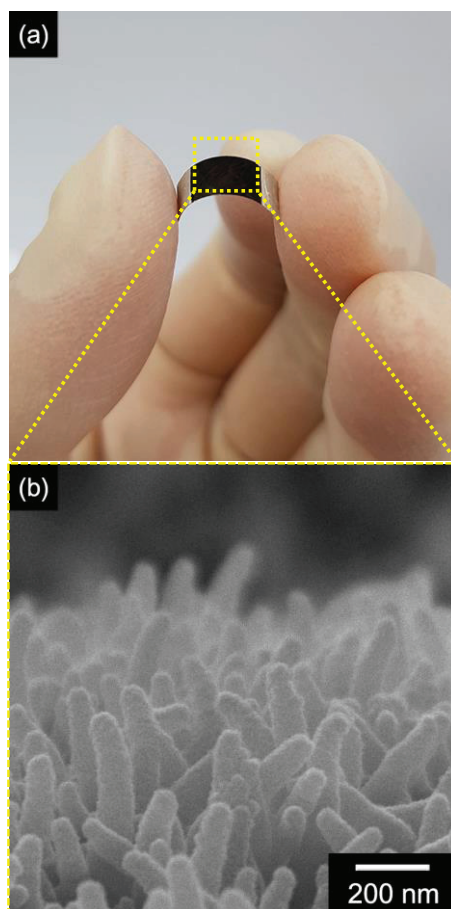
Figure 69. (a) Optical and (b) FE-SEM images of the bent aptasensor electrode.
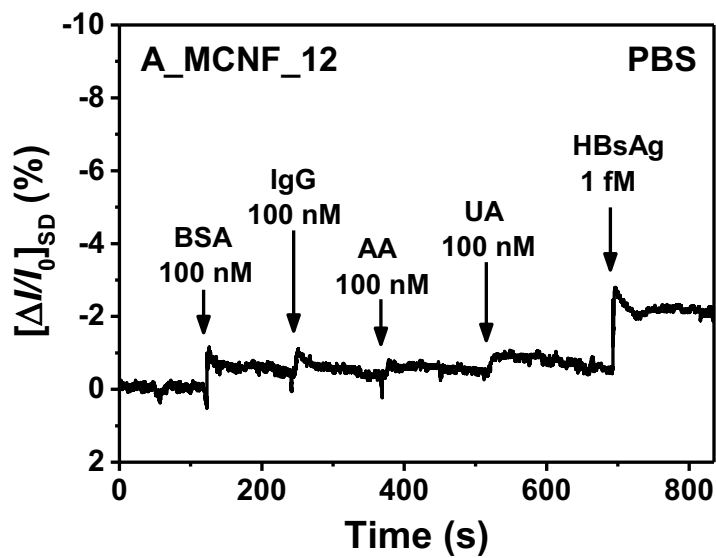
Figure 70. Selective responses of the A_MCNF-based aptasensor toward nontarget (BSA, IgG, ascorbic acid, and uric acid) and target (HBsAg) analytes.
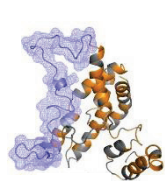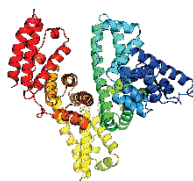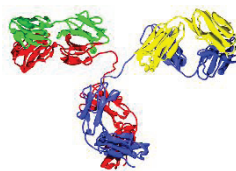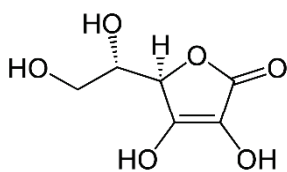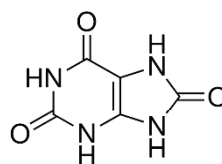
Figure 71. Molecular diagram of the different biomolecules.
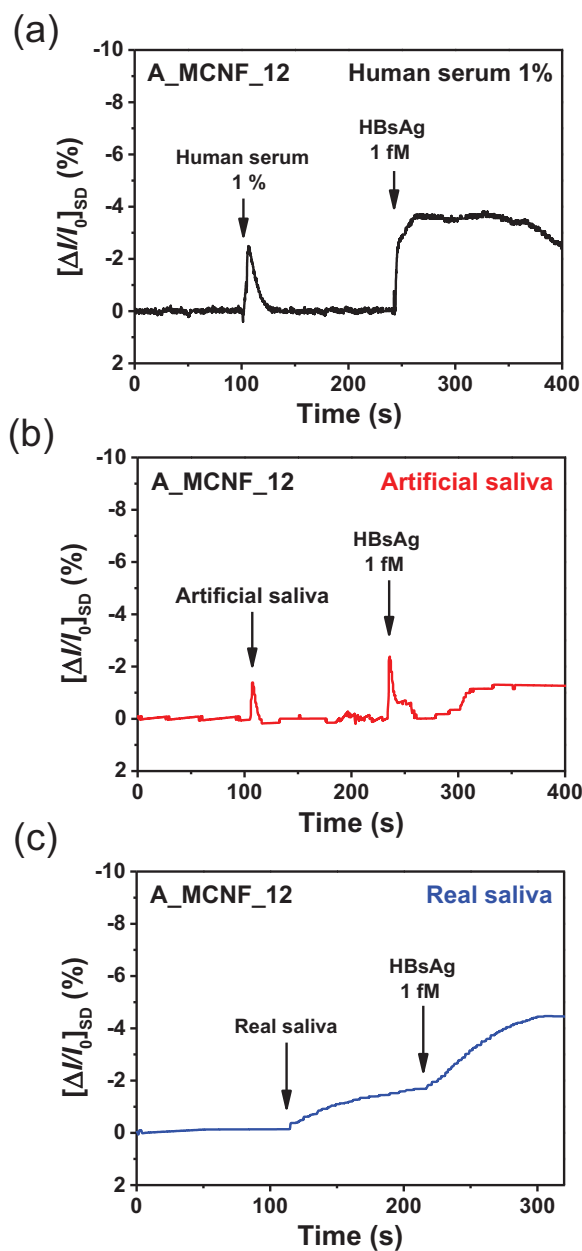
Figure 72. Real-time responses for the selectivity in different solution environments: (a) diluted human serum; (b) artificial saliva; (c) real saliva sample.

4. Conclusion

  Various polypyrrole nanowire-based 3D conductive nanofilms, whose physical and chemical properties were successfully altered by three types of modifications methods, suggested potential properties in the diverse chemical/biosensors applications. The properties of polypyrrole nanowire-based 3D conductive nanofilms, including doping level, noble metal decoration, and degree of surface functionalization were optimized to improve sensitivity and stability of the chemical/biosensors. The subtopics are concluded in the view point of each subtopic as follows:

1. The three-dimensional microvillus-like polypyrrole nanowire-based conductive nanofilms with different morphologies and doping levels were facilely synthesized for ammonia and methanol gas sensor. The morphologies of 3D MCNs were easily controlled by changing the polymerization temperature during the electropolymerzation of pyrrole. The polypyrole nanostructure transformed from nanowire to micrograins due to the enlargement of micelle sizes as temperature increases. 3D MCN polymerized at 5ºC was then went through electrochemical doping level control, resulting in different polymer

chain structure that are neutral, polaron, bipolaron, and over-oxidation. Increasing doping level maximized electrical conductivity, carrier density, and carrier mobility of the conductive films. The resulting doping level controlled 3D MCNs were used in a gas sensor for the detection of the VOC gases, NH_3 and MeOH, with ultrahigh sensitivity at room temperature. Enhanced sensitivity was observed as the doping level of conductive nanofilm increased. In particular, the 3D MCN_+1.0V exhibited a minimum detectable level (MDL) of 1 ppb to NH_3 and 0.1 ppm to MeOH gas, respectively. Furthermore, 3D MCN_+1.0V showed fast response/recovery time, excellent flexibility and selectivity.

2. The Pd nanoparticle-decorated three dimensional polypyrrole nanostructures (PPyPd)-based hydrogen sensors were successfully fabricated by sequential electrodeposition of polypyrrole and Pd NPs on interdigitated array (IDA) electrodes. The population and morphologies of decorated Pd NPs were varied by changing concentration of metal precursor, $PdCl_2$. In addition, the diameter of the Pd NPs increased as the deposition temperature elevated. The as-prepared PPyPds were used in gas sensor for the detection of the

hydrogen gas with high sensitivity at room temperature. In particular, decoration of larger size of Pd NP exhibited a minimum detectable level (MDL) of 5 ppm, which is more sensitive than smaller Pd NPs. The PPy nanostructure provided the large surface area for discrete anchoring of Pd NPs and diameter increase in Pd NPs provided more chances of creating conductive pathways. Furthermore, the PPyPd sensors manifested a wide linear detectable range (5 – 2000 ppm) and good cyclability.

3. The aptamer functionalized multidimensional conductive nanofilm (A_MCNF)-based aptasensor was fabricated using electro-polymerization process and acid treatment. The *L/D* ratios of polypyrrole nanowires (PPyNW) in MCNFs were easily controlled by changing the reaction time of electropolymerization at fixed temperatures of 5ºC. Subsequently, the surface of the PPyNW were immersed in acid solution to produce carboxylated PPyNW (CPPyNW) as to form covalent bonding with aptamers. The surface functionality was varied by changing the acid treatment time. The maximized active surface area that comes from vertically oriented carboxylated polypyrrole nanowires (CPPyNW) enhances decoration amount of the

HBsAg binding aptamers, increasing its affinity to HBsAg molecule. As a result, the A_MCNF aptasensor suggested high sensitivity (~ 10 aM) to HBsAg that is $10^1 - 10^5$ fold times higher than that of other sensor systems. Furthermore, the A_MCNF aptasensor displayed flexibility and high specificity to the HBsAg in mixtures of interfering molecules, diluted human serum and artificial saliva.

References

[1] A. G. MacDiarmid, *Angew. Chem. Int. Ed.,* **2001**, 40, 2581.

[2] H. Shirakawa, *Angew. Chem. Int. Ed.,* **2001**, 40, 2574.

[3] A. J. Heeger, *Angew. Chem. Int. Ed.,* **2001**, 40, 2591.

[4] T.-H. Le, Y. Kim, H. Yoon, *Polymers,* **2017**, 9, 150.

[5] H. Yoon, J. Jang, *Adv. Funct. Mater.,* **2009**, 19, 1567.

[6] E. Roduner, *Chem. Soc. Rev.,* **2006**, 35, 583.

[7] F. Jabbari, A. Rajabpour, S. Saedodin, *Chem. Eng. Sci.,* **2017**, 174, 67.

[8] J. Jang, in *Emissive Materials Nanomaterials*, Springer, Berlin, Heidelberg, **2006**, pp. 189.

[9] J. Jang, Y. Nam, H. Yoon, *Adv. Mater.,* **2005**, 17, 1382.

[10] J. Jang, H. Yoon, *Small,* **2005**, 1, 1195.

[11] S. J. Park, O. S. Kwon, J. E. Lee, J. Jang, H. Yoon, *Sensors,* **2014**, 14, 3604.

[12] J. S. Lee, J. Oh, S. G. Kim, J. Jang, *Small,* **2015**, 11, 2399.

[13] F. Meng, W. Shi, Y. Sun, X. Zhu, G. Wu, C. Ruan, X. Liu, D. Ge, *Biosens. Bioelectron.,* **2013**, 42, 141.

[14] W. Na, J. W. Park, J. H. An, J. Jang, *J. Mater. Chem. B,* **2016**, 4, 5025.

[15] O. S. Kwon, S. J. Park, H.-W. Park, T. Kim, M. Kang, J. Jang, H. Yoon, *Chem. Mater.,* **2012**, 24, 4088.

[16] C.-M. Yoon, K. H. Cho, Y. Jang, J. Kim, K. Lee, H. Yu, S. Lee, J. Jang, *Langmuir,* **2018**, 34, 15773.

[17] J. J. S. Rickard, I. Farrer, P. Goldberg Oppenheimer, *ACS Nano,* **2016**, 10, 3865.

[18] T. K. Das, S. Prusty, *Polym.-Plast. Technol. Eng.,* **2012**, 51, 1487.

[19] D. L. Wise, G. E. Winek, D. J. Trantolo, T. M. Cooper, J. D.

Gresser, *Electrical and Optical Polymer Systems: Fundamentals: Methods, and Applications,* Vol. 17, Marcel Dekker, Inc., New York, **1998**.

[20] J. Rodriguez, H.-J. Grande, T. F. Otero, in *Handbook of Organic Conductive Molecules and Polymers,* Vol. 2 (Ed.: H. S. Nalwa), John Wiley and Sons, **1997**, p. 415.

[21] J. Simonet, J. Rault-Berthelot, *Prog. Solid State Chem.,* **1991**, 21, 1.

[22] B. Scrosati, G. Stienen, *Applications of Electroactive Polymers*, Chapman & Hall, London, **1993**.

[23] A. J. Heeger, *Handbook of Conducting Polymers,* Vol. 1, Marcel Dekker, New York, **1986**.

[24] G. H. Gorman, R. H. Grubbs, in *Conjugated Polymers* (Eds.: J. L. Brédas, R. Silbey), Springer, Dordrecht, **1991**, pp. 1.

[25] R. E. Myers, *J. Electron. Mater.,* **1986**, 15, 61.

[26] C. Li, H. Bai, G. Shi, *Chem. Soc. Rev.,* **2009**, 38, 2397.

[27] K. S. Novoselov, A. K. Geim, S. V. Morozov, D. Jiang, Y. Zhang, S. V. Dubonos, I. V. Grigorieva, A. A. Firsov, *Science,* **2004**, 306, 666.

[28] O. S. Kwon, H. S. Song, T. H. Park, J. Jang, *Chem. Rev.,* **2019**, 119, 36.

[29] S. Haar, A. Ciesielski, J. Clough, H. Yang, R. Mazzaro, F. Richard, S. Conti, N. Merstorf, M. Cecchini, V. Morandi, C. Casiraghi, P. Samorì, *Small,* **2015**, 11, 1691.

[30] W. Zhao, M. Fang, F. Wu, H. Wu, L. Wang, G. Chen, *J. Mater. Chem.,* **2010**, 20, 5817.

[31] C.-Y. Su, A.-Y. Lu, Y. Xu, F.-R. Chen, A. N. Khlobystov, L.-J. Li, *ACS Nano,* **2011**, 5, 2332.

[32] Y. Zhang, L. Zhang, C. Zhou, *Acc. Chem. Res.,* **2013**, 46, 2329.

[33] H. Ago, in *Frontiers of Graphene and Carbon Nanotubes: Devices and Applications* (Ed.: K. Matsumoto), Springer Japan,

Tokyo, **2015**, pp. 3.

[34] O. S. Kwon, S. H. Lee, S. J. Park, J. H. An, H. S. Song, T. Kim, J. H. Oh, J. Bae, H. Yoon, T. H. Park, J. Jang, *Adv. Mater.,* **2013**, 25, 4177.

[35] A. K. Geim, K. S. Novoselov, *Nat. Mater.,* **2007**, 6, 183.

[36] E. Kibena, M. Mooste, J. Kozlova, M. Marandi, V. Sammelselg, K. Tammeveski, *Electrochem. Commun.,* **2013**, 35, 26.

[37] W. Schwarzacher, *Electrochem. Soc. Interface,* **2006**, 15, 32.

[38] E. I. Cooper, C. Bonhote, J. Heidmann, Y. Hsu, P. Kern, J. W. Lam, M. Ramasubramanian, N. Robertson, L. T. Romankiw, H. Xu, *IBM J. Res. Dev.,* **2005**, 49, 103.

[39] S. Sadki, P. Schottland, N. Brodie, G. Sabouraud, *Chem. Soc. Rev.,* **2000**, 29, 283.

[40] E. Song, J.-W. Choi, *Nanomaterials,* **2013**, 3, 498.

[41] S. S. Rao, J. Winter, *Front. Neuroeng.,* **2009**, 2.

[42] A. Kaynak, *Mater. Res. Bull.,* **1997**, 32, 271.

[43] L. Santos, J. P. Neto, A. Crespo, P. Baião, P. Barquinha, L. Pereira, R. Martins, E. Fortunato, in *Electroplating of Nanostructures* (Ed.: A. Mahmood), IntechOpen, **2015**.

[44] B. M. Mundotiya, W. Ullah, in *Novel Metal Electrodeposition and the Recent Application* (Eds.: M. Sone, K. Masu), IntechOpen, **2018**.

[45] I. Zhitomirsky, *Adv. Colloid Interface Sci.,* **2002**, 97, 279.

[46] Y. Wang, L. Zhao, Y. Zhao, W. Y. Wang, Y. Liu, C. Gu, J. Li, G. Zhang, T. J. Huang, S. Yang, *Adv. Mater.,* **2018**, 30, 1805686.

[47] M. Sookhakian, E. Zalnezhad, Y. Alias, *Sens. Actuators, B,* **2017**, 241, 1.

[48] C. Zhu, D. Du, A. Eychmüller, Y. Lin, *Chem. Rev.,* **2015**, 115, 8896.

[49] J. L. Brédas, G. B. Street, *Acc. Chem. Res.,* **1985**, 18, 309.

[50] M. Mishra, *Encyclopedia of Polymer Applications*, 1st ed., CRC Press, **2018**.

[51] P. Kar, *Doping in Conjugated Polymers*, Wiley-Scrivener, Massachusetts, **2013**.

[52] S. H. Cho, K. T. Song, J. Y. Lee, in *Conjugated polymers: theory, synthesis, properties, and characterization*, 3rd ed., CRC Press, **2007**.

[53] H. Ge, G. Qi, E.-T. Kang, K. G. Neoh, *Polymer,* **1994**, 35, 504.

[54] J. Mostany, B. R. Scharifker, *Electrochim. Acta,* **1997**, 42, 291.

[55] T. F. Otero, *J. Mater. Chem. B,* **2013**, 1, 3754.

[56] S. D. Jayasena, *Clin. Chem.,* **1999**, 45, 1628.

[57] A. D. Keefe, S. Pai, A. Ellington, *Nat. Rev. Drug Discovery,* **2010**, 9, 537.

[58] N. J. Ronkainen, H. B. Halsall, W. R. Heineman, *Chem. Soc. Rev.,* **2010**, 39, 1747.

[59] Y.-B. Hahn, R. Ahmad, N. Tripathy, *Chem. Commun.,* **2012**, 48, 10369.

[60] W. K. Jang, J. Yun, H.-I. Kim, Y.-S. Lee, *Carbon letters,* **2012**, 13, 88.

[61] B. Timmer, W. Olthuis, A. v. d. Berg, *Sens. Actuators, B,* **2005**, 107, 666.

[62] S. Christie, E. Scorsone, K. Persaud, F. Kvasnik, *Sens. Actuators, B,* **2003**, 90, 163.

[63] C. S. Rout, M. Hegde, A. Govindaraj, C. N. R. Rao, *Nanotechnology,* **2007**, 18, 205504.

[64] K. Wetchakun, T. Samerjai, N. Tamaekong, C. Liewhiran, C. Siriwong, V. Kruefu, A. Wisitsoraat, A. Tuantranont, S. Phanichphant, *Sens. Actuators, B,* **2011**, 160, 580.

[65] Ishpal, A. Kaur, *J. Appl. Phys.,* **2013**, 113, 094504.

[66] F. Miramirkhani, A. H. Navarchian, *IEEE Sens. J,* **2017**, 17, 2992.

[67] S. Bagchi, R. Achla, S. K. Mondal, *Sens. Actuators, B,* **2017**, 250,

52.

[68] J. G. Webster, H. Eren, *Measurement, Instrumentation, and Sensors Handbook: Electromagnetic, Optical, Radiation, Chemical, and Biomedical Measurement*, 2nd ed., CRC Press, **2017**.

[69] G. Korotcenkov, S. D. Han, J. R. Stetter, *Chem. Rev.,* **2009**, 109, 1402.

[70] S. K. Arya, S. Krishnan, H. Silva, S. Jean, S. Bhansali, *Analyst,* **2012**, 137, 2743.

[71] Y. H. Hu, L. Zhang, *Adv. Mater.,* **2010**, 22, E117.

[72] L. Jia, X. Sun, Y. Jiang, S. Yu, C. Wang, *Adv. Funct. Mater.,* **2015**, 25, 1814.

[73] S. Xu, D. Li, P. Wu, *Adv. Funct. Mater.,* **2015**, 25, 1127.

[74] T. Hübert, L. Boon-Brett, G. Black, U. Banach, *Sens. Actuators, B,* **2011**, 157, 329.

[75] A. Chen, C. Ostrom, *Chem. Rev.,* **2015**, 115, 11999.

[76] D. H. Shin, J. S. Lee, J. Jun, J. H. An, S. G. Kim, K. H. Cho, J. Jang, *Sci. Rep.,* **2015**, 5, 12294.

[77] M. Gao, M. Cho, H.-J. Han, Y. S. Jung, I. Park, *Small,* **2018**, 14, 1703691.

[78] J. Kim, A. S. Campbell, B. E.-F. de Ávila, J. Wang, *Nat. Biotechnol.,* **2019**, 37, 389.

[79] H. Yang, D. Kim, J. Kim, D. Moon, H. S. Song, M. Lee, S. Hong, T. H. Park, *ACS Nano,* **2017**, 11, 11847.

[80] N. Reta, C. P. Saint, A. Michelmore, B. Prieto-Simon, N. H. Voelcker, *ACS Appl. Mater. Interfaces,* **2018**, 10, 6055.

[81] N. J. Ronkainen, H. B. Halsall, W. R. Heineman, *Chem. Soc. Rev.,* **2010**, 39, 1747.

[82] M. S. Kim, K. H. Cho, K. H. Park, J. Jang, J.-S. Hahn, *Nucleic Acids Res.,* **2018**, 47, 1211.

[83] H. Xie, S.-C. Luo, H.-h. Yu, *Small,* **2009**, 5, 2611.

[84] D. Wang, V. Noël, B. Piro, *Electronics,* **2016**, 5, 9.

[85] C. Trépo, H. L. Y. Chan, A. Lok, *Lancet (London, England),* **2014**, 384, 2053.

[86] Y.-F. Liaw, *Hepatology,* **2011**, 53, 2121.

[87] A. J. V. Thompson, T. Nguyen, D. Iser, A. Ayres, K. Jackson, M. Littlejohn, J. Slavin, S. Bowden, E. J. Gane, W. Abbott, G. K. K. Lau, S. R. Lewin, K. Visvanathan, P. V. Desmond, S. A. Locarnini, *Hepatology,* **2010**, 51, 1933.

[88] I. Köksal, K. Çetinkaya, F. Aker, *Ophthalmologica,* **1992**, 204, 19.

[89] R. M. Scott, R. Snitbhan, W. H. Bancroft, H. J. Alter, M. Tingpalapong, *J. Infect. Dis.,* **1980**, 142, 67.

[90] P. Karayiannis, D. M. Novick, A. S. Lok, M. J. Fowler, J. Monjardino, H. C. Thomas, *Br. Med. J.,* **1985**, 290, 1853.

[91] M. Deguchi, N. Yamashita, M. Kagita, S. Asari, Y. Iwatani, T. Tsuchida, K. Iinuma, I. K. Mushahwar, *J. Virol. Methods,* **2004**, 115, 217.

[92] S. Sabouri, H. Ghourchian, M. Shourian, M. Boutorabi, *Anal. Methods,* **2014**, 6, 5059.

[93] S.-K. Suh, S. Song, H.-B. Oh, S.-H. Hwang, S. S. Hah, *Analyst,* **2014**, 139, 4310.

[94] A. Kamińska, E. Witkowska, K. Winkler, I. Dzięcielewski, J. L. Weyher, J. Waluk, *Biosens. Bioelectron.,* **2015**, 66, 461.

[95] N. Ma, C. Ma, N. Wang, C. Li, S. Elingarami, X. Mou, Y. Tang, S. Zheng, N. He, *J. Nanosci. Nanotechnol.,* **2014**, 14, 3348.

[96] Z. Xi, R. Huang, Z. Li, N. He, T. Wang, E. Su, Y. Deng, *ACS Appl. Mater. Interfaces,* **2015**, 7, 11215.

[97] S. Shi, X. Yu, Y. Gao, B. Xue, X. Wu, X. Wang, D. Yang, H. Zhu, *J. Virol.,* **2014**, 88, 1990.

[98] F. Chen, Y. Hu, D. Li, H. Chen, X.-L. Zhang, *PLOS ONE,* **2009**,

4, e8142.

[99] K. Butz, C. Denk, B. Fitscher, I. Crnkovic-Mertens, A. Ullmann, C. H. Schröder, F. Hoppe-Seyler, *Oncogene,* **2001**, 20, 6579.

[100] J. Liu, Y. Yang, B. Hu, Z.-y. Ma, H.-p. Huang, Y. Yu, S.-p. Liu, M.-j. Lu, D.-l. Yang, *Virol. Sin.,* **2010**, 25, 27.

[101] L. A. Donnell-Fink, C. Arbelaez, J. E. Collins, A. Novais, A. Case, M. L. Pisculli, W. M. Reichmann, J. N. Katz, E. Losina, R. P. Walensky, *J. Acquired Immune Defic. Syndr.,* **2012**, 61, 588.

[102] A. Lackner, H. H. Kessler, C. Walch, S. Quasthoff, R. B. Raggam, *J. Med. Virol.,* **2010**, 82, 1582.

[103] H. P. Lawrence, *J Can Dent Assoc.,* **2002**, 68, 170.

[104] C.-Z. Zhang, X.-Q. Cheng, J.-Y. Li, P. Zhang, P. Yi, X. Xu, X.-D. Zhou, *Int. J. Oral Sci.,* **2016**, 8, 133.

[105] M. Castagnola, P. M. Picciotti, I. Messana, C. Fanali, A. Fiorita, T. Cabras, L. Calò, E. Pisano, G. C. Passali, F. Iavarone, G. Paludetti, E. Scarano, *Acta Otorhinolaryngol. Ital.,* **2011**, 31, 347.

[106] K. H. Cho, D. H. Shin, J. Oh, J. H. An, J. S. Lee, J. Jang, *ACS Appl. Mater. Interfaces,* **2018**, 10, 28412.

[107] G. P. Kittlesen, H. S. White, M. S. Wrighton, *J. Am. Chem. Soc.,* **1984**, 106, 7389.

[108] H. Shafiee, M. K. Kanakasabapathy, F. Juillard, M. Keser, M. Sadasivam, M. Yuksekkaya, E. Hanhauser, T. J. Henrich, D. R. Kuritzkes, K. M. Kaye, U. Demirci, *Sci. Rep.,* **2015**, 5, 9919.

[109] J. Huang, K. Wang, Z. Wei, *J. Mater. Chem.,* **2010**, 20, 1117.

[110] J. Zang, S.-J. Bao, C. M. Li, H. Bian, X. Cui, Q. Bao, C. Q. Sun, J. Guo, K. Lian, *J. Phy. Chem. C,* **2008**, 112, 14843.

[111] K. Streletzky, G. D. J. Phillies, *Langmuir,* **1995**, 11, 42.

[112] M. Kumbhakar, T. Goel, T. Mukherjee, H. Pal, *J. Phy. Chem. B,* **2004**, 108, 19246.

[113] R. R. Balmbra, J. S. Clunie, J. M. Corkill, J. F. Goodman, *Trans.*

Faraday Society, **1962**, 58, 1661.

[114] J. Huang, B. Quan, M. Liu, Z. Wei, L. Jiang, *Macromol. Rapid Commun.,* **2008**, 29, 1335.

[115] M. Bouabdallaoui, Z. Aouzal, S. B. Jadi, A. E. Jaouhari, M. Bazzaoui, G. Lévi, J. Aubard, E. A. Bazzaoui, *J. Solid State Electrochem.,* **2017**, 21, 3519.

[116] J. Ouyang, Q. F. Xu, C. W. Chu, Y. Yang, G. Li, J. Shinar, *Polymer,* **2004**, 45, 8443.

[117] D. S. H. Charrier, R. A. J. Janssen, M. Kemerink, *Chem. Mater.,* **2010**, 22, 3670.

[118] L. Al-Mashat, C. Debiemme-Chouvy, S. Borensztajn, W. Wlodarski, *J. Phy. Chem. C,* **2012**, 116, 13388.

[119] E. Mazzotta, A. Caroli, A. Pennetta, G. E. De Benedetto, E. Primiceri, A. G. Monteduro, G. Maruccio, C. Malitesta, *RSC. Adv.,* **2018**, 8, 10367.

[120] T. R. Soreta, J. Strutwolf, O. Henry, C. K. O'Sullivan, *Langmuir,* **2010**, 26, 12293.

[121] W. Kim, D. H. Shin, J. Jun, J. H. Kim, J. Jang, *Adv. Mater. Interfaces,* **2017**, 4, 1700573.

[122] M. Iqbal, C. Li, K. Wood, B. Jiang, T. Takei, Ö. Dag, D. Baba, A. S. Nugraha, T. Asahi, A. E. Whitten, M. S. A. Hossain, V. Malgras, Y. Yamauchi, *Chem. Mater.,* **2017**, 29, 6405.

[123] S. Ko, J. Jang, *Angew. Chem. Int. Ed.,* **2006**, 45, 7564.

[124] M. E. Hyde, R. G. Compton, *J. Electroanal. Chem.,* **2003**, 549, 1.

[125] V. Agarwal, I. Aruna, V. Banerjee, B. R. Mehta, *Phys. Rev. B,* **2006**, 74, 035412.

[126] J. Ustarroz, X. Ke, A. Hubin, S. Bals, H. Terryn, *J. Phy. Chem. C,* **2012**, 116, 2322.

[127] R. M. Penner, *J. Phy. Chem. B,* **2002**, 106, 3339.

[128] B. M. Quinn, C. Dekker, S. G. Lemay, *J. Am. Chem. Soc.,* **2005**, 127, 6146.

[129] S.-Y. Cho, H. Ahn, K. Park, J. Choi, H. Kang, H.-T. Jung, *ACS Sens.,* **2018**, 3, 1876.

[130] X. Q. Zeng, M. L. Latimer, Z. L. Xiao, S. Panuganti, U. Welp, W. K. Kwok, T. Xu, *Nano Lett.,* **2011**, 11, 262.

[131] F. Yang, S.-C. Kung, M. Cheng, J. C. Hemminger, R. M. Penner, *ACS Nano,* **2010**, 4, 5233.

[132] T. Xu, M. P. Zach, Z. L. Xiao, D. Rosenmann, U. Welp, W. K. Kwok, G. W. Crabtree, *Appl. Phys. Lett.,* **2005**, 86, 203104.

[133] O. Dankert, A. Pundt, *Appl. Phys. Lett.,* **2002**, 81, 1618.

[134] S. Mubeen, T. Zhang, B. Yoo, M. A. Deshusses, N. V. Myung, *J. Phy. Chem. C,* **2007**, 111, 6321.

[135] X. Tang, P.-A. Haddad, N. Mager, X. Geng, N. Reckinger, S. Hermans, M. Debliquy, J.-P. Raskin, *Sci. Rep.,* **2019**, 9, 3653.

[136] M. H. Seo, E. J. Lim, S. M. Choi, S. H. Nam, H. J. Kim, W. B. Kim, *Int. J. Hydrogen Energy,* **2011**, 36, 11545.

[137] C. M. Ghimbeu, C. Zlotea, R. Gadiou, F. Cuevas, E. Leroy, M. Latroche, C. Vix-Guterl, *J. Mater. Chem.,* **2011**, 21, 17765.

[138] G. K. Reddy, C. Ling, T. C. Peck, H. Jia, *RSC. Adv.,* **2017**, 7, 19645.

[139] C. Yue, J. Wang, L. Han, L. Chang, Y. Hu, H. Wang, *Fuel Process. Technol.,* **2015**, 135, 125.

[140] W. Fan, J. E. Morris, *Thin Solid Films,* **1994**, 246, 17.

[141] J. S. Lee, S. G. Kim, S. Cho, J. Jang, *Nanoscale,* **2015**, 7, 20665.

[142] Y. J. Zou, Q. Y. Wang, C. L. Xiang, C. Y. Tang, H. L. Chu, S. J. Qiu, E. H. Yan, F. Xu, L. X. Sun, *Int. J. Hydrogen Energy,* **2016**, 41, 5396.

[143] D.-T. Phan, G.-S. Chung, *Sens. Actuators, B,* **2014**, 199, 354.

[144] A. Fakhry, F. Pillier, C. Debiemme-Chouvy, *J. Mater. Chem. A,*

2014, 2, 9859.

[145] Z. Xia, S. Wang, L. Jiang, H. Sun, G. Sun, *J. Power Sources,* **2014**, 256, 125.

[146] J. Hazarika, A. Kumar, *J. Phy. Chem. B,* **2017**, 121, 6926.

[147] M. M. Abdi, H. N. M. E. Mahmud, A. Kassim, W. M. M. Yunus, Z. A. Talib, M. J. Haron, *Polym. Sci., Ser. B,* **2010**, 52, 662.

[148] A. Kaynak, *Fibers Polym.,* **2009**, 10, 590.

[149] M. Forsyth, V. T. Truong, *Polymer,* **1995**, 36, 725.

[150] O. S. Kwon, S. J. Park, J. Jang, *Biomaterials,* **2010**, 31, 4740.

[151] J. Travas-Sejdic, N. Aydemir, B. Kannan, D. E. Williams, J. Malmström, *J. Mater. Chem. B,* **2014**, 2, 4593.

[152] Y. Ohno, K. Maehashi, K. Matsumoto, *J. Am. Chem. Soc.,* **2010**, 132, 18012.

[153] T. Hermann, D. J. Patel, *Science,* **2000**, 287, 820.

[154] Y. D. Ivanov, T. O. Pleshakova, A. F. Kozlov, K. A. Malsagova, N. V. Krohin, V. V. Shumyantseva, I. D. Shumov, V. P. Popov, O. V. Naumova, B. I. Fomin, D. A. Nasimov, A. L. Aseev, A. I. Archakov, *Lab Chip,* **2012**, 12, 5104.

[155] I. K. Lee, M. Jeun, H. J. Jang, W. J. Cho, K. H. Lee, *Nanoscale,* **2015**, 7, 16789.

[156] B. Babamiri, R. Hallaj, A. Salimi, *Sens. Actuators, B,* **2018**, 254, 551.

[157] N. Alizadeh, R. Hallaj, A. Salimi, *Biosens. Bioelectron.,* **2017**, 94, 184.

[158] Y. Wu, W. Guo, W. Peng, Q. Zhao, J. Piao, B. Zhang, X. Wu, H. Wang, X. Gong, J. Chang, *ACS Appl. Mater. Interfaces,* **2017**, 9, 9369.

[159] C. Liao, C. Mak, M. Zhang, H. L. W. Chan, F. Yan, *Adv. Mater.,* **2015**, 27, 676.

국문초록

최근 산업안전, 환경관리, 의료진단, 식품의 품질검사, 건강상태 추적 등 다양한 분야에서 화학센서와 바이오센서가 활용되면서 고기능 센서에 대한 수요가 폭발적으로 증가하고 있다. 센서의 성능을 평가하는 지표는 주로 민감도, 선택성, 반응/회복속도, 신뢰성 등을 짚을 수 있다. 트랜스듀서 물질은 타겟 물질과 직간접적으로 반응하여 이를 측정 가능한 전기적 신호로 변환시켜주는 역할로, 센서의 성능 향상에 근본적인 영향을 미치는 센서의 구성 요소 중 하나이다. 특히, 전도성 고분자 나노 물질은 무기물이나 금속산화물 기반 나노 물질 등과 비교하였을 때 다양한 구조로 쉽게 합성이 가능하고 표면 개질이 간단하며 가볍고 유연하다는 장점 때문에 트랜스듀서 물질로서 많은 연구가 진행되어왔다. 다양한 전도성 고분자 가운데 폴리피롤은 단량체가 쉽게 산화되고 물에 잘 녹으며 중합된 고분자가 강한 환경저항성, 우수한 산화환원 특성, 높은 전기전도도, 생체친화성을 나타내기 때문에 아주 매력적인 연구 대상이다. 이러한 폴리피롤 나노소재를 기반으로 한 센서 트랜스듀서는 다양한 중합법과 개질 방법을 결합하여 물리적

181

구조와 화학적 조성을 조절함으로써 센서 성능을 향상시키는 데 기여할 수 있다.

본 논문에서는 전기중합법으로 제조한 폴리피롤 나노와이어 기반의 트랜스듀서 물질을 각기 다른 개질법을 통해 물리적/화학적 변화를 주어 다양한 종류의 화학 및 바이오센서에 응용하는 방법을 제시한다. 첫 번째로, 중합온도 조절과 전기화학적 도핑 조절 법을 통해 다양한 모양과 도핑 레벨을 갖는 3차원 구조의 융털 모양 전도성 나노필름을 제조하였고, 이를 휘발성 유기화합물을 검출하는 가스 센서로 적용하였다. 그 결과, 도핑 레벨이 조절된 3차원 구조의 융털 모양 전도성 나노필름은 향상된 전하 이동도로 인해 암모니아와 메탄올 가스에 높은 민감도를 보여주었다. 두 번째로, 순차적인 전기도금법을 통해 다양한 팔라듐 입자 분포도와 입자 크기를 갖는 팔라듐 나노입자가 부착된 폴리피롤 나노구조를 제조하였다. 팔라듐 나노입자가 부착된 폴리피롤 나노구조는 고민감도의 수소 가스 센서용 트랜스듀서로 적용되었다. 마지막으로, 반응 시간 조절과 표면의 산 처리를 통해 다양한 종횡비와 다양한 농도의 카르복실 관능기를 갖는 폴리피롤 나노와이어 기반의 다차원 전도성 나노필름을 제조하였다. 이어서 압타머를 부착한

다차원 전도성 나노필름은 효과적으로 B형 간염 인자를 검출하는 센서로 적용되었다. 정리하면, 본 논문은 고민감도의 선택적이고 안정적이며 유연한 화학 및 바이오센서를 달성할 수 있는 트랜스듀서 물질로서 전도성 고분자 폴리피롤 나노와이어의 제조 및 응용에 대한 접근법을 제시한다. 나아가 본 연구에서 논의된 물질 제조 및 개질 방법론은 폴리피롤 이외의 다양한 유무기 나노 물질에도 확장될 수 있을 것으로 기대된다.

주요어: 센서, 폴리피롤 나노와이어, 전기도금, 도핑, 귀금속, 압타머

학 번: 2014-22602